

AD-A216 375



DTIC
ELECTE
JAN 03 1990
S D

Comparison of C⁻ and O-Grid Generation Methods
Using a NACA 0012 Airfoil

THESIS

Mark J. Lutton
Captain, USAF

AFIT/GAE/ENY/89D-21

DISTRIBUTION STATEMENT A

Approved for public release
Distribution Unlimited

DEPARTMENT OF THE AIR FORCE

AIR UNIVERSITY

AIR FORCE INSTITUTE OF TECHNOLOGY

Wright-Patterson Air Force Base, Ohio

90 01 02 096

AFIT/GAE/ENY/89D-21

1

DTIC
ELECTE
JAN 03 1990
S D D

Comparison of C- and O-Grid Generation Methods
Using a NACA 0012 Airfoil

THESIS

Mark J. Lutton
Captain, USAF

AFIT/GAE/ENY/89D-21

Approved for public release; distribution unlimited.

AFIT/GAE/ENY/89D-21

COMPARISON OF C- AND O-GRID GENERATION METHODS
USING A NACA 0012 AIRFOIL

THESIS

Presented to the Faculty of the School of Engineering
of the Air Force Institute of Technology
Air University
In Partial Fulfillment of the
Requirements for the Degree of
Master of Science in Aeronautical Engineering

Mark J. Lutton, B.S.

Captain, USAF

December, 1989



Accession For	
NTIS	CRA&I
DTIC	LAB
Unlimited	
Justification	
By	
Distribution	
Availability Codes	
Dist	Availability for Special
A-1	

Approved for public release; distribution unlimited.

Preface

The purpose of this research was to investigate and compare the performance of C- and O-grid generation methods as applied to predicting the flow about a NACA 0012 airfoil. The Beam and Warming algorithm was employed to solve the Navier-Stokes equations as applied to a two-dimensional, viscous, compressible flow. Similar flow conditions were established utilizing both grid generation methodologies and the results compared to experimental data. The NACA 0012 airfoil was chosen because it has been extensively studied and experimental results were readily available.

Numerical grid generation has become an important tool used in the numerical solution of partial differential equations. The general method involves a discretization of the physical domain into a collection of grid points. The differential equations are then approximated as a set of algebraic equations applied in this domain. In simplest terms, the grid is orthogonal and rectilinear. In the case of a curved boundary, such as an airfoil, it is advantageous to consider a conformal grid which greatly simplifies the application of the boundary conditions. The mapping between the physical and computational domains is accomplished by means of the transformation metrics, which must also be applied to the field equations one is attempting to solve. The accuracy of the numerical solution is therefore influenced by the type of grid chosen and the associated metrics. Differing methods of handling the boundary conditions may also have an influence on the numerical solution. For this reason, the differences in the metrics and the application of boundary conditions are also compared.

I would like to thank my thesis advisor, Capt Philip Beran for his continuing support and encouragement during this research. I would also like to thank Dr Joseph Shang, the sponsor of this research, for his strong support, for providing computer resources, and most especially for allowing me access to the outstanding group of people he supervises. Without the help of those mentioned this thesis could not

have been accomplished. Finally, a special thanks to my wife and children for their patience and moral support over the past six months.

Mark J. Lutton

Table of Contents

	Page
Preface	ii
Table of Contents	iv
List of Figures	vi
List of Tables	ix
List of Symbols	x
Abstract	xi
I. Introduction	1
II. Analysis	4
2.1 Governing Equations	4
2.2 Grid Analysis	13
III. Numerical Solution of the NS Equations	20
3.1 Implicit NS Code	20
3.2 Convergence Criteria	23
IV. Results and Discussion	24
4.1 Grids Employed	24
4.2 C-Grid Refinement Study	25
4.3 Comparison of C-grid and O-Grid Results	28
4.3.1 Subsonic Case	28
4.3.2 Transonic Case	29

	Page
4.3.3 Supersonic Case	31
4.3.4 Convergence Rate Comparison	32
4.4 Comparison of Transformation Metrics	33
V. Conclusions and Recommendations	95
Appendix A. Non-dimensional Variables	98
Appendix B. Jacobian Matrices	99
Appendix C. Boundary and Initial Conditions	102
Appendix D. Turbulence Model	105
Appendix E. Computer Resources and Codes	108
Bibliography	111
Vita	113

List of Figures

Figure	Page
1. Transformation from Physical to Computational Plane	15
2. C-grid 1 (119x40)	36
3. C-grid 2 (149x60)	37
4. C-grid 3 (179x80)	38
5. C-grid 4 (219x100)	39
6. C-grid 5: Refined Spacing for Shock (229x100)	40
7. C-grid 6: Modified Leading-Edge Spacing (219x100)	41
8. C-grid 7: Metrics Smoothed (219x100)	42
9. C-grid 8: Metrics Smoothed (299x60)	43
10. O-grid 1: .0051c TEC (204x108)	44
11. O-grid 2: .0025c TEC (204x108)	45
12. O-grid 3: .0015c TEC (204x100)	46
13. O-grid 4: .0015c TEC Modified Spacing (204x108)	47
14. O-grid 2: Trailing-Edge Geometry	48
15. O-grid 3: Leading Edge Geometry	49
16. C-grid 4: Leading Edge Geometry	50
17. C-grid 1: Subsonic Pressure Coefficient Profile	51
18. C-grid 4: Subsonic Pressure Coefficient Profile	52
19. C-grid 5: Subsonic Pressure Coefficient Profile	53
20. C-grid 1: Transonic Pressure Coefficient Profile	54
21. C-grid 4: Transonic Pressure Coefficient Profile	55
22. C-grid 5: Transonic Pressure Coefficient Profile	56
23. Transonic Pressure Coefficient Profile, Reduced Damping	57
24. C_l and C_d vs Artificial Viscosity	58

Figure	Page
25. C-grid 1: Mach Contours $M = 0.775, \alpha = 2.03$	59
26. C-grid 4: Mach Contours $M = 0.775, \alpha = 2.03$	60
27. Experimental Location of Shock Wave, $M = 0.775, \alpha = 2.03$	61
28. C-grid 2: Lift Coefficient vs Iterations, $M = 0.3, \alpha = 4.04$	62
29. C-grid 2: Lift Coefficient vs Iterations, $M = 0.775, \alpha = 2.03$	63
30. C-grid 4: Lift Coefficient vs Iterations, $M = 0.775, \alpha = 2.03$	64
31. O-grid 1: Subsonic Pressure Coefficient Profile	65
32. O-grid 3: Subsonic Pressure Coefficient Profile	66
33. C-grid 4, O-grid 3: Lift Coefficient vs Angle of Attack	67
34. C-grid 4, O-grid 3: Transonic Pressure Coefficient Profiles	68
35. O-grid 2: Transonic Pressure Coefficient Profile	69
36. O-grid 4: Transonic Pressure Coefficient Profile	70
37. O-grid 3: Mach Contours, $M = 0.775, \alpha = 2.03$	71
38. O-grid 4: Mach Contours, $M = 0.775, \alpha = 2.03$	72
39. C-grid 4: Pressure Coefficient Contours, $M = 0.775, \alpha = 2.03$	73
40. O-grid 3: Pressure Coefficient Contours, $M = 0.775, \alpha = 2.03$	74
41. O-grid 4: Pressure Coefficient Contours, $M = 0.775, \alpha = 2.03$	75
42. O-grid 3: Vorticity Contours $M = 0.775, \alpha = 2.03$	76
43. C-grid 4: Vorticity Contours, $M = 0.775, \alpha = 2.03$	76
44. O-grid 3: Mach Contours, $M = 1.1, \alpha = 6.00$	77
45. C-grid 4: Mach Contours, $M = 1.1, \alpha = 6.00$	78
46. O-grid 3: Pressure Coefficient Contours, $M = 1.1, \alpha = 6.00$	79
47. C-grid 4: Pressure Coefficient Contours, $M = 1.1, \alpha = 6.00$	80
48. O-grid 3: Vorticity Contours, $M = 1.1, \alpha = 6.00$	81
49. C-grid 4: Vorticity Contours $M = 1.1, \alpha = 6.00$	81
50. C-grid 8: Mach Contours, $M = 1.1, \alpha = 6.00$	82
51. C-grid 8: Vorticity Contours, $M = 1.1, \alpha = 6.00$	82

Figure	Page
52. O-grid 3: Force Coefficients vs Iterations, $M = 0.3, \alpha = 4.04$	83
53. C-grid 4: Force Coefficients vs Iterations, $M = 0.3, \alpha = 4.04$	84
54. O-grid 3: Force Coefficients vs Iterations, $M = 0.775, \alpha = 2.03$	85
55. C-grid 4: Force Coefficients vs Iterations, $M = 0.775, \alpha = 2.03$	86
56. C-grid 4: Aspect Ratio Contours	87
57. O-grid 3: Aspect Ratio Contours	88
58. C-grid 4: Non-orthogonality Contours	89
59. O-grid 3: Non-orthogonality Contours	90
60. C-grid 4: Jacobian Contours	91
61. O-grid 3: Jacobian Contours	92
62. C-grid 4: Jacobian Contours - Smoothed Metrics	93
63. C-grid 8: Jacobian Contours - Smoothed Metrics	94
64. Regions of Application for Turbulence Model	107

List of Tables

Table	Page
1. C-Grid Specifications	26
2. O-Grid Specifications	26
3. Comparison of CPU times: Cray vs Stellar	108

List of Symbols

<u>Symbol</u>	<u>Definition</u>
A	Jacobian Matrix
B	Jacobian Matrix
C_d	Drag Coefficient
C_l	Lift Coefficient
C_p	Pressure Coefficient
c	airfoil chord
c_p	Specific heat at constant pressure
C	Courant number
D_e, D_i	Damping coefficients
E_t	Total internal energy
e	Specific internal energy
F	Flux vector
\vec{f}	Body force vector
G	Flux vector
I	Identity matrix
IL	Number of grid points in ξ direction
J	Transformation Jacobian
JL	Number of grid points in η direction
k	Coefficient of thermal conductivity
k_t	Turbulent coefficient of thermal conductivity
L	Reference length
M	Mach number
M	Jacobian matrix
N	Number of iterations
N	Jacobian matrix
p	Pressure
Pr	Molecular Prandtl number
Pr_t	Turbulent Prandtl number
Q	Internal heat generation
\vec{q}	Heat conduction vector
R	Perfect gas constant
Re	Reynolds number
T	Temperature
t	time
U	Vector of dependant variables

u	Stream wise velocity component
\mathcal{U}	Contravariant velocity
\vec{V}	Velocity vector
v	Normal velocity component
\mathcal{V}	Contravariant velocity
x	Streamwise coordinate direction
y	Normal coordinate direction
α	Angle of attack
γ	Specific heat ratio
Δ	Difference operator
δ	Finite difference operator
ϵ	Turbulent eddy viscosity
η	Normal coordinate direction
ξ	Tangential coordinate direction
μ	Molecular viscosity
ρ	Density
$\underline{\sigma}$	Stress tensor
$\underline{\tau}$	Shear stress tensor
ω	Vorticity

Abstract

The purpose of this study was to investigate and compare the performance of C- and O-grid topologies as applied to numerically predicting the flow about a NACA 0012 airfoil. Both types of grid were generated using a hyperbolic grid generation code. The solution of the flow field was numerically calculated using the Beam and Warming approximate factorization method to solve the two-dimensional Navier-Stokes equations for viscous, compressible flow.

This study examined the performance of each grid for a range of Mach number (0.3 to 1.1) and angle of attack (2 to 12 degrees). The Reynolds number was approximately 2,000,000, with variations to exactly match experimental flow conditions. The numerical inquiry consisted of two parts. The first part was a grid sensitivity study using the C-grid. Progressively finer grids were employed until the respective numerical solutions converged. The second part was a parametric study using the O-grid. The trailing edge curvature was reduced from 0.005c to 0.0015c and the numerical results compared with those of the C-grid.

The numerical solutions obtained with both the C- and O-grid configurations compare favorably to both experiment and previous numerical results. The numerical results produced indicate that both grids are satisfactory in a general application. However, specific weaknesses arise for each type of grid in certain situations. In these instances, there may be an advantage in selecting a particular type of grid.

In the subsonic range, the O-grid is superior to the C-grid in determining the pressure coefficient in the vicinity of the leading edge. The O-grid displays an advantage when large flow gradients appear in the vicinity of the trailing edge, such as the formation of a lambda shock. The O-grid also attains convergence for certain critical cases (high Mach number, Reynolds number, or angle of attack) for which the C-grid solution diverges.

The C-grid displayed several advantages over the O-grid. One advantage is ease of application. It is generally easier to construct a C- grid to a given set of specifications than an O-grid. The C-grid handles the flow resolution better in the wake, especially when the flow gradients are concentrated directly behind the airfoil. In this region the C-grid displays a considerably higher concentration of grid points. The C-grid also predicts the pressure distribution at transonic speeds and the mid-chord shock location more accurately the O-grid.

COMPARISON OF C- AND O-GRID GENERATION METHODS USING A NACA 0012 AIRFOIL

I. Introduction

The purpose of this study is to investigate and compare the performance of two differing grid generation methods with varying topologies as applied to the flow about a NACA 0012 airfoil. The numerical method of solution is based on the Beam and Warming approximate-factorization algorithm applied to the two-dimensional, mass-averaged, Navier-Stokes equations for compressible, viscous flows. While this algorithm is applicable to both steady and unsteady flows, the solutions considered in this study are all steady state.

Numerical grid generation has become an important tool used in the numerical solution of partial differential equations (PDEs). The general method involves a discretization of the physical domain into a collection of grid points. The differential equations are then approximated as a set of non-linear algebraic equations applied to this domain. In simplest form, the grid is orthogonal and rectilinear. In the case of a curved boundary, the difficulty of extrapolating data at gridpoints adjacent to the boundaries is introduced. Not only is this extrapolation cumbersome and difficult, it also imposes a reduction in the order of accuracy for the boundary conditions, thus degrading the fidelity of the solution throughout the field. To overcome these difficulties for the case of a curved or irregular boundary, such as an airfoil, it is advantageous to consider a conformal grid that simultaneously eases the implementation of the boundary conditions and avoids the loss of accuracy associated with the aforementioned method.

Grid generation methods can be classified into three major categories (6:521): complex variable methods, algebraic methods, and differential equation methods. The differential equation method is the most common and powerful, especially for complex geometries. These methods generally employ solutions of Laplace's or Poisson's equations to specify the coordinate transformation between the physical and computational domains. The PDEs chosen are generally elliptic or hyperbolic, although some recent investigations have explored parabolic grid generators. The elliptical methods have a strong applicability to internal flows and also to external flows where multiple bodies are present. Hyperbolic methods are generally easier to apply and are applicable for external flows where there is no constraint of the outer computational domain. The grid generation code employed in this study was written by Barth and Kinsey (9) and is a modification of the hyperbolic method described by Steger and Chaussee (15).

Two different types of grid are considered in this work: a C-grid and an O-grid. The C-grid envelopes the airfoil in C-shaped loops beginning and terminating in the far wake. The branch cut, or the line along which the numbering of the grid lines begins and ends, therefore exists in the wake and extends from the trailing edge to the far field boundary. The O-grid has oval-like loops which completely encircle the airfoil. The cut line for the O-grid is arbitrary, and for this study extends from the far-field boundary in front of the airfoil to the leading edge.

Of particular interest when comparing two different grids for a given application, aside from rectifiable differences such as grid spacing and resolution, are the transformation metrics, which provide the mathematical map from the physical to the computational domains. Since the metrics appear in the differencing equations to be solved, they have an impact on the local truncation error. Also of interest are any differences due to the varying means of applying the boundary conditions.

This study consists of two basic parts. The first consists of a grid refinement study using the C-grid. Progressively finer C-grids were employed for selected con-

ditions (Mach number ranging from 0.3 to 0.78; angle of attack between 2 and 4 degrees) until the solutions became invariant. To incorporate the O-grid generator for the NACA 0012 airfoil, it is necessary to truncate the trailing edge and fit it with a circular arc. As the truncation point is moved aft, the resulting trailing-edge radius of curvature (TEC) becomes smaller. The second part of the study involved a parametric study based on the TEC. Values of TEC ranging from 0.005c to 0.0015c were considered. The results are compared with those obtained using the C-grid.

Data analyzed for comparative purposes included the lift coefficient, C_l , drag coefficient, C_d , and pressure coefficient, \mathcal{C}_p . To examine convergence rate differences, C_l and C_d are plotted versus iteration number. Contours of Mach number, pressure coefficient, and vorticity are presented. Contours of the Jacobian, aspect ratio, and orthogonality are presented and examined to determine structural differences between the two grid types.

Both versions of the Navier-Stokes code (for C- and O-grids) were authored by Dr Miguel Visbal of the Wright Research and Development Center (WRDC) Flight Dynamics Lab (FDL) (16) (17). The code is an implementation of the implicit, approximate-factorization algorithm developed by Beam and Warming (4). The turbulence model is a modification of the algebraic eddy viscosity model developed by Baldwin and Lomax (3) (See Appendix D).

Computer resources required were provided by FDL and included accounts on the Cray-Vax and the Cray XMP. Data plots were performed on the FDL Prime computer. Selected data runs were performed on the AFIT Stellar computer for the dual purpose of comparison and code checkout.

II. Analysis

2.1 Governing Equations

The fundamental equations of fluid dynamics are based on the principles of classical mechanics and thermodynamics: the conservation of mass, momentum, and energy. These equations are often grouped together and referred to as the Navier-Stokes equations. The equations are presented in an Eulerian formulation using vector notation, and are valid for unsteady, compressible, and viscous flows (13:11):

Conservation of Mass (Continuity)

$$\frac{\partial \rho}{\partial t} + \vec{\nabla} \cdot (\rho \vec{V}) = 0, \quad (1)$$

Conservation of Momentum (Newton's Second Law)

$$\frac{\partial(\rho \vec{V})}{\partial t} + \vec{\nabla} \cdot (\rho \vec{V} \vec{V}) = \rho \vec{f} + \vec{\nabla} \cdot \underline{\sigma}, \quad (2)$$

Conservation of Energy (First Law of Thermodynamics)

$$\frac{\partial E_t}{\partial t} + (\vec{V} \cdot \vec{\nabla}) E_t = \frac{\partial Q}{\partial t} + \rho \vec{f} \cdot \vec{V} + \vec{\nabla} \cdot (\underline{\sigma} \cdot \vec{V}) - \vec{\nabla} \cdot \vec{q}. \quad (3)$$

The stress tensor $\underline{\sigma}$ is expressed in terms of the fluid pressure and the viscous stress tensor, $\underline{\tau}$,

$$\underline{\sigma} = -pI + \underline{\tau}. \quad (4)$$

Other variables are defined in the list of symbols at the beginning of this report. Two additional relations are required to close the equations. These are the

equation of state for a perfect fluid

$$p = \rho RT = \rho e(\gamma - 1), \quad (5)$$

and Fourier's law of heat conduction that relates the heat flux vector to the temperature gradient

$$\vec{q} = -k\vec{\nabla}T, \quad (6)$$

where the thermal conductivity, k , is a function of the temperature.

If a Newtonian fluid is assumed, then Stokes' law relates the viscous stresses to the rate of strain

$$\underline{\tau} = \lambda(\vec{\nabla} \cdot \vec{V})I + \mu(\vec{\nabla}\vec{V} + (\vec{\nabla}\vec{V})^T), \quad (7)$$

where Stokes' hypothesis $3\lambda + 2\mu = 0$ essentially equates the mean pressure in a deforming viscous fluid and the thermodynamic pressure (20:70). The total internal energy, E_t , can be related to the specific internal energy, e , and the velocity (in two dimensions):

$$E_t = \rho \left(e + \frac{u^2 + v^2}{2} \right). \quad (8)$$

To facilitate the solution of the NS equations, they are nondimensionalized (see Appendix A) and are given below in conservation-law form for a two-dimensional, rectilinear coordinate system. The internal heat generation, Q , is assumed constant in time.

$$\frac{\partial \rho}{\partial t} + \frac{\partial(\rho u)}{\partial x} + \frac{\partial(\rho v)}{\partial y} = 0 \quad (9)$$

$$\frac{\partial(\rho u)}{\partial t} + \frac{\partial(\rho u^2 + p - \tau_{xx})}{\partial x} + \frac{\partial(\rho uv - \tau_{xy})}{\partial y} = \rho \tilde{f}_x \quad (10)$$

$$\frac{\partial(\rho v)}{\partial t} + \frac{\partial(\rho v^2 + p - \tau_{yy})}{\partial y} + \frac{\partial(\rho uv - \tau_{yx})}{\partial x} = \rho \tilde{f}_y \quad (11)$$

$$\begin{aligned} \frac{\partial E_t}{\partial t} - \rho(\tilde{f}_x u + \tilde{f}_y v) + \frac{\partial(E_t u + pu - u\tau_{xx} - v\tau_{yx} + q_x)}{\partial x} \\ + \frac{\partial(E_t v + pv - u\tau_{xy} - v\tau_{yy} + q_y)}{\partial y} = 0. \end{aligned} \quad (12)$$

The components of the non-dimensional stress tensor are given by

$$\tau_{ij} = -p\delta_{ij} + \frac{\mu}{Re} \left(\frac{\partial u_i}{\partial x_j} + \frac{\partial u_j}{\partial x_i} \right) + \delta_{ij} \lambda \frac{\partial u_k}{\partial x_k}. \quad (13)$$

These equations are applicable to an orthogonal, rectilinear coordinate system. To transform the equations so that they apply to a general curvilinear coordinate system, the chain rule is employed. The transformation is from the physical domain (x, y) to the computational domain (ξ, η) , where the partial derivatives take the following form (13:252)

$$\xi = \xi(x, y) \quad (14)$$

$$\eta = \eta(x, y). \quad (15)$$

The direct application of the chain rule then produces the derivative operators

$$\begin{aligned} \frac{\partial}{\partial x} &= \frac{\partial \xi}{\partial x} \frac{\partial}{\partial \xi} + \frac{\partial \eta}{\partial x} \frac{\partial}{\partial \eta} \\ &= \xi_x \frac{\partial}{\partial \xi} + \eta_x \frac{\partial}{\partial \eta} \end{aligned} \quad (16)$$

$$\begin{aligned} \frac{\partial}{\partial y} &= \frac{\partial \xi}{\partial y} \frac{\partial}{\partial \xi} + \frac{\partial \eta}{\partial y} \frac{\partial}{\partial \eta} \\ &= \xi_y \frac{\partial}{\partial \xi} + \eta_y \frac{\partial}{\partial \eta}. \end{aligned} \quad (17)$$

$$(18)$$

The metrics are determined in the following manner

$$d\xi = \xi_x dx + \xi_y dy \quad (19)$$

$$d\eta = \eta_x dx + \eta_y dy. \quad (20)$$

In matrix form

$$\begin{bmatrix} d\xi \\ d\eta \end{bmatrix} = \begin{bmatrix} \xi_x & \xi_y \\ \eta_x & \eta_y \end{bmatrix} \begin{bmatrix} dx \\ dy \end{bmatrix} \quad (21)$$

$$\begin{bmatrix} dx \\ dy \end{bmatrix} = \begin{bmatrix} x_\xi & x_\eta \\ y_\xi & y_\eta \end{bmatrix} \begin{bmatrix} d\xi \\ d\eta \end{bmatrix}, \quad (22)$$

and

$$\begin{bmatrix} \xi_x & \xi_y \\ \eta_x & \eta_y \end{bmatrix} = \begin{bmatrix} x_\xi & x_\eta \\ y_\xi & y_\eta \end{bmatrix}^{-1} = J \begin{bmatrix} y_\eta & -x_\eta \\ -y_\xi & x_\xi \end{bmatrix}. \quad (23)$$

Therefore, by solving the transformation identity (19:141)

$$\begin{bmatrix} \xi_x & \xi_y \\ \eta_x & \eta_y \end{bmatrix} \begin{bmatrix} x_\xi & x_\eta \\ y_\xi & y_\eta \end{bmatrix}^{-1} = \begin{bmatrix} 1 & 0 \\ 0 & 1 \end{bmatrix}, \quad (24)$$

and defining the Jacobian of the transformation

$$J = \frac{\partial(\xi, \eta)}{\partial(x, y)} = \begin{vmatrix} \frac{\partial \xi}{\partial x} & \frac{\partial \xi}{\partial y} \\ \frac{\partial \eta}{\partial x} & \frac{\partial \eta}{\partial y} \end{vmatrix} = \xi_x \eta_y - \xi_y \eta_x \quad (25)$$

$$J = \frac{1}{\frac{\partial(x,y)}{\partial(\xi,\eta)}} = \frac{1}{\begin{vmatrix} \frac{\partial x}{\partial \xi} & \frac{\partial x}{\partial \eta} \\ \frac{\partial y}{\partial \xi} & \frac{\partial y}{\partial \eta} \end{vmatrix}} = \frac{1}{x_\xi y_\eta - x_\eta y_\xi}, \quad (26)$$

the following relationship between the metrics can be established:

$$\xi_x = y_\eta J \quad \xi_y = -x_\eta J \quad (27)$$

$$\eta_x = -y_\xi J \quad \eta_y = -x_\xi J. \quad (28)$$

The NS equations may then be written in terms of the general curvilinear coordinates (18:5)

$$\frac{\partial U}{\partial t} + \xi_x \frac{\partial F}{\partial \xi} + \xi_y \frac{\partial G}{\partial \xi} + \eta_x \frac{\partial F}{\partial \eta} + \eta_y \frac{\partial G}{\partial \eta} = 0, \quad (29)$$

where body forces are omitted and

$$U = (\rho, \rho u, \rho v, \rho e)^T \quad (30)$$

$$F = \begin{pmatrix} \rho u \\ \rho u^2 - \tau_{xx} \\ \rho uv - \tau_{xy} \\ (\rho e + p)u - F_4 \end{pmatrix} \quad (31)$$

$$G = \begin{pmatrix} \rho v \\ \rho uv - \tau_{xy} \\ \rho v^2 - \tau_{yy} \\ (\rho e + p)v - G_4 \end{pmatrix}. \quad (32)$$

To incorporate turbulence, the viscosity is separated into the molecular viscosity, μ , and the turbulent eddy viscosity, ϵ . Then Stokes' hypothesis is extended to include the turbulent eddy viscosity as

$$\lambda_t = -\frac{2}{3}(\mu + \epsilon). \quad (33)$$

The molecular viscosity is calculated from Sutherland's formula. The turbulent eddy viscosity is obtained via the eddy viscosity model of Baldwin and Lomax (3) (See Appendix D). In a similar fashion, the thermal conductivity is separated into a nominal component, k , and a turbulent component, k_t , by defining the nominal and turbulent Prandtl numbers respectively

$$k = c_p \frac{\mu}{Pr} \quad k_t = c_p \frac{\epsilon}{Pr_t}. \quad (34)$$

The viscous stress and heat conduction terms can then be written in the following form (18:6)

$$\tau_{xx} = -3\lambda_t u_x + \lambda_t(u_x + v_y) \quad (35)$$

$$\tau_{xy} = -\frac{3}{2}\lambda_t(u_x + v_y) \quad (36)$$

$$\tau_{yy} = -3\lambda_t v_y + \lambda_t(u_x + v_y) \quad (37)$$

$$F_4 = u\tau_{xx} + v\tau_{xy} - q_x \quad (38)$$

$$G_4 = u\tau_{xy} + v\tau_{yy} - q_y \quad (39)$$

$$p = \rho(\gamma - 1)\left(e - \frac{1}{2}(u^2 + v^2)\right) \quad (40)$$

$$q_x = -(k + k_t)\frac{\partial T}{\partial x} \quad (41)$$

$$q_y = -(k + k_t)\frac{\partial T}{\partial y}. \quad (42)$$

The molecular Prandtl number, Pr , the turbulent Prandtl number, Pr_t , and the

specific heat at constant pressure, c_p , are taken as constants:

$$Pr = \frac{\mu c_p}{k} \cong .72 \quad (43)$$

$$Pr_t = \frac{\varepsilon c_p}{k} \cong .9 \quad (44)$$

$$c_p = \frac{\gamma R}{\gamma - 1} \cong 1,000 \text{ Joules/Kg-K.} \quad (45)$$

The NS equations can be cast in strong conservative form as follows (18:7)

$$\frac{\partial \hat{U}}{\partial t} + \frac{\partial \hat{F}}{\partial \xi} + \frac{\partial \hat{G}}{\partial \eta} = 0, \quad (46)$$

where

$$\hat{U} = \frac{U}{J} \quad (47)$$

$$\hat{F} = \frac{(\xi_x F + \xi_y G)}{J} \quad (48)$$

$$\hat{G} = \frac{(\eta_x F + \eta_y G)}{J}. \quad (49)$$

To facilitate the numerical implementation, the strong-conservation form of the equations is rewritten as (18:8)

$$\frac{\partial \hat{U}}{\partial t} + \frac{\partial E_1}{\partial \xi} + \frac{\partial E_2}{\partial \eta} = \frac{\partial V_1(\hat{U}, \hat{U}_\xi)}{\partial \xi} + \frac{\partial V_2(\hat{U}, \hat{U}_\eta)}{\partial \xi} + \frac{\partial W_1(\hat{U}, U_\xi)}{\partial \eta} + \frac{\partial W_2(\hat{U}, \hat{U}_\eta)}{\partial \eta} \quad (50)$$

where

$$E_1 = \frac{1}{J} \begin{pmatrix} \rho \mathcal{U} \\ \rho u \mathcal{U} + \xi_x p \\ \rho v \mathcal{U} + \xi_y p \\ (p + \rho e) \mathcal{U} \end{pmatrix} \quad (51)$$

$$E_2 = \frac{1}{J} \begin{pmatrix} \rho \mathcal{V} \\ \rho u \mathcal{V} + \eta_x p \\ \rho v \mathcal{V} + \eta_y p \\ (p + \rho e) \mathcal{V} \end{pmatrix} \quad (52)$$

$$V_1 = \frac{1}{J} \begin{pmatrix} 0 \\ b_1 u_\xi + b_2 v_\xi \\ b_3 u_\xi + b_4 v_\xi \\ b_1 u u_\xi + b_2 (v u_\xi + u v_\xi) + b_3 v v_\xi + b_4 T_\xi \end{pmatrix} \quad (53)$$

$$V_2 = \frac{1}{J} \begin{pmatrix} 0 \\ c_1 u_\eta + c_2 v_\eta \\ c_3 u_\eta + c_4 v_\eta \\ c_1 u u_\eta + c_2 u v_\eta + c_3 v u_\eta + c_4 v v_\eta + c_5 T_\eta \end{pmatrix} \quad (54)$$

$$W_1 = \frac{1}{J} \begin{pmatrix} 0 \\ c_1 u_\xi + c_3 v_\xi \\ c_2 u_\xi + c_4 v_\xi \\ c_1 u u_\xi + c_2 v u_\xi + c_3 u v_\xi + c_4 v v_\xi + c_5 T_\xi \end{pmatrix} \quad (55)$$

$$W_2 = \frac{1}{J} \begin{pmatrix} 0 \\ d_1 u_\eta + d_2 v_\eta \\ d_2 u_\eta + d_3 v_\eta \\ d_1 u u_\eta + d_2 (v u_\eta + u v_\eta) + d_3 v v_\eta + d_4 T_\eta \end{pmatrix} \quad (56)$$

U and V denote the contravariant velocities:

$$U = \xi_x u + \xi_y v \quad (57)$$

$$V = \eta_x u + \eta_y v. \quad (58)$$

The viscous coefficients are:

$$b_1 = -\frac{3}{2} \lambda_1 \left(\frac{4}{3} \xi_x^2 + \xi_y^2 \right) \quad (59)$$

$$b_2 = -\frac{1}{2} \lambda_1 \xi_x \xi_y \quad (60)$$

$$b_3 = -\frac{3}{2} \lambda_1 \left(\frac{4}{3} \eta_y^2 + \eta_x^2 \right) \quad (61)$$

$$b_4 = c_p \left(\frac{\mu}{Pr} + \frac{\epsilon}{Pr_1} \right) (\xi_x^2 + \xi_y^2) \quad (62)$$

$$c_1 = \frac{3}{2} \lambda_1 \left(\frac{4}{3} \xi_x \eta_x + \xi_y \eta_y \right) \quad (63)$$

$$c_2 = \frac{3}{2} \lambda_1 \left(\frac{2}{3} \xi_x \eta_y - \xi_y \eta_x \right) \quad (64)$$

$$c_3 = -\frac{3}{2} \lambda_1 \left(\xi_x \eta_y + \frac{2}{3} \xi_y \eta_x \right) \quad (65)$$

$$c_4 = \frac{3}{2} \lambda_1 \left(\xi_x \eta_x + \frac{2}{3} \xi_y \eta_y \right) \quad (66)$$

$$c_5 = -c_p \left(\frac{\mu}{Pr} + \frac{\epsilon}{Pr_1} \right) (\xi_x \eta_x + \xi_y \eta_y) \quad (67)$$

$$d_1 = -\frac{3}{2} \lambda_1 \left(\frac{4}{3} \eta_x^2 + \eta_y^2 \right) \quad (68)$$

$$d_2 = -\frac{1}{2} \lambda_1 \eta_x \eta_y \quad (69)$$

$$d_3 = -\frac{3}{2} \lambda_1 \left(\frac{4}{3} \eta_y^2 + \eta_x^2 \right) \quad (70)$$

$$d_4 = c_p \left(\frac{\mu}{Pr} + \frac{\epsilon}{Pr_1} \right) (\eta_x^2 + \eta_y^2). \quad (71)$$

The NS equations written in the above form are valid for unsteady, viscous flows. The governing equations form a hybrid hyperbolic-parabolic system. Their parabolic nature arises from the second-order derivatives in the momentum and energy equations. The continuity equation contains only first-order terms and is hyperbolic (5:27). These characteristics of the system of partial differential equations dictate the manner in which the boundary conditions may be applied (13:312). See Appendix C for an explanation of the boundary conditions.

2.2 Grid Analysis

As previously mentioned, the grids used for this study were of two types: C-grid and O-grid. Both were numerically generated using the hyperbolic grid generation method of Steger and Chaussee (15) as incorporated in the code written by Barth and Kinsey (9). An advantage of employing a hyperbolic grid generator is that only the inner boundary need be specified (6:530), i.e., a point distribution is specified on the airfoil surface only. The solution then proceeds outward from the surface in a time-like manner.

The algorithm developed by Steger and Chaussee utilizes the definitions of the transformation Jacobian and cell orthogonality to devise a mapping scheme from the physical to the computational domain (9:3):

$$x_{\xi}x_{\eta} + y_{\xi}y_{\eta} = 0 \quad \text{Orthogonality} \quad (72)$$

$$J = \frac{\partial(\xi,\eta)}{\partial(x,y)} = \xi_x\eta_y - \eta_x\xi_y \quad \text{Jacobian} \quad (73)$$

$$J^{-1} = \frac{\partial(x,y)}{\partial(\xi,\eta)} = x_{\xi}y_{\eta} - x_{\eta}y_{\xi} \quad \text{Inverse Jacobian.} \quad (74)$$

Here the Jacobian represents the cell area ratio between the computational and

physical domains, and is variable throughout the mesh. A typical transformation is illustrated in Figure 1. The area integrands in the the physical and computational domains can be written as follows (9:3):

$$dA = dx dy = J^{-1} d\xi d\eta \quad (75)$$

$$J dx dy = d\xi d\eta. \quad (76)$$

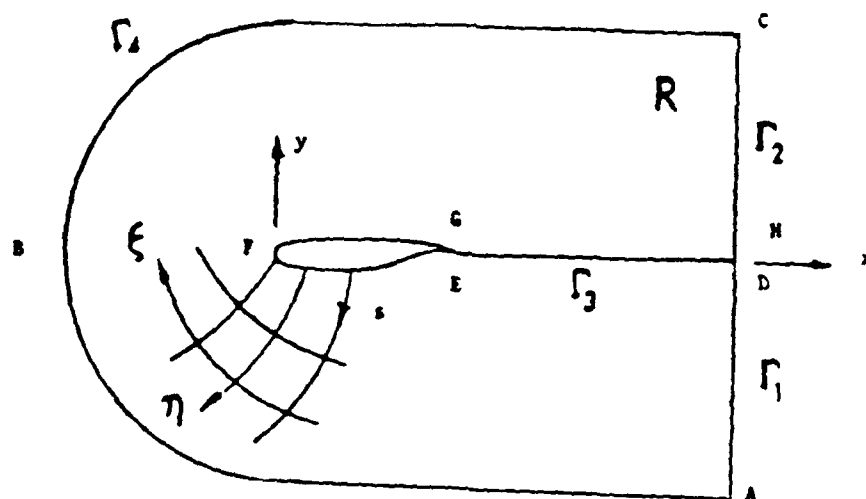
Numerically, $\Delta\xi$ and $\Delta\eta$ are arbitrary and are most conveniently chosen to equal one. In this case, the inverse Jacobian approximates the physical cell area. The orthogonality constraint and inverse Jacobian are locally linearized using

$$x = x^o + \Delta x \quad (77)$$

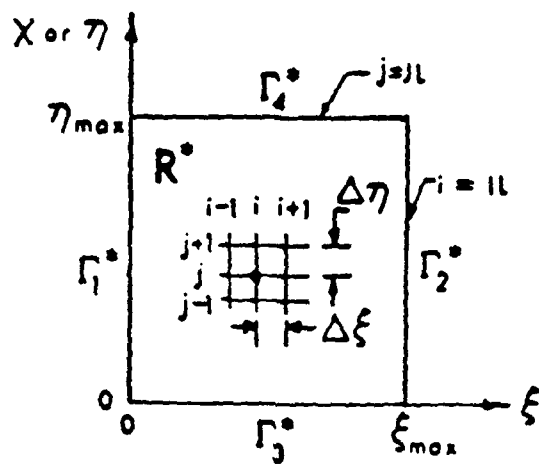
$$y = y^o + \Delta y, \quad (78)$$

where x^o and y^o denote a known, near-solution state. The linearization then proceeds as follows (15:433):

$$\begin{aligned} x_\xi x_\eta &= (x^o + \Delta x)_\xi (x^o + \Delta x)_\eta \\ &= x_\xi^o x_\eta^o + x_\xi^o \Delta x_\eta + x_\eta^o \Delta x_\xi + O(\Delta^2) \\ &= x_\xi^o x_\eta^o + x_\xi^o (x - x^o)_\eta + x_\eta^o (x - x^o)_\xi \\ &= x_\xi^o x_\eta + x_\eta^o x_\xi - x_\xi^o x_\eta^o \end{aligned} \quad (79)$$



(a) Physical Plane



(b) Transformed Plane

Figure 1. Transformation from Physical to Computational Plane (Ref:18)

The resulting locally linearized system is then (9:4)

$$\begin{bmatrix} x_\eta^o & y_\eta^o \\ y_\eta^o & -x_\eta^o \end{bmatrix} \begin{bmatrix} x \\ y \end{bmatrix}_\xi + \begin{bmatrix} x_\xi^o & y_\xi^o \\ -y_\xi^o & x_\xi^o \end{bmatrix} \begin{bmatrix} x \\ y \end{bmatrix}_\eta = \begin{bmatrix} 0 \\ V + V^o \end{bmatrix} \quad (80)$$

or alternately

$$A\tilde{R}_\xi + B\tilde{R}_\eta = \tilde{F}. \quad (81)$$

The finite-difference scheme is central differenced in ξ and forward differenced in η . Typically, x_ξ^o and y_ξ^o are approximated as follows (9:6)

$$x_\xi^o = \frac{x_{i+1,j} - x_{i-1,j}}{2\Delta\xi} \quad (82)$$

$$y_\xi^o = \frac{y_{i+1,j} - y_{i-1,j}}{2\Delta\xi}, \quad (83)$$

while x_η^o and y_η^o are extracted from the orthogonality constraint and the Jacobian.

$$x_\eta^o = \frac{-y_\xi^o V^o}{(x_\xi^o)^2 + (y_\xi^o)^2} \quad (84)$$

$$y_\eta^o = \frac{x_\xi^o V^o}{(x_\xi^o)^2 + (y_\xi^o)^2}. \quad (85)$$

There are certain geometric conditions for which the hyperbolic algorithm as described has difficulties. These are pronounced slope discontinuities and regions of reverse or concave curvature. These problems may produce unwanted grid characteristics if the discontinuities or regions of reverse curvature propagate into the grid interior. By adding explicit and implicit dissipation these difficulties can be partially circumvented. The resulting hyperbolic equations are utilized in the numerical code of Barth and Kinsey. The reader is referred to (9) for a development of the delta formulation of the algorithm employed.

Since the local truncation error will in part depend upon the discretization of the coordinate system (i.e., the transformation metrics), it is useful to have an alternate means to examine a grid in terms of these parameters. A physically meaningful reparameterization of the Jacobian matrix is presented by Kerlick and Klopfer (8). The metric tensor is introduced as an intrinsic property of the transformed geometry. The metric tensor is defined as (8:788)

$$g_{ij} = \delta_{kl} \frac{dx^k}{d\xi^i} \frac{dx^l}{d\xi^j}, \quad (86)$$

where δ_{kl} represents the Kronecker delta function

$$\delta_{kl} = \begin{cases} 0 & \text{if } k \neq l \\ 1 & \text{if } k = l. \end{cases}$$

In general, this approach is valid for three dimensions. However, in the current context, the following is presented for the two-dimensional case where $\xi^1 = \xi$ and $\xi^2 = \eta$. The components of the metric tensor may then be written as

$$g_{11} = x_\xi^2 + y_\xi^2 \quad (87)$$

$$g_{12} = x_\xi x_\eta + y_\xi y_\eta \quad (88)$$

$$g_{22} = x_\eta^2 + y_\eta^2. \quad (89)$$

The metric tensor can be decomposed into its determinant and into terms which quantify the aspect ratio and orthogonality of the grid cells. The skewness, or the angular deviation between the physical and computational coordinate lines, is also defined via components of the metric tensor. In terms of the metric tensor, the inverse Jacobian is defined by

$$(J^{-1})^2 = \det[g_{ij}] = (x_\xi y_\eta - x_\eta y_\xi)^2.$$

The orthogonality of the grid is characterized by the angle θ_{ij} between the tangent lines to the ξ and η coordinate lines at the points of intersection, where

$$\cos(\theta_{ij}) = \frac{g_{ij}}{\sqrt{g_{ii}g_{jj}}} \quad (i \neq j; \text{no sum on } i,j) \quad (90)$$

$$= \frac{x_\xi x_\eta + y_\xi y_\eta}{\sqrt{x_\xi^2 + y_\xi^2} \sqrt{x_\eta^2 + y_\eta^2}}. \quad (91)$$

The aspect ratio is defined by

$$A_k = \sqrt{\frac{g_{kk}}{g_{11}}} \quad (k=2,n; \text{no sum on } k) \quad (92)$$

$$= \sqrt{\frac{x_\eta^2 + y_\eta^2}{x_\xi^2 + y_\xi^2}}, \quad (93)$$

while the cosine of the skewness angle, α_s , is determined by

$$\cos(\alpha_s) = \frac{x_\xi}{\sqrt{g_{11}}} \quad (94)$$

$$= \frac{x_\xi}{\sqrt{x_\xi^2 + y_\xi^2}}. \quad (95)$$

A complete error analysis of the Beam and Warming algorithm incorporating the effects of the metrics is beyond the scope of this report (see McRae and Klopfer (12)). However, an examination of the metric parameters listed above can provide some insight into the degree of truncation error induced by the grid. In particular, one should suspect increased truncation error when the gradient of the metrics and the associated metric parameters becomes large. This is particularly true if large flow gradients develop at the same location.

III. Numerical Solution of the NS Equations

The numerical procedure for the solution of the Navier-Stokes equations is outlined in this chapter. The finite-difference scheme employed is based on the work by R. M. Beam and R. F. Warming and is known as the Beam and Warming approximate factorization algorithm (5). The algorithm has four pertinent characteristics (19:139):

1. unconditional stability,
2. spatial factorization,
3. delta formulation, and
4. three-level implicit structure.

3.1 Implicit NS Code

The implicit implementation solves the strong conservation form of the Navier-Stokes equations. In delta formulation, with first-order Euler time differencing, the scheme may be written as follows (18):

$$\left\{ I + \Delta t \left(\frac{\partial A^n}{\partial \xi} - \frac{\partial^2 M^n}{\partial \xi^2} \right) \right\} \left\{ I + \Delta t \left(\frac{\partial B^n}{\partial \eta} - \frac{\partial^2 N^n}{\partial \eta^2} \right) \right\} \Delta \hat{U}^n = -\Delta t \left\{ \frac{\partial}{\partial \xi} (E_1 - V_1 - V_2)^n + \frac{\partial}{\partial \eta} (E_2 - W_1 - W_2)^n \right\}. \quad (96)$$

The overall scheme progresses in time as

$$\hat{U}^{n+1} = \hat{U}^n + \Delta \hat{U}, \quad (97)$$

where n represents the temporal index and A , B , M , and N represent the Jacobian

matrices (see Appendix B)

$$A = \frac{\partial E_1}{\partial \hat{U}} \quad B = \frac{\partial E_2}{\partial \hat{U}} \quad (98)$$

$$M = \frac{\partial V_1}{\partial \hat{U}_\xi} \quad N = \frac{\partial W_2}{\partial \hat{U}_\eta} \quad (99)$$

Application of second-order central differencing for the spatial derivatives yields as a function of nodal position (18:19)

$$\{I + \Delta t (\mu_\xi A_{i,j} - \delta_\xi^2 M_{i,j})\} \Delta \hat{U}_{i,j}^* = \quad (100)$$

$$-\Delta t \{ \mu_\xi (E_1 - V_2)_{i,j} + \mu_\eta (E_2 - W_1)_{i,j} \}$$

$$\{I + \Delta t (\mu_\eta B_{i,j} - \delta_\eta^2 N_{i,j})\} \Delta \hat{U}_{i,j} = \Delta \hat{U}_{i,j}^* \quad (101)$$

$$\xi_i = (i - 1)\Delta\xi \quad 1 \leq i \leq IL \quad (102)$$

$$\eta_j = (j - 1)\Delta\eta \quad 1 \leq j \leq JL, \quad (103)$$

with the finite-difference operators defined as (18:20)

$$\delta_\xi f_{i,j} = \frac{(f_{i+1/2,j} - f_{i-1/2,j})}{\Delta\xi} \quad (104)$$

$$\delta_\eta f_{i,j} = \frac{(f_{i,j+1/2} - f_{i,j-1/2})}{\Delta\eta} \quad (105)$$

$$\mu_\xi f_{i,j} = \frac{(f_{i+1,j} - f_{i-1,j})}{2\Delta\xi} \quad (106)$$

$$\mu_\eta f_{i,j} = \frac{(f_{i,j+1} - f_{i,j-1})}{2\Delta\eta} \quad (107)$$

The transformation derivatives (metrics) are computed directly from the grid. Second-order, central differencing is employed for interior points, while second-order, one-sided differences are employed on the boundaries. The scheme is implemented in an alternating-direction fashion by first solving equation (100) along lines of constant

ξ for $2 \leq j \leq JL-1$ followed by the solution of eqn (101) along lines of constant η for $2 \leq i \leq IL-1$. This results in a block tridiagonal system along each coordinate line due to the computational stencil brought about by the approximate factorization. The boundary equations are then solved explicitly.

Compressible flow computations are susceptible to numerical instabilities induced by nonlinear effects due to large flow gradients (e.g. shock waves and flow separation). These nonlinearities are especially prone to producing numerical instabilities at high Reynolds numbers, which in turn can slow down convergence considerably (13:322).

The oscillations induced by numerical instabilities can be damped by the inclusion of second- and fourth-order artificial viscosity in the algorithm. An explicit fourth-order damping term, D_e , is included in the right-hand side of equation (100). Two second order damping terms, D_ξ and D_η are included within the respective implicit operators in equation (101).

The equations for these added terms are (18:20)

$$D_e = -\omega_e \Delta t J_{i,j}^{-1} (\delta_\xi^4 + \delta_\eta^4) U_{i,j}^n \quad (108)$$

$$D_\xi = -\omega_i \Delta t J_{i,j}^{-1} \delta_\xi^2 J_{i,j} I \quad (109)$$

$$D_\eta = -\omega_j \Delta t J_{i,j}^{-1} \delta_\eta^2 J_{i,j} I, \quad (110)$$

where $\omega_e \sim 1$ and $\omega_i \geq 2\omega_e$.

In order to accelerate convergence for a steady flow computation, a local time step, $\Delta t_{i,j}$, is introduced. The local time step is a function of the local flow condition and the transformation metrics. The time step is controlled by the user via specification of the Courant number, C , which is utilized in the following fashion

$$\Delta t_{i,j} = C \Delta t_{max,i,j}. \quad (111)$$

The maximum local timestep, $\Delta t_{max,i,j}$, as mentioned, is then a function of the local transformation metrics and flow conditions

$$\Delta t_{max,i,j} = \left[\frac{|u|}{\Delta \xi} + \frac{|v|}{\Delta \eta} + a \sqrt{\Delta S_{\xi}^{-2} + \Delta S_{\eta}^{-2}} + \frac{2\gamma}{\rho \Delta S_{\eta}^2} \left(\frac{\mu}{Pr} + \frac{\epsilon}{Pr_t} \right) \right]^{-1} \quad (112)$$

$$\Delta S_{\xi} = \sqrt{x_{\xi}^2 + y_{\xi}^2} \Delta \xi \quad (113)$$

$$\Delta S_{\eta} = \sqrt{x_{\eta}^2 + y_{\eta}^2} \Delta \eta. \quad (114)$$

Generally, for an explicit algorithm, the Courant number must be less than one for stability. However, for the Beam and Warming implicit algorithm it can be much higher and is typically set to twenty (5:20).

3.2 Convergence Criteria

By considering only steady-state solutions, the specification of convergence criteria is simplified. In general, some small oscillation in flow variables will persist indefinitely. These oscillations may be too small to appreciably affect the solution. A suitable convergence criteria must be established to ascertain when the oscillations are satisfactorily small.

The convergence criteria used in this study follows the example of Visbal (18) and Boyles (5). Convergence was assessed by monitoring the airfoil lift and drag coefficients. The solution was assumed converged when the amplitude of the oscillations for C_l was less than 0.1 percent and the variation in C_d was less than one drag count, where one drag count equals 0.0001.

IV. Results and Discussion

This chapter presents the results obtained from the numerical study of the two differing grid topologies. The study is divided into two basic parts. The first consists of a grid refinement study using the C-grid. Progressively finer grids are employed for subsonic and transonic cases. The second part is the comparative study between the C- and O-grid topologies. An overview of the various grids employed and their construction is presented first. This is followed by the results of the C- grid refinement study and a comparative analysis between the C- and O-grid.

4.1 Grids Employed

There are procedural differences in the construction of the two grid types. The construction of C-grids is based on a straightforward application of the Barth and Kinsey code (9). The construction of O-grids is complicated by the need to enforce a finite curvature at the trailing edge, allowing the O-grid generator to function. The first step is the construction of the airfoil shape. The airfoil is then truncated at a specified point and a circular arc is affixed to form the trailing edge. The point distribution around the airfoil is then specified and the actual generation of the grid can then proceed. This procedure represents an added degree of difficulty which should be considered when comparing the two types of grid.

The grids employed in this study are listed in Tables 1 and 2. Figures 2 through 5 display the progressively finer C-grids employed. C-Grids 5 through 8, shown in Figures 6 through 9 were constructed for specialized purposes. C-grid 5 is an asymmetric grid, constructed with more points and finer spacing on the upper surface to test for better shock capturing in the transonic case. C-grid 6 was constructed with a finer leading edge spacing in an attempt to better match the experimental pressure coefficient data at that location. C-grid 7 was constructed in an attempt to smooth the gradient in the transformation metrics, especially at the

trailing edge/wake junction. C-Grid 8 represents a further attempt to smooth the metrics without sacrificing fine tangential spacing at the trailing edge. The three basic O-grids shown in Figures 10 through 12 vary at the point in which the nominal airfoil was truncated, thus they vary in the radius of curvature at the respective trailing edges. O-grid 4, shown in Figure 13, was constructed with a finer grid spacing on the upper surface to test for better shock resolution. Figure 14 shows an example of the trailing-edge geometry for the O-grids, while Figures 15 and 16 offer a comparison of leading-edge geometries for the C- and O-grids.

4.2 C-Grid Refinement Study

Two specific flow regimes were considered for the C-grid refinement study; a subsonic and transonic case. The subsonic case chosen was at $M = 0.3$, $\alpha = 4.04$ degrees, and $Re = 1,860,000$. The transonic case chosen was at $M = 0.775$, $\alpha = 2.03$ degrees, and $Re = 1,900,000$. These cases were chosen because of the availability of comparative experimental data (2) (11).

Figures 17 and 18 display the variation of pressure coefficient on the surface for the subsonic case. The differences in the plots appear most readily at the leading edge. C-grids 1 and 4 display almost identical results, each displaying a spike in C_p on the upper surface near the leading edge and generally overestimating the magnitude of C_p along the upper surface to the midchord point. A close examination reveals that C-grid 1 matches the experimental data slightly better than C-grid 4 in that range. However, an examination of similar experimental data reveals the sensitivity of the pressure distribution to angle of attack (7:58). The corrected, experimental angle of attack (as opposed to the geometric angle) is a difficult parameter to determine precisely, and is a likely cause of this discrepancy. The results using a finer leading-edge spacing (C-grid 6) are shown in Figure 19. The spike in pressure at the leading edge is slightly reduced, but the trend remains the same. The numerical results obtained are duplicated using a finer grid (299x100) by Boyles (5:43).

C-Grid	IL x JL	Pts_{up}	Pts_{lo}	Pts_{wa}	$\Delta\xi_{le}$	$\Delta\xi_{te}$	$\Delta\eta_w$	KDIST
1	119x40	35	35	25	.0125	.0250	.0020	5
2	149x60	40	40	35	.0100	.0250	.0020	10
3	179x80	50	50	40	.0075	.0200	.0004	10
4	219x100	60	60	50	.0050	.0150	.0004	15
5	229x100	70	60	50	.0050	.0150	.0004	15
6	219x100	60	60	50	.0030	.0100	.0002	15
7	219x100	50	50	60	.0030	.0400	.0004	15
8	299x60	60	40	100	.0050	.0100	.0004	5

Table 1. C-Grid Specifications

O-Grid	IL x JL	Pts_{up}	Pts_{lo}	TEC	$\Delta\xi_{le}$	$\Delta\xi_{te}$	$\Delta\eta_w$	KDIST
1	204x108	102	102	.0051c	.0050	.000150	.0004	15
2	204x108	102	102	.0025c	.0050	.000100	.0004	15
3	204x108	102	102	.0014c	.0050	.000075	.0004	15
4	204x108	102*	102	.0014c	.0050	.000075	.0004	15

* Grid spacing refined along forward surface

Table 2. O-Grid Specifications

The results for the transonic case show a greater variation with grid spacing. Figures 20 and 21 display a convergence toward the experimental data with grid refinement. As the grid becomes finer and the chordwise distribution of points increases, the numerical solution approaches the experimental data. C-Grid 5 was constructed in an attempt to fit the grid to the expected solution. The number of points on the upper surface was increased and the chordwise spacing decreased at the expected location of the shock. A slight variation of the pressure distribution is evident in Figure 22, with the shock definition slightly enhanced.

In general, there will be some variation from experimental data due to a combination of experimental error, numerical truncation error, and the need to apply artificial viscosity to achieve solution convergence. To determine the effect of the second-order artificial viscosity, the value utilized in the previous case was reduced by fifty percent. Figure 23 displays the result using C-grid 4; the reduction in artificial viscosity produced an even closer agreement with the experimental data. Comparing Figures 22 and 23 indicates that minimizing the artificial viscosity may be as or even more important in obtaining an accurate solution than an overreliance on reducing grid spacing. The importance of minimizing artificial viscosity is further demonstrated by Figure 24, in which the effect of artificial viscosity on C_l and C_d is shown. In particular, the value of C_d varies by nearly 10 percent, while C_l varies by nearly 4 percent over the range of artificial viscosities considered.

The contour plots display the same trends as the plots of C_p on the surface. Comparison of the Mach contours in Figures 25 and 26 reveals that the solution obtained with C-grid 1 exhibits a misplaced sonic line, moves the shock too far forward, and has a poor resolution of the shock wave. Figure 27 displays the experimental location of the shock at the midchord point (11:69). The solution obtained using C-grid 4 places the shock at the correct location and displays better shock resolution.

Figures 28 and 29 exhibit the dependency of convergence rate on flow conditions and grid characteristics. The plots display the oscillation of lift coefficient with

iteration number, N . Convergence is obtained for the subsonic case ($M = 0.3$) in less than 600 iterations using C-grid 2. However, increasing the Mach number to 0.775 produces a marked oscillation in C_l which persists beyond 5000 iterations. This is attributed at least in part to the point distribution in the normal direction. Referring to Table 1, C-grid 2 uses only 50 percent more points in the normal direction to cover twice the distance (i.e., ten chord lengths instead of five). The poor point distribution can contribute to numerical error, which is then further exacerbated by large flow gradients. When additional points are added in the normal direction, the problem ceases, as revealed by Figure 30.

4.3 Comparison of C-grid and O-Grid Results

Three regimes are chosen for comparative purposes: subsonic, transonic, and supersonic. Experimental data is used as the yardstick of measure in the subsonic and transonic cases, while the differences in flow structure is considered in the supersonic case. In general, the higher the Mach number, the more differences appear in the solutions between the two grid types. Only small differences are noticed in the subsonic regime, while more significant differences are noted for the other cases.

4.3.1 Subsonic Case Of the first three O-grids employed, (see Table 2) the only difference is the point at which the trailing edge is truncated and the circular arc affixed. Of course, the further aft this truncation occurs, the smaller the radius of curvature of the arc. In general there was little difference in the solutions obtained using these three grids. Comparing Figures 31 and 32 reveals no discernable difference in the plots. Figure 31 reveals the effect of the truncation at approximately $x = .97$, where the data is similarly truncated. However, the pressure distribution over the remainder of the surface is largely unaffected. The integrated variables, C_l and C_d , are also comparable. The variation of C_l and C_d is less than 2 percent when comparing O-grids 1 and 3, and less than 0.5 percent when comparing O-grids 2 and 3.

Comparing these results with those of C-grids 4 and 6 for the subsonic case (Figures 18 and 19) shows a similar agreement with two exceptions: the leading and trailing edges show slight differences. At the leading edge, C-grid 4 displays a greater pressure spike on the upper surface. Only when the leading-edge spacing is reduced to .003 (C-grid 5) do the pressure values agree very closely at that location. When equal spacing is specified at the leading edge, the O-grid performs slightly better. Note that the specification of equal spacing does not enforce an equal point distribution in the region near the leading edge for the C- and O-grids. This can be seen in Figures 5 and 12; the point distributions are similar but not exact. There is also some variation in C_p at the trailing edge. The averaging procedure applied to the boundary conditions in the wake for the case of the C-Grid may induce some oscillatory behavior there. The O-grid has no branch cut in the wake and so this difficulty does not arise. See Appendix C for a discussion of these boundary conditions.

The comparison of lift coefficient versus angle of attack is presented in Figure 33. Results are presented for Reynolds number 6,000,000. The experimental data (1:462) represents an average of the results presented for this value of Reynolds number. The agreement with this data indicates that the turbulence level for the experiment could not be precisely matched, since the only differences in the experimental data was the transition point and turbulence level. Transition was specified at the leading edge for both C- and O-grids in the numerical code, attempting to match the experimental case where .011 inch grain was applied at the leading edge. The numerical results show excellent agreement up to 10 degrees angle of attack. Past this point there is some variation, with the O-grid correctly predicting α_{stall} at approximately 12 degrees. The data curve truncates at the twelve degree point for the C-grid because the solution diverged at higher values.

4.3.2 Transonic Case In the transonic case, there again is no discernable difference in the pressure distribution on the surface between O-grids 1, 2, and 3,

as shown by Figures 34 and 35. The data is truncated near the trailing edge for O-grid 3, as noted in the subsonic case, but the overall distribution remains unaffected. However, a comparison with the result of C-grid 4, also shown Figure 34, indicates that the C-grid, with equal values set for second- and fourth-order artificial viscosity, performed slightly better in predicting C_p in the vicinity of the shock wave. In an attempt to match this result, the chordwise grid spacing was reduced forward of the shock wave for O-grid 5. However, the C-grid still outperformed the O-grid in matching the experimental data, as the results of Figure 36 fail to show any improvement.

A comparison of Mach contours shows two deficiencies of O-grid 3 vis-à-vis C-grid 4. See Figures 25 and 37. Firstly, the O-grid displays a poorer resolution of the shock wave, with the shock wave positioned too far forward. Secondly, the O-grid displays large errors in the wake region. The O-grid has a large concentration of grid points directly aft of the trailing edge. However, beyond $x \approx 1.3$ the grid spacing becomes larger. This inadequate resolution produces the choppy, stairstep type of contour seen in the wake of Figure 37. O-grid 5 was constructed specifically to address the first problem. The result is seen in Figure 38. The resolution of the shock wave for this case equals that produced by the C-grid. In addition the small contour directly aft of the shock wave is nearly identical to that of the C-grid, in contrast to the previous case. The O-grid solution still places the shock wave slightly forward of the C-grid shock wave, but the overall definition is much improved. However, the shifting of points to the surface has the result of reducing still further the number of points in the wake. The deficiency noted in the wake for O-grid 3 thus becomes even more severe for O-grid 4.

Interestingly, contours of C_p indicate a deficiency of the C-grid. Upon examination of Figure 39, the contour in the wake reveals a small oscillation that occurs directly along the branch cut. This oscillation is most likely due to the handling of the boundary conditions along the cut. The corresponding O-grid plot, Figure 40,

has a similar contour in the wake, but lacks the oscillation apparent in the C-grid case. In general, the same comments apply to the pressure contours in terms of shock location and resolution as for the Mach contours, i.e., the O-grid solutions display comparable shock resolution only if a particular effort is made to concentrate points in the vicinity of the shock.

The comparison of vorticity between the two grids, shown in Figures 42 and 43, display similar profiles. However, the inadequate resolution of the O-grid wake is again apparent in the step-like curves occurring there.

4.3.3 Supersonic Case The supersonic case considered is not compared with experimental data as in the previous two cases. The conditions, $M = 1.1$, $\alpha = 6^\circ$, exceed the design specifications of the airfoil and experimental data in this regime is very limited and somewhat suspect (10:3). However, a comparison can still be made based on global flow characteristics.

Contour plots of Mach contours, C_p , and vorticity are presented in Figures 44 through 51. All of the O-grid plots display the weakness noted earlier of inadequate resolution in the wake. The contours there are generally choppy and ill-formed, just as in the previous cases. The resolution of the lambda shock forming at the trailing edge is generally quite good for the O-grid, superior to that of the C-grid. This is apparent for both the Mach and C_p contours. An examination of O-grid 3 (Figure 12) reveals why this is the case; the O-grid typically has a pronounced clustering of points near the trailing edge, nearly coincident with the formation of the shock wave. This aids the resolution of the shock wave, at least near the body.

The corresponding C-grid plots (Figures 45, 47, and 49) display an obvious shortcoming in the large amounts of numerical noise in the region around the shock wave. These disturbances are certainly nonphysical and appear most strongly just prior to the shock wave. They appear to dampen as they propagate through the shock and further downstream. The plot of vorticity is most interesting, as the

disturbances appear to outline the grid elements themselves. It can be concluded that these disturbances do not arise from the handling of the branch cut in the wake, previously implicated in other cases for two reasons. Firstly, the flow remains supersonic after the oblique shock and so downstream errors should not propagate upstream, and secondly, the disturbances appear to dampen out, not magnifying, as they approach the wake. For these reasons, the most likely source of this error is the transformation metrics themselves. This hypothesis was tested by constructing C-grid 8 in an attempt to smooth the metrics in the region where the numerical noise was generated. The results obtained utilizing C-grid 8 are shown in Figures 50 and 51. The Mach contours display very little numerical noise in the region forward of the shock, however, numerical noise persists aft of the shock wave. The vorticity contours display the same trend. The large amounts of numerical noise forward of the shock wave evident in Figure 49 are completely absent in Figure 51. However, the numerical noise persists aft of the shock wave. See the section on the comparison of the transformation metrics for a further discussion of this point.

4.3.4 Convergence Rate Comparison There are minor differences in the convergence properties for the C- and O-grids. Plots of C_l and C_d are presented in Figures 52 through 55 for the subsonic and transonic cases. In general, the oscillations in C_l and C_d are more pronounced for the O-grid than the C-Grid for the subsonic case. Convergence is attained for the O-Grid solution in about 1400 iterations, while the oscillations occurring in the case of the C-grid exhibit less amplitude, with convergence attained in about 1100 iterations. For the transonic case, the C-grid solution converges in 1700 iterations while the O-grid solution converges in 2000 iterations.

This difference in convergence rate is due in part to the smaller minimum time step which must be specified to avoid divergence in the case of the O-grid. The local time step, being a function of grid spacing, essentially becomes too large around the trailing edge of the O-grid, where the tangential spacing is extremely small. Decreasing the user specified time step with respect to the C-grid value allows the

O-grid solution to converge. It is significant that there are particular cases for which the O-grid solution converges while the C-grid solution diverges. For example at $M = 0.3$, $\alpha = 13^\circ$, and $Re = 6,000,000$ the O-grid solution converges while the C-grid solution diverges. This occurs despite lowering the minimum timestep for the C-grid (as well as the CFL input). The typical mechanism for divergence is the appearance of a negative value of temperature in the field. In terms of convergence criteria, the C-grid solution exhibits less oscillation in the integrated variables and tends to converge somewhat sooner, while the O-grid solution converges for more critical flow conditions when the C-Grid solution diverges. This suggests that a different source of numerical error is occurring to produce the difficulties mentioned.

4.4 *Comparison of Transformation Metrics*

There is a significant difference in the appearance of the transformation metrics between the C-grid and O-grid topologies. It is most intuitive to display the metrics in terms of geometric parameters such as the Jacobian, orthogonality, and aspect ratio (8). Figures 56 and 57 display aspect ratio contours for C-grid 4 and O-grid 3 respectively. The basic structure of the contours is similar, there are some differences in the leading-edge area, while both display a steeper gradient in the area above and below the trailing edge. The contours for the O-grid are generally more rounded, while the C-grid displays a cusp in the transition to the wake region.

The departure from orthogonality is displayed in Figures 58 and 59. Both grids are nearly orthogonal in the wake, i.e., $\cos(\theta) \approx 0$. The largest differences here are at the leading edge. Surprisingly, the C-grid exhibits a larger departure from orthogonality in the region around the leading edge and above and below the leading edge. This may partially explain why the C-grid requires a finer grid spacing at the leading edge to match the more accurate O-grid performance there, as discussed earlier.

Contour plots of the Jacobian, or the area ratio between the physical and

computational domains, are presented in Figures 60 through 63. Some significant differences are evident between the C- and O-grid cases. The C-grid displays a distinct cusp above and below the trailing edge of the airfoil. The O-grid has a much smoother transition in this area and the contours display such cusp. The numerical error will be a function, in part, of the gradient in the transformation metrics. Therefore, at the cusp point, the C-grid will generate metric-induced errors that are larger than those of the O-grid. This offers a possible explanation for the numerical oscillations occurring in the supersonic case. The oscillations occur in precisely the region where the gradient of the Jacobian displays a discontinuity, corresponding to a cusp in the Jacobian contours. The O-grid displays a well behaved gradient there, and no such oscillations occur.

In an attempt to rectify this situation, C-grid 7 was generated with the intent of smoothing the metric gradients (see Figure 8). It was hoped that this would allow a better solution and perhaps allow convergence for several C-grid cases which diverged. However, this attempt was a failure because the means chosen to accomplish the smoothing was inadequate. Smoothing was accomplished by transferring points from the airfoil surface to the wake and increasing the specified spacing at the trailing edge. Figure 62 reveals that significant smoothing of the Jacobian contours was achieved. However, this apparently increased the total truncation error due to increased grid spacing to the extent that any improvement due to smoothing the metrics was not discernable. A difficult trade-off occurs within the constraint of a fixed number of grid points. This involves allowing sufficient grid resolution in critical flow areas while dispermitting any abrupt changes in the metrics. Optimizing this trade off may reduce the total truncation error.

C-grid 8 (see Figure 9) was also generated with the intent of smoothing the metric gradients. The goal was to reduce the large amounts of numerical noise evident in the C-grid solution for the supersonic case (see Figures 45 and 49). The method employed to achieve smoothing was to enforce uniform tangential spacing

from $x = 0.8$ to $x = 1.0$ (the trailing edge). The result on the Jacobian contours is evident in Figure 63. The smoothing is effective forward of the trailing edge, but the cusp still remains at $x = 1.0$, since the uniform spacing was not maintained beyond this point. There is a strong correlation between the Jacobian contours and the vorticity contours seen in Figure 51. The large amounts of numerical noise evident in Figure 49 is completely gone in the region forward of the shock wave in Figure 51. This corresponds to the region in Figure 63 where the metric smoothing occurs. However, the numerical noise persists aft of the shock wave, since the magnitude of the metric gradients are unaltered beyond $x = 1.0$. The overall reduction in the level of numerical noise could also be attributed to finer grid spacing (irregardless of the metrics). However, a comparison with the midchord shock wave occurring in the transonic case (see Figure 26), shows no numerical noise evident, despite a relatively coarse tangential spacing. It is pertinent that the Jacobian contours are well behaved in the midchord region. Therefore, it is inferred that the coincidence of large flow gradients and large metric gradients contribute to the type of numerical noise seen in Figure 49.

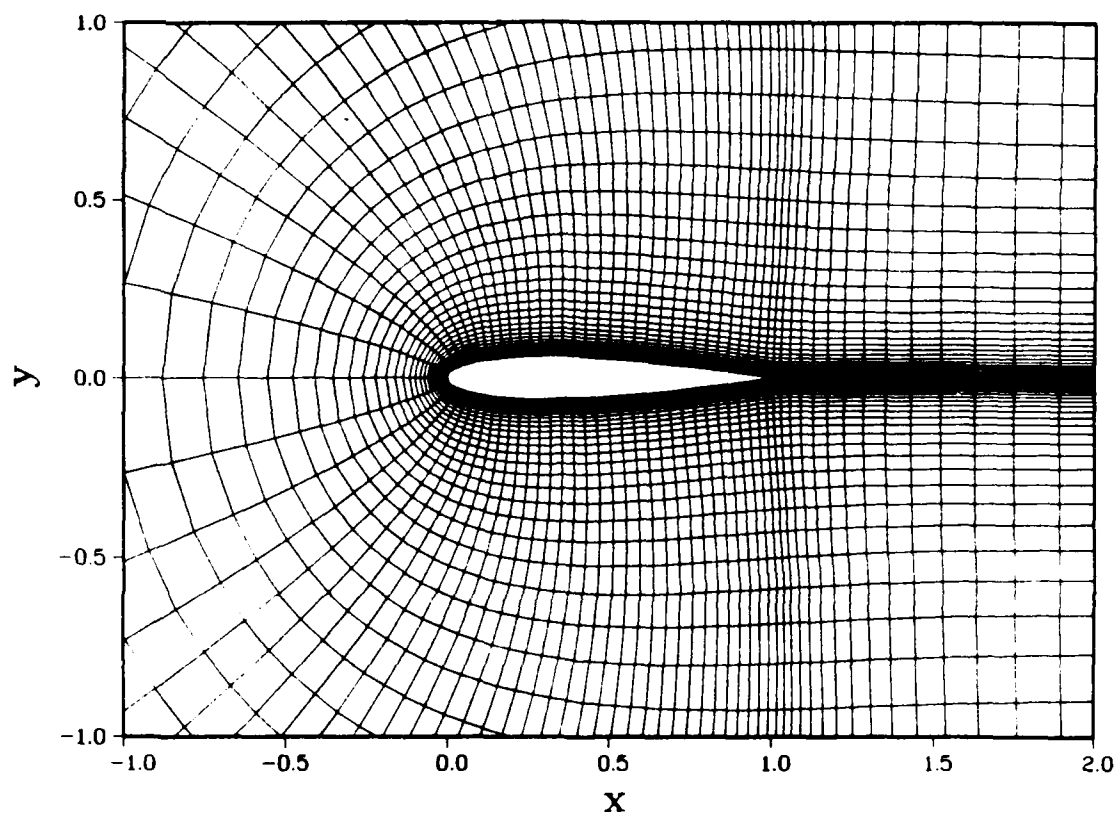


Figure 2. C-grid 1 (119x40)

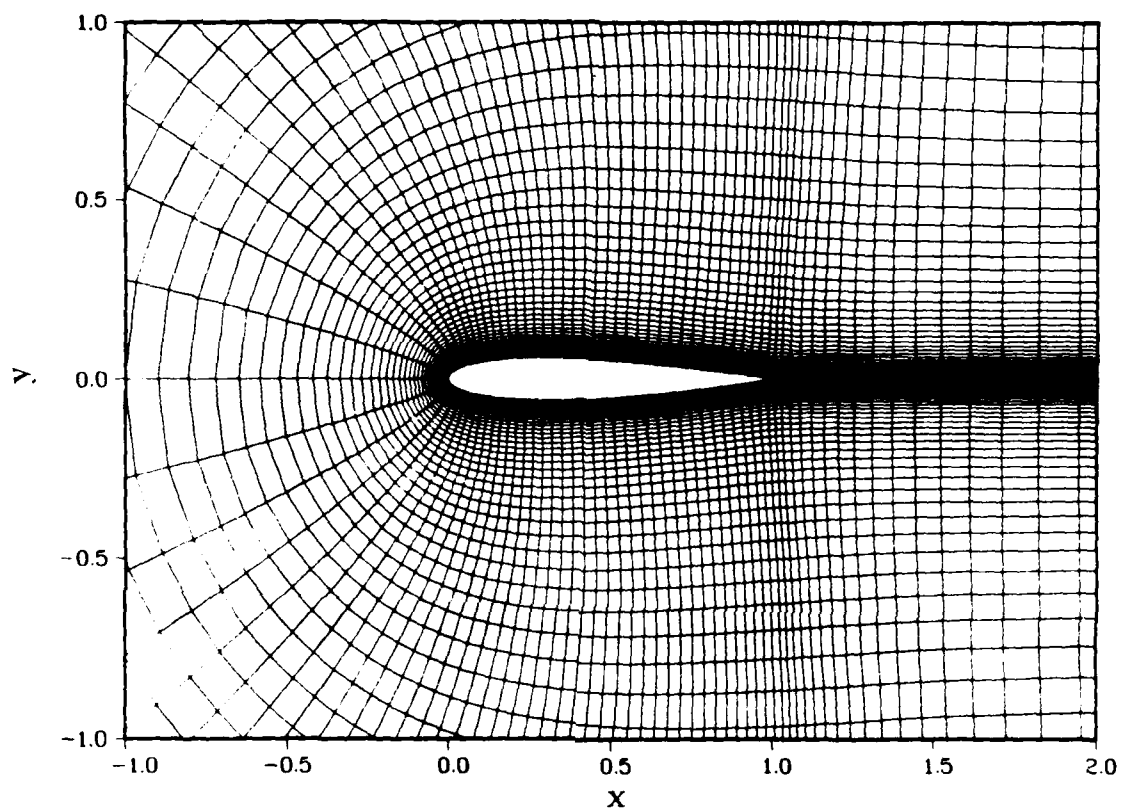


Figure 3. C-grid 2 (149x60)

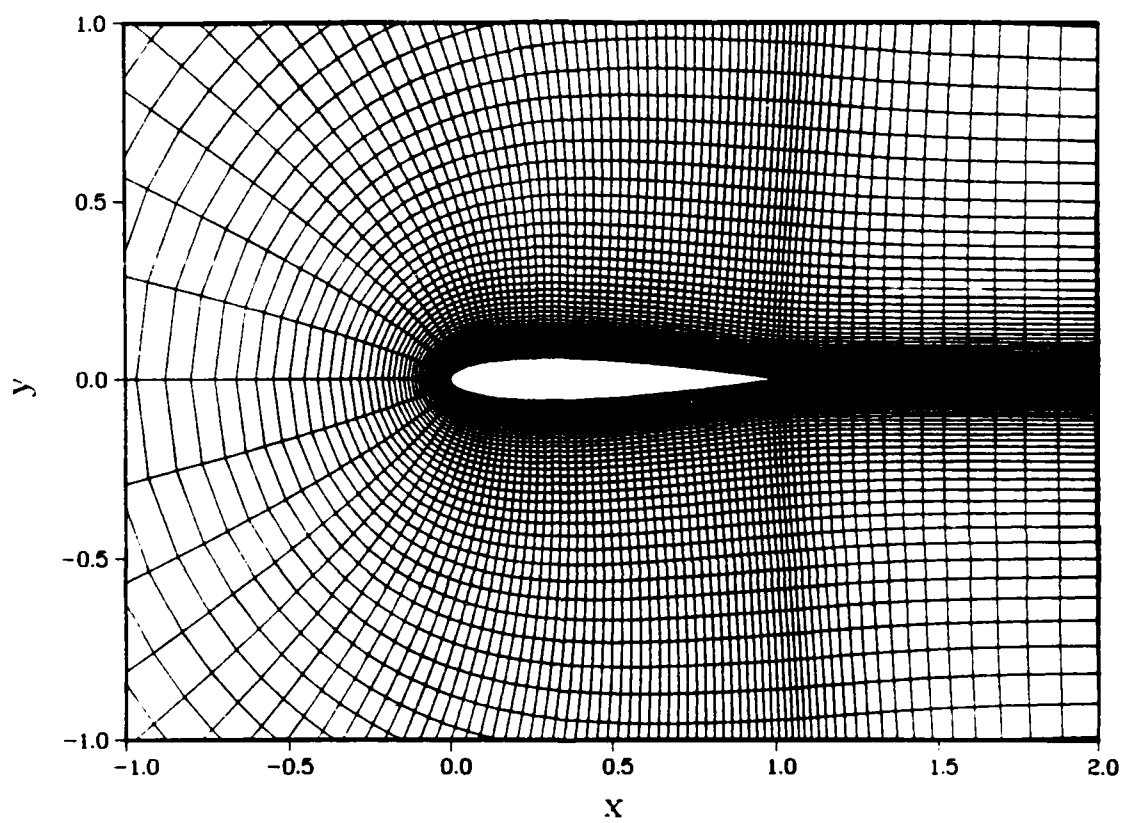


Figure 4. C-grid 3 (179x80)

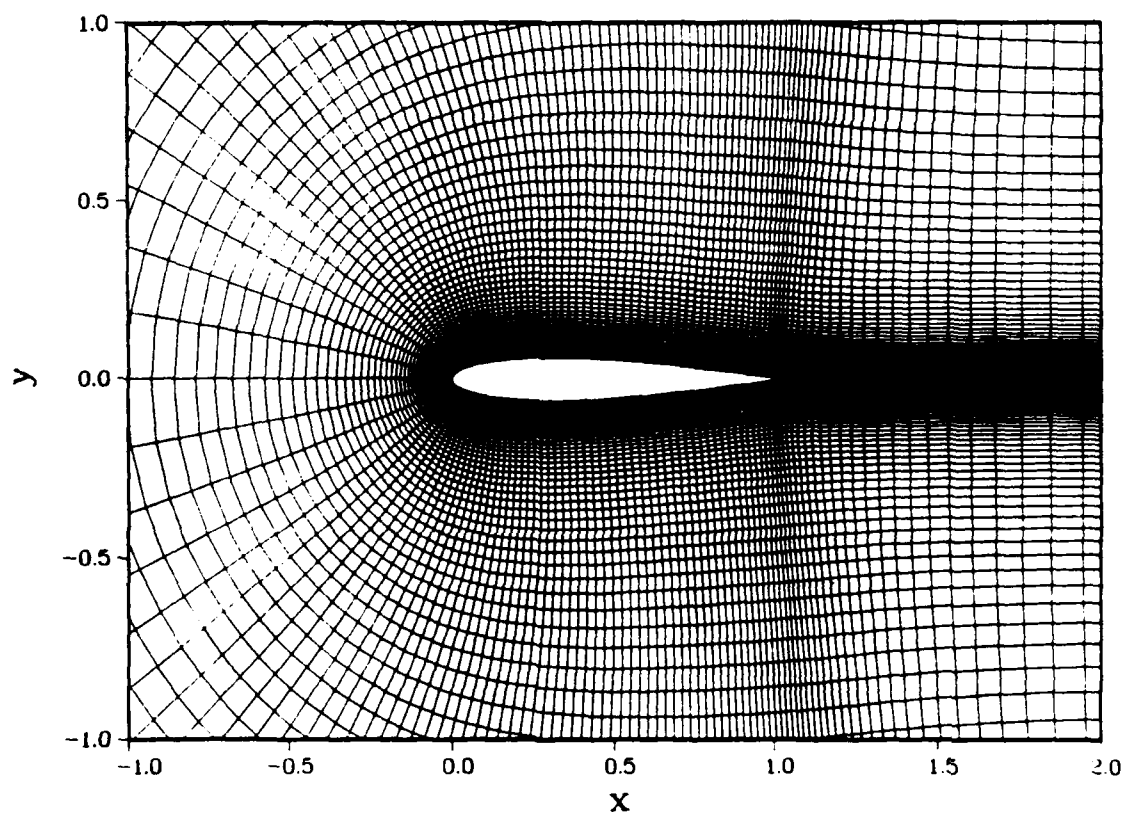


Figure 5. C-grid 4 (219x100)

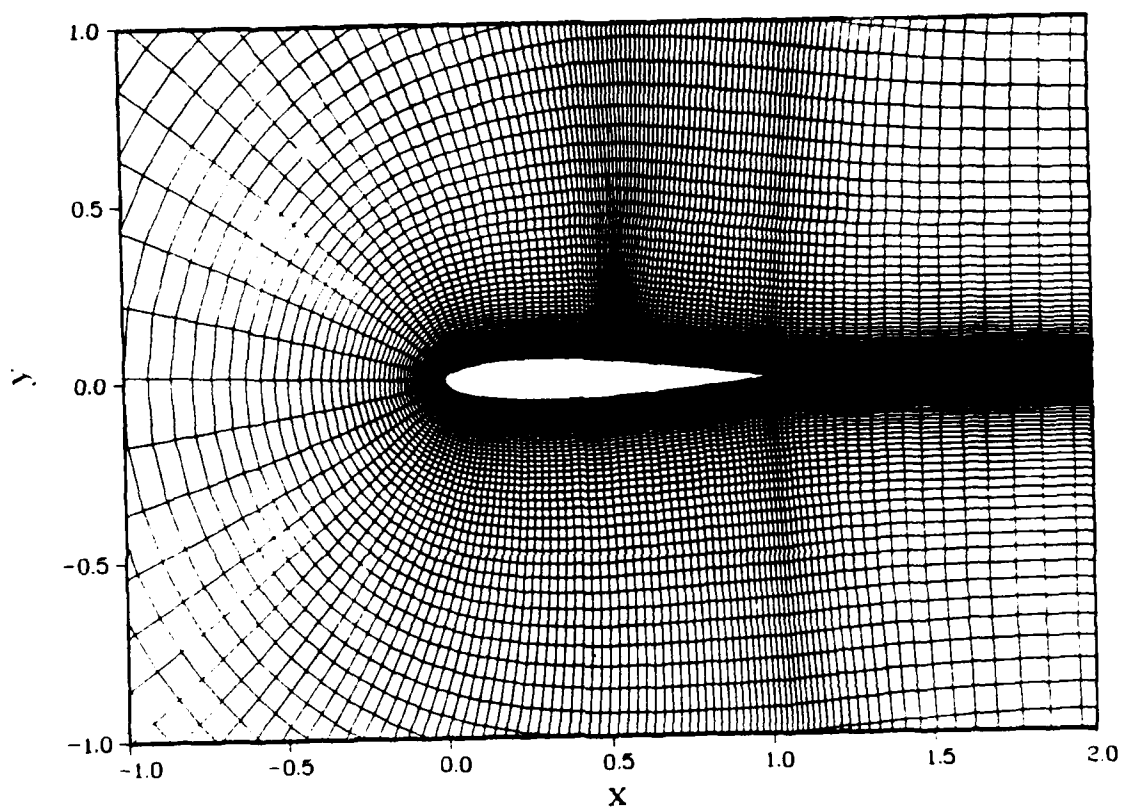


Figure 6. C-grid 5: Refined Spacing for Shock (229x100)

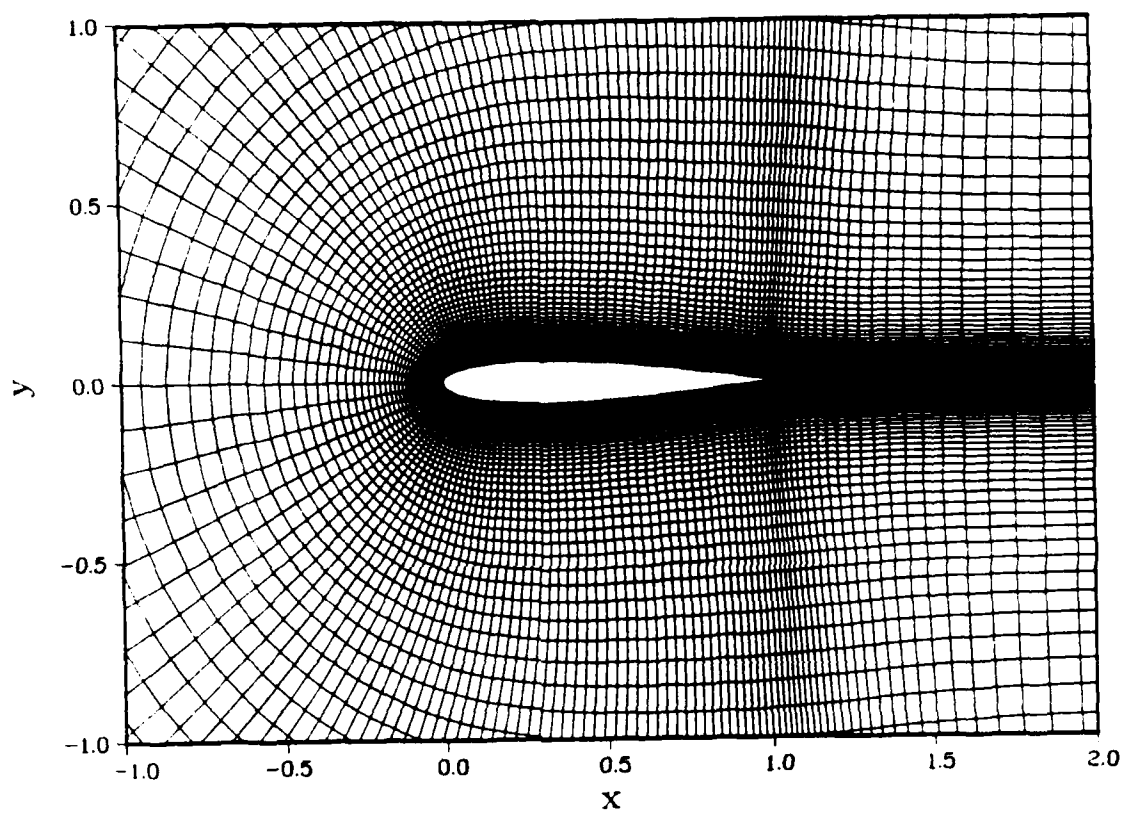


Figure 7. C-grid 6: Modified Leading-Edge Spacing (219x100)

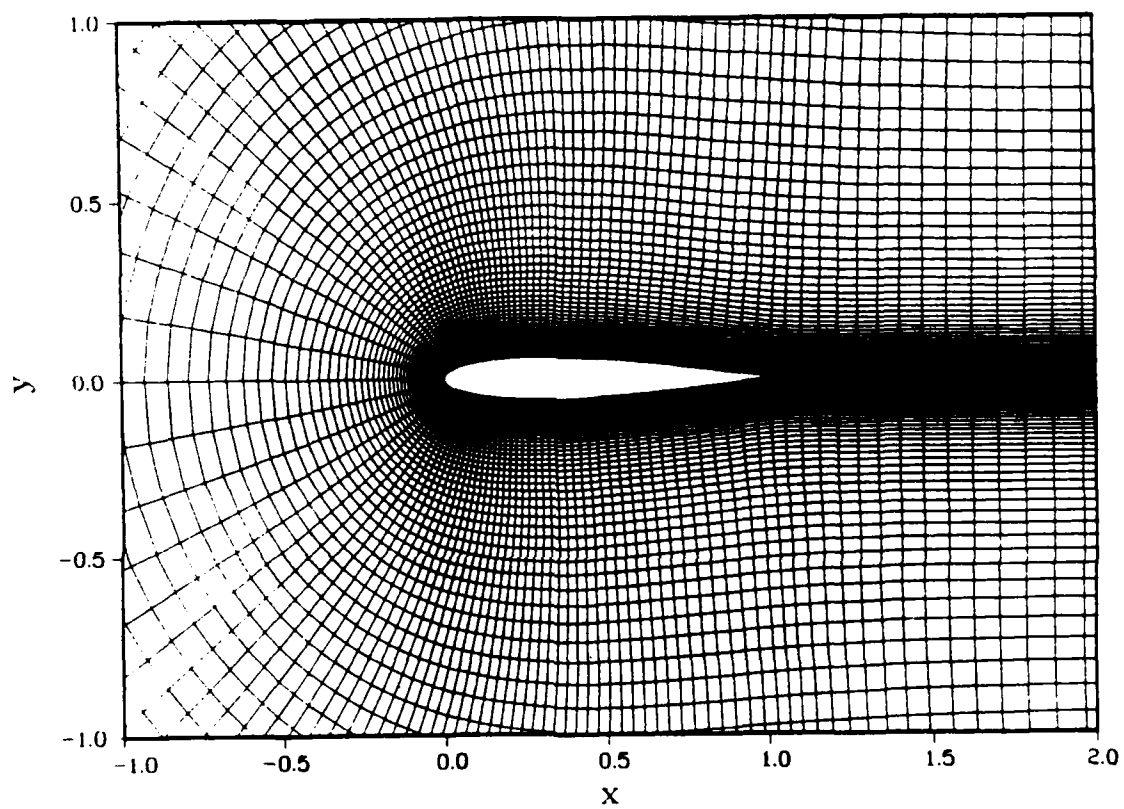


Figure 8. C-grid 7: Metrics Smoothed (219x100)

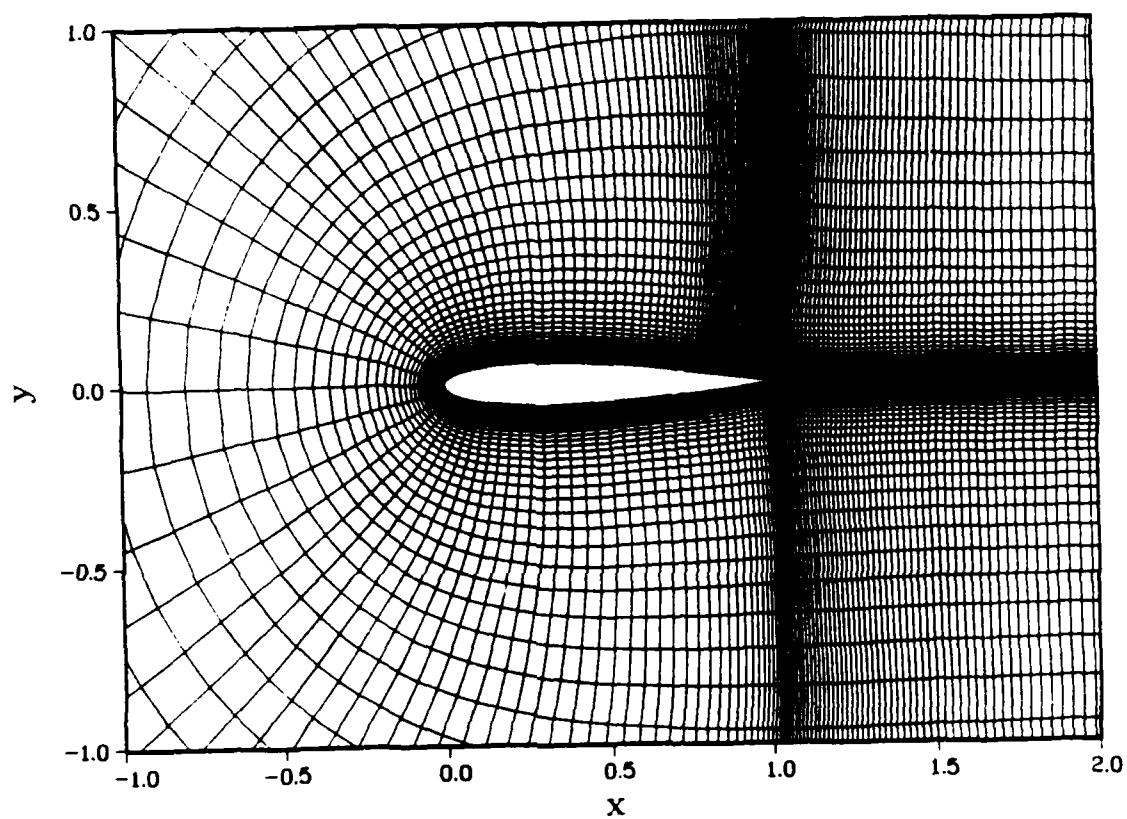


Figure 9. C-grid 8: Metrics Smoothed (299x60)

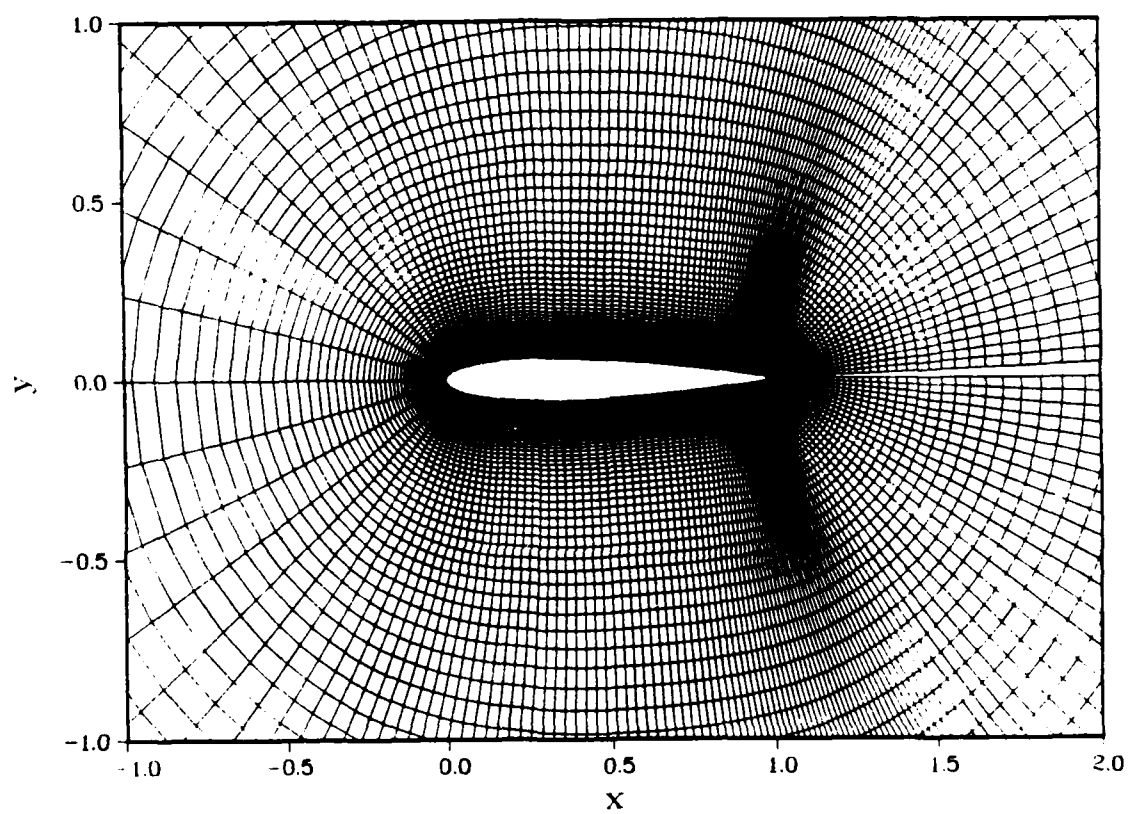


Figure 10. O-grid 1: .0051c TEC (204x108)

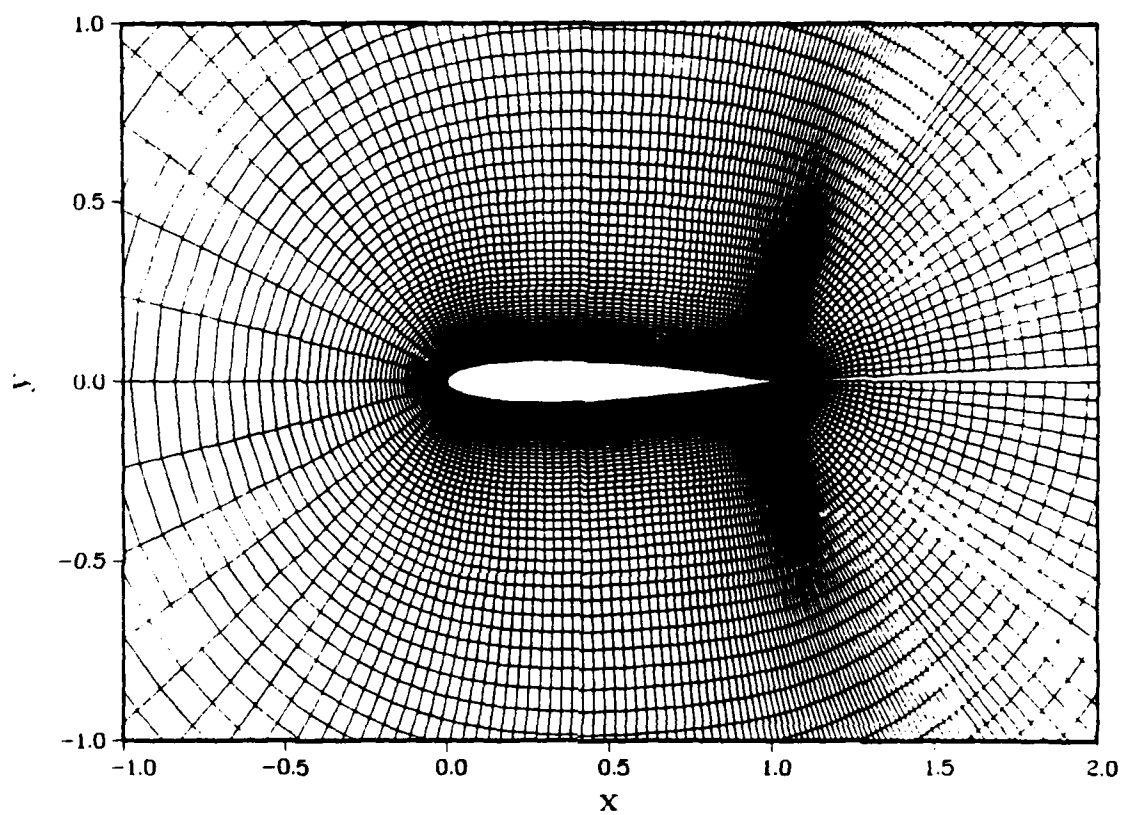


Figure 11. O-grid 2: .0025c TEC (204x108)

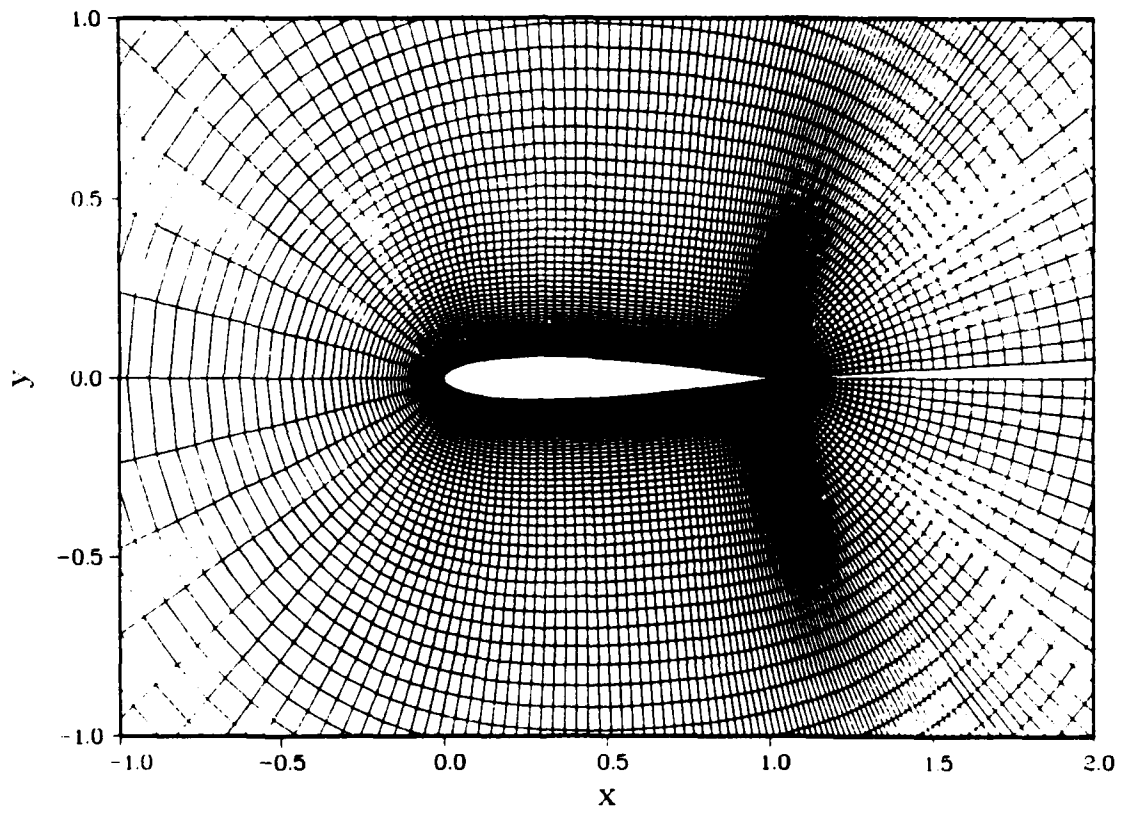


Figure 12. O-grid 3: .0015c TEC (204x100)

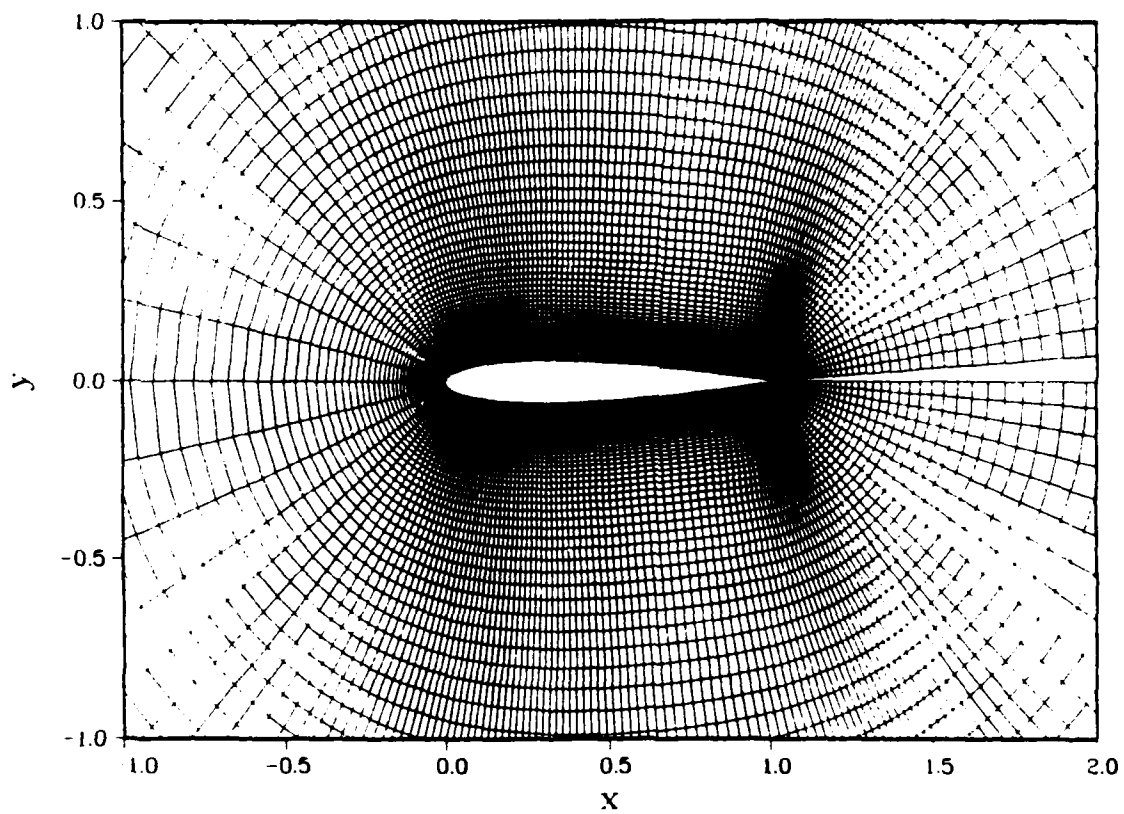


Figure 13. O-grid 4: .0015c TEC Modified Spacing (204x108)

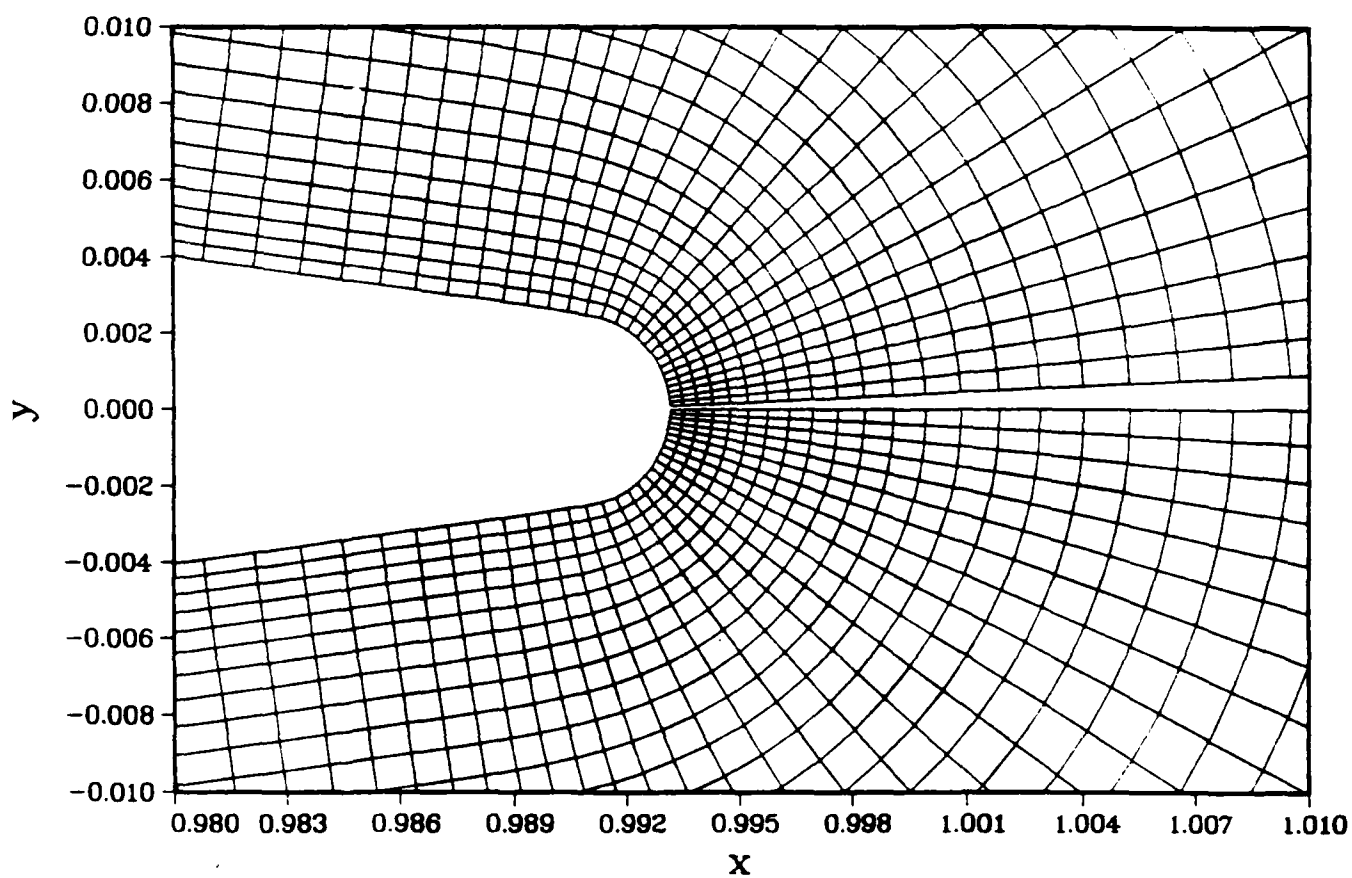


Figure 14. O-grid 2: Trailing-Edge Geometry

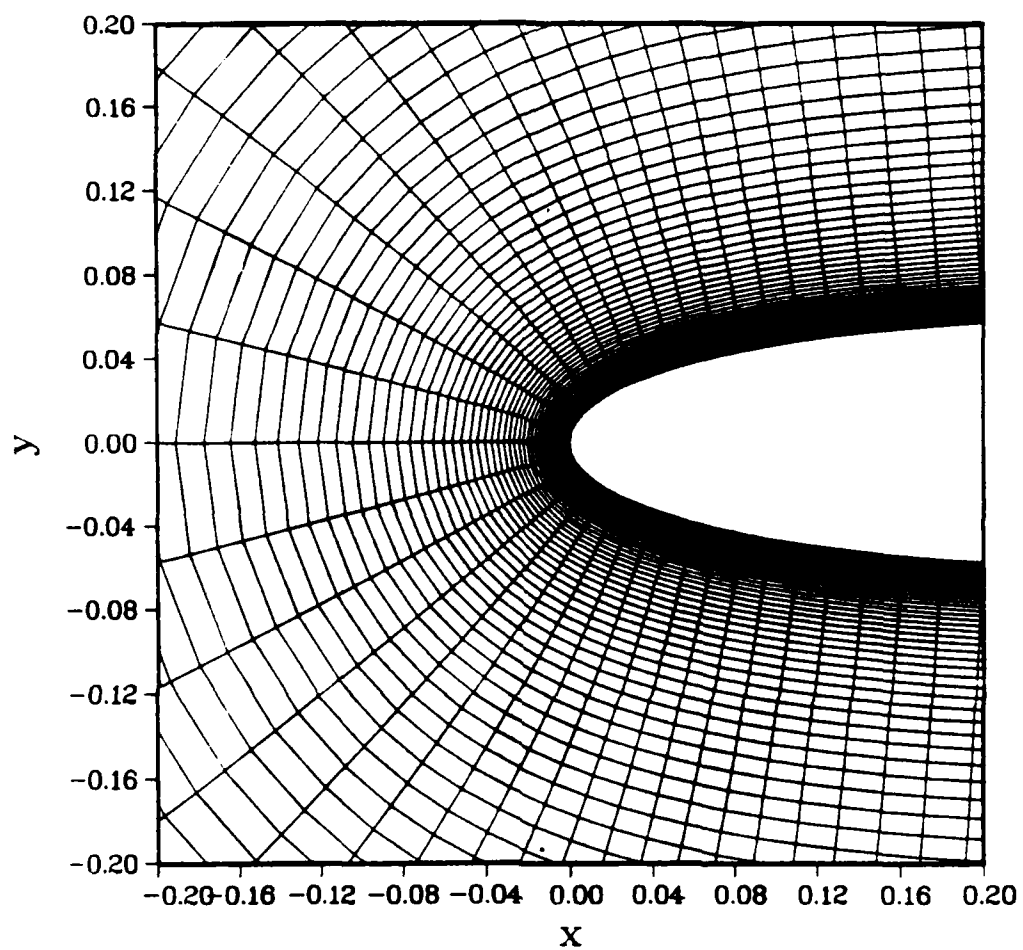


Figure 15. O-grid 3: Leading Edge Geometry

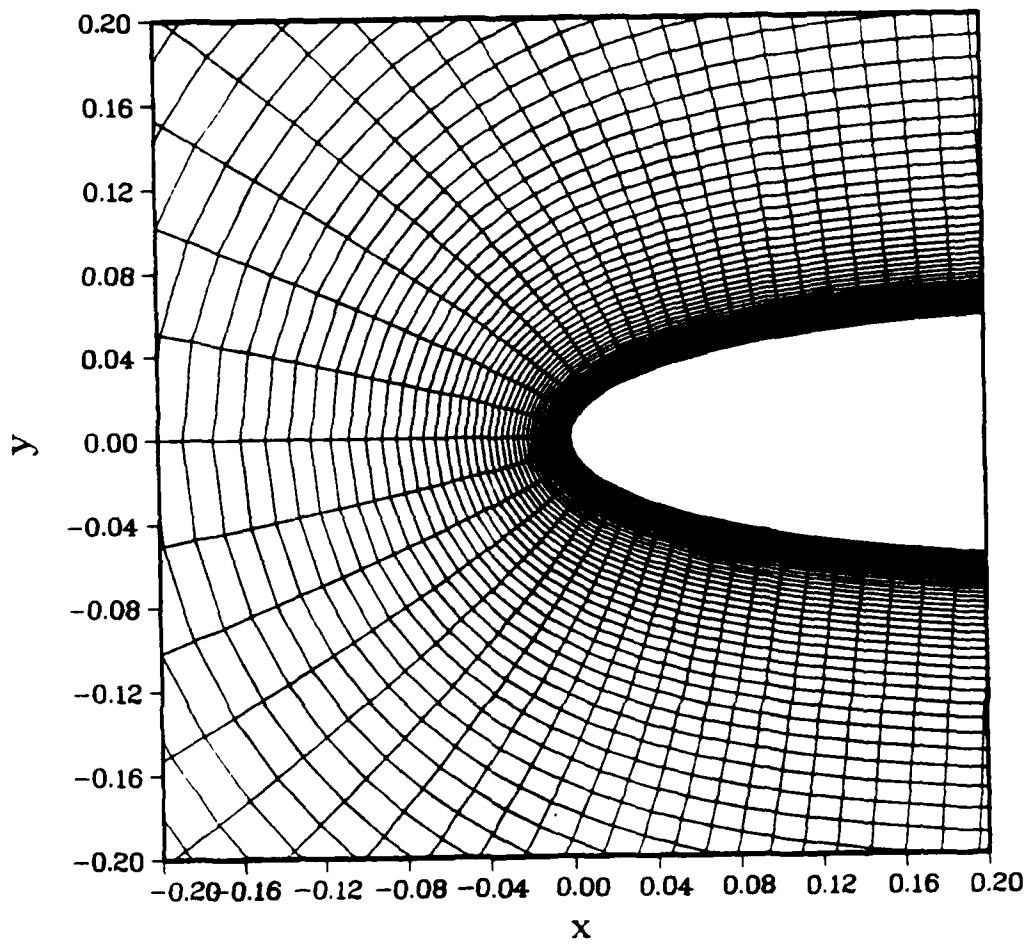


Figure 16. C-grid 4: Leading Edge Geometry

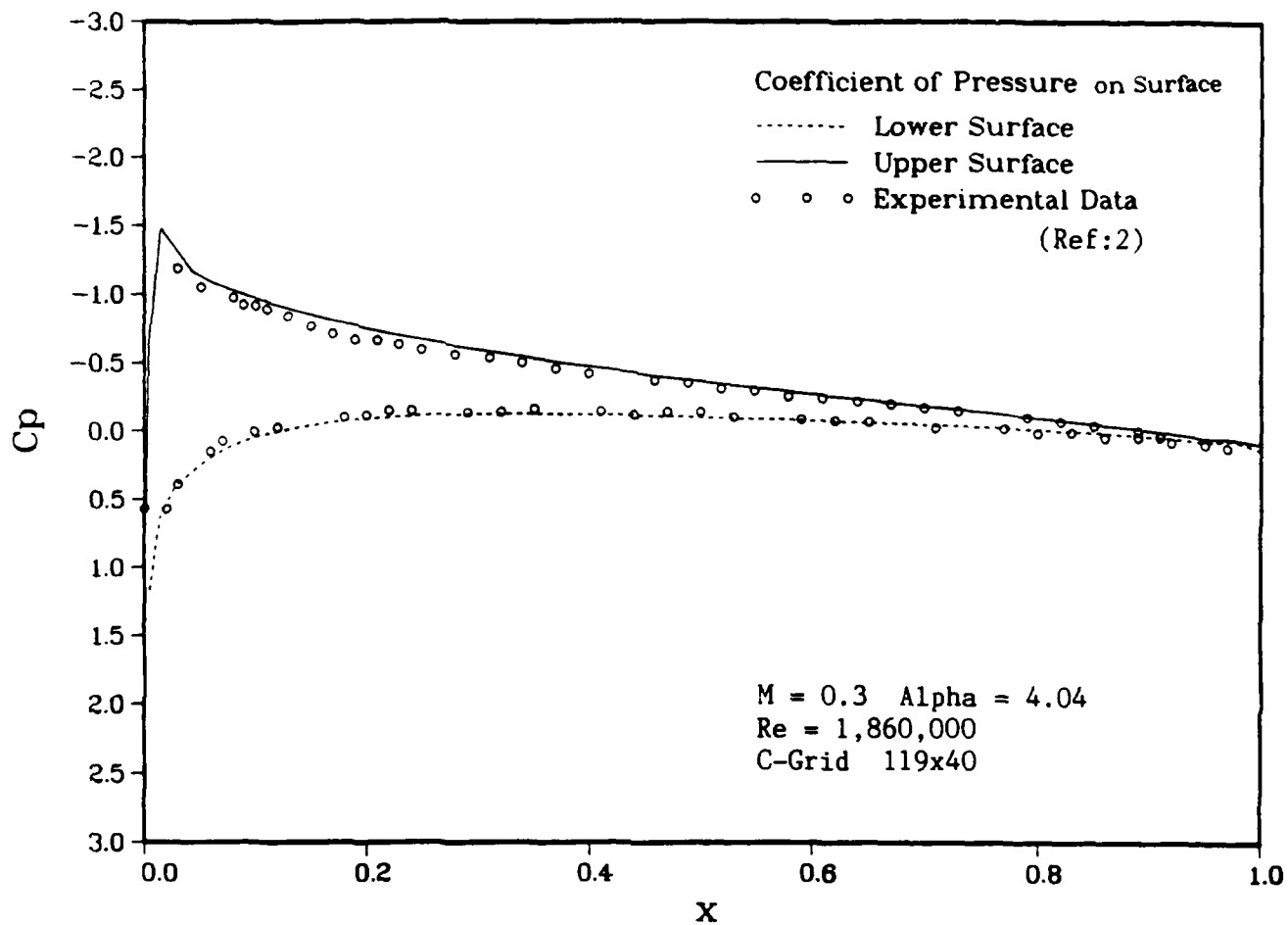


Figure 17. C-grid 1: Subsonic Pressure Coefficient Profile

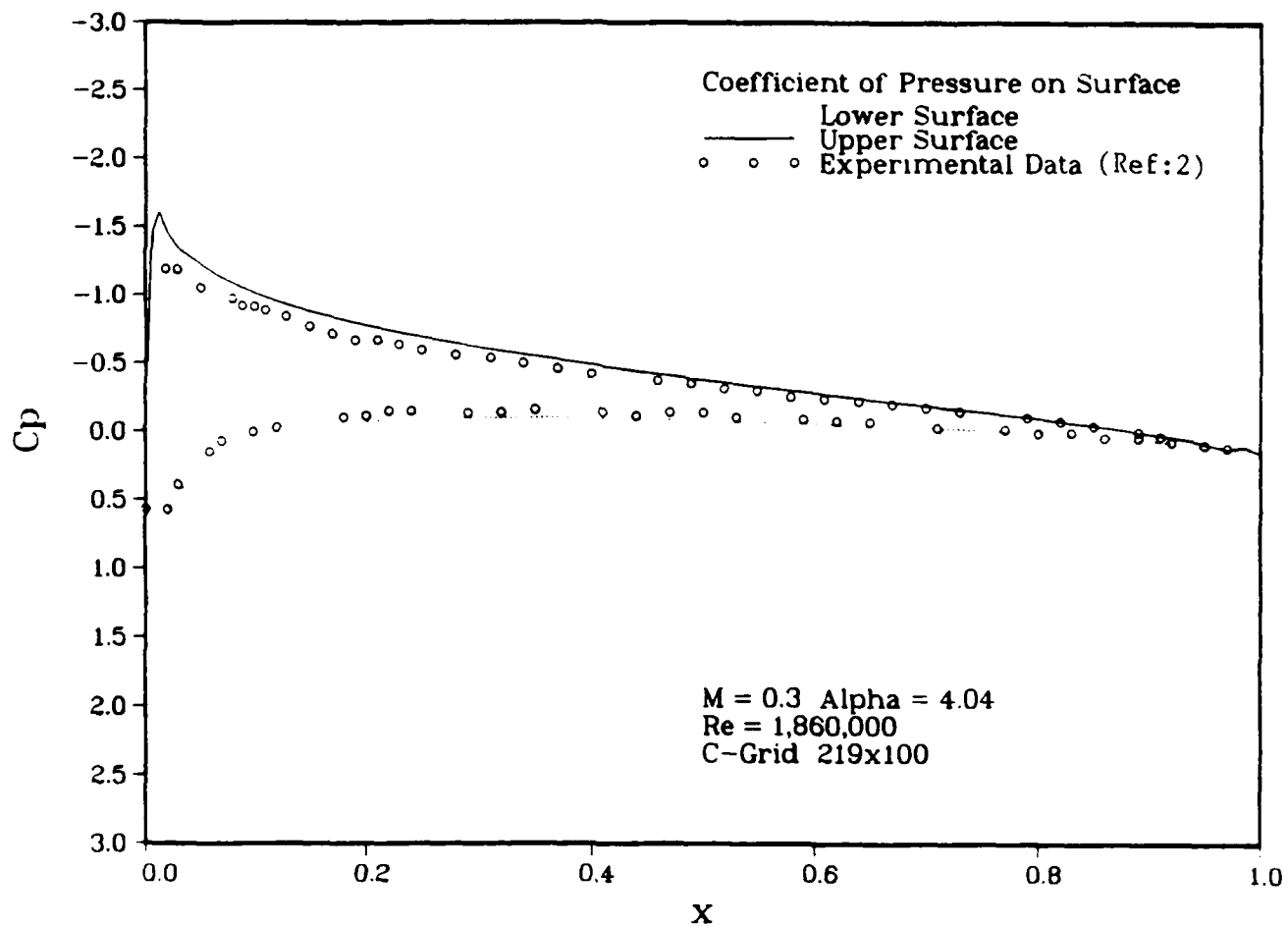


Figure 18. C-grid 4: Subsonic Pressure Coefficient Profile

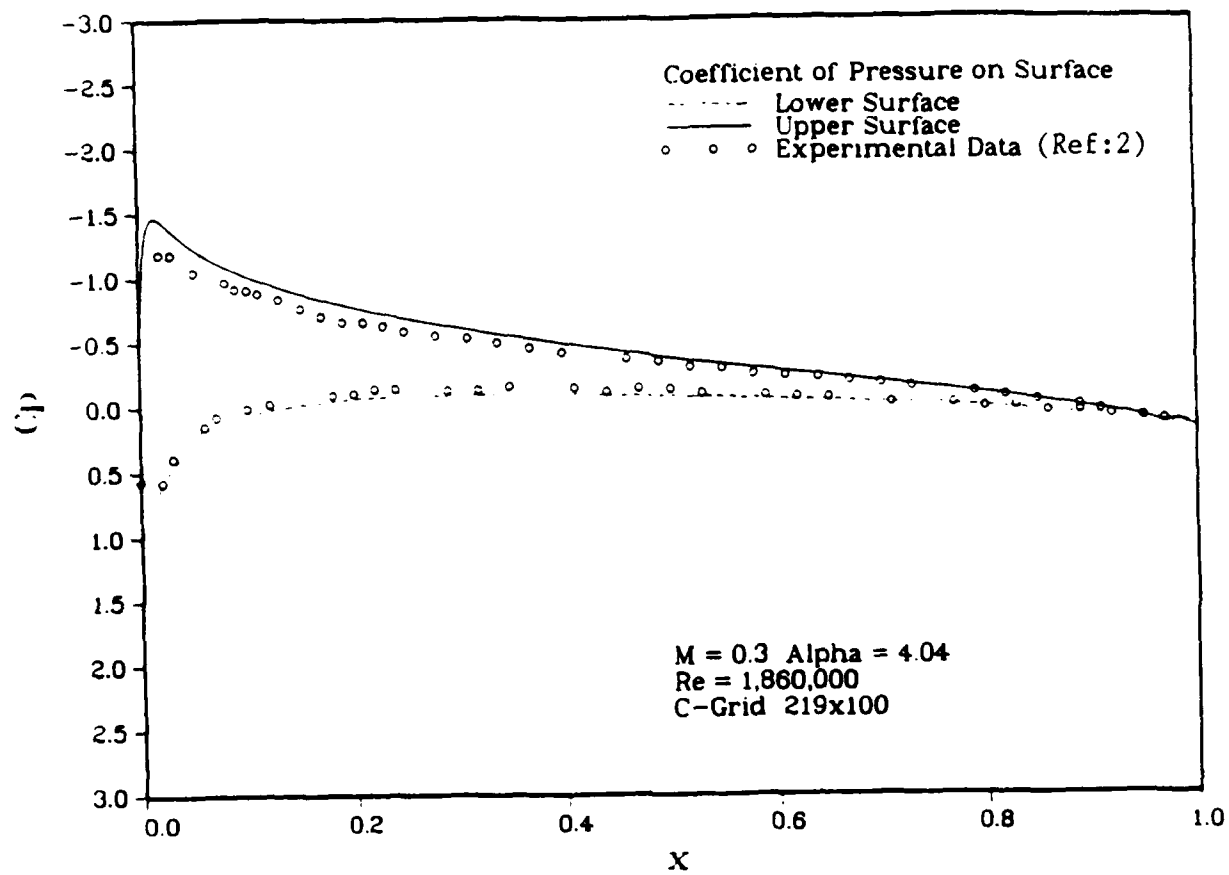


Figure 19. C-grid 5: Subsonic Pressure Coefficient Profile

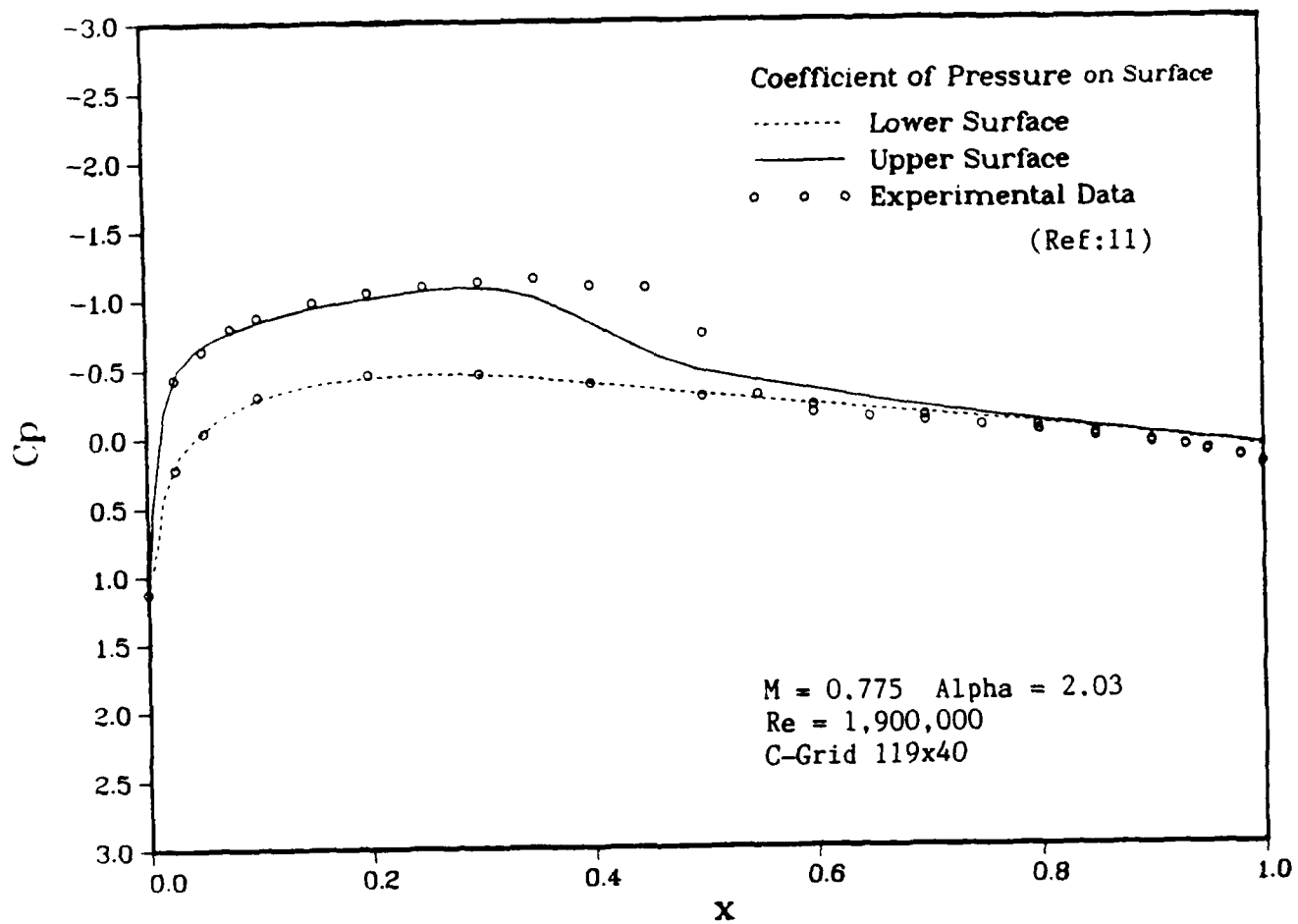


Figure 20. C-grid 1: Transonic Pressure Coefficient Profile

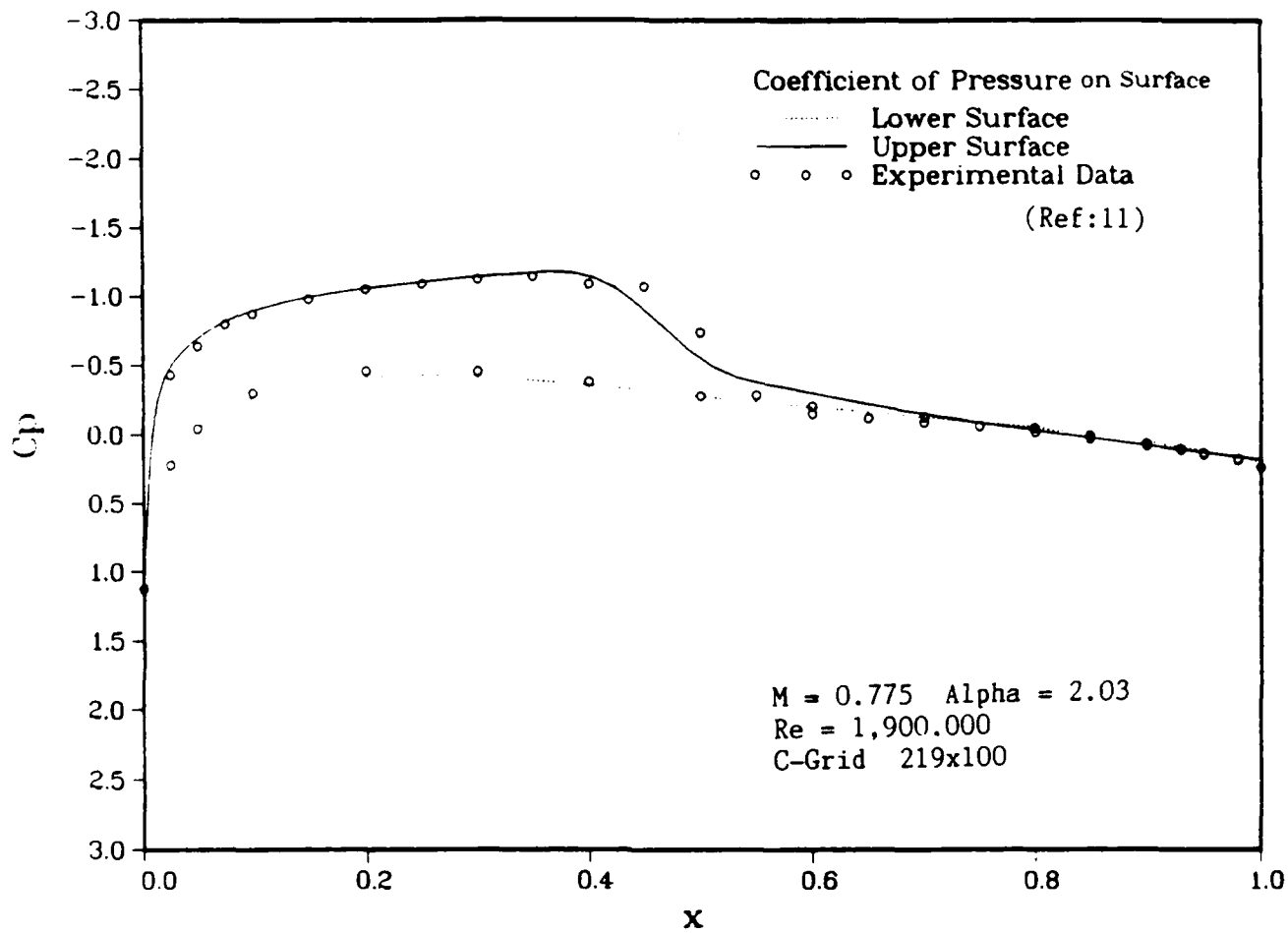


Figure 21. C-grid 4: Transonic Pressure Coefficient Profile

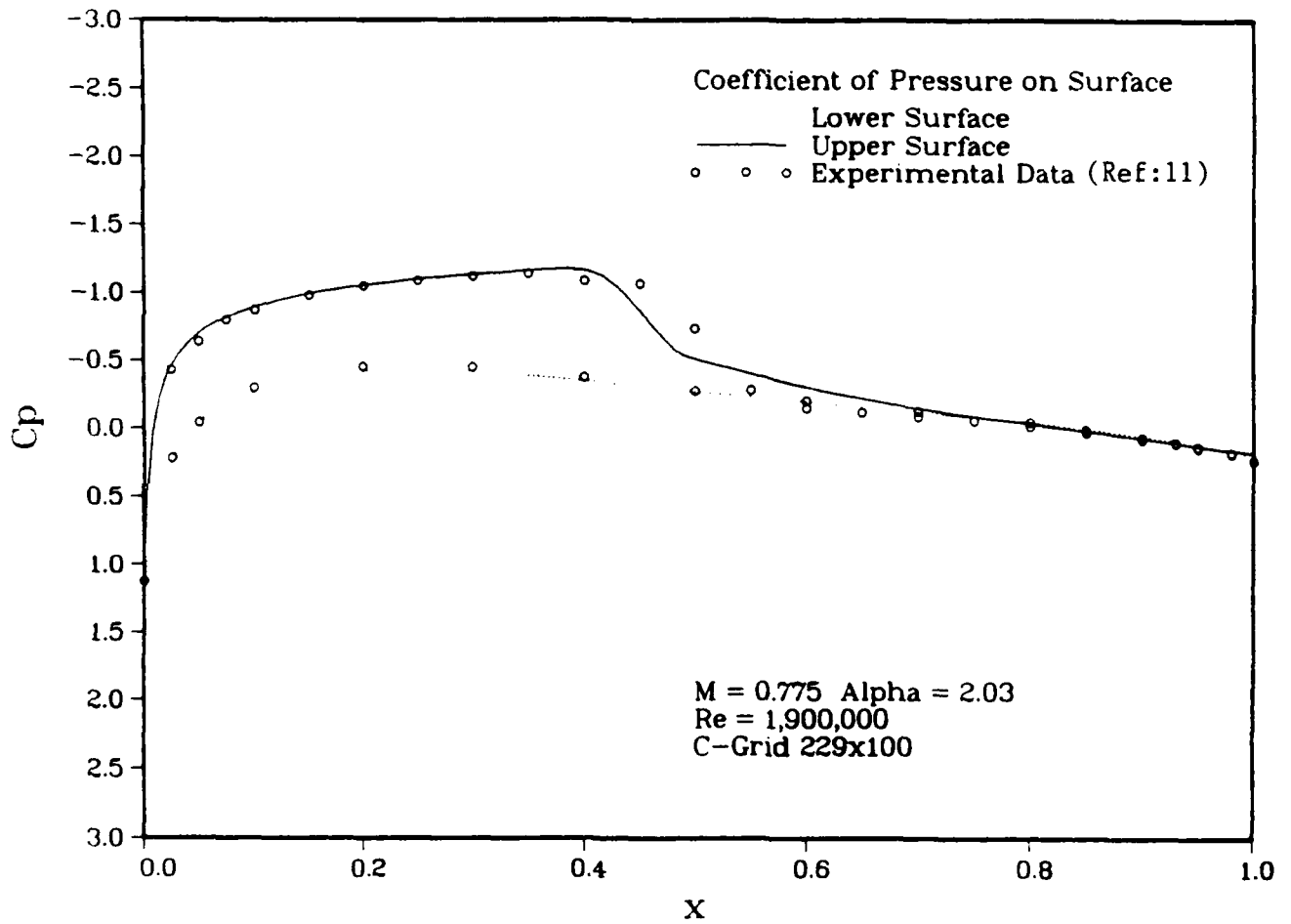


Figure 22. C-grid 5: Transonic Pressure Coefficient Profile

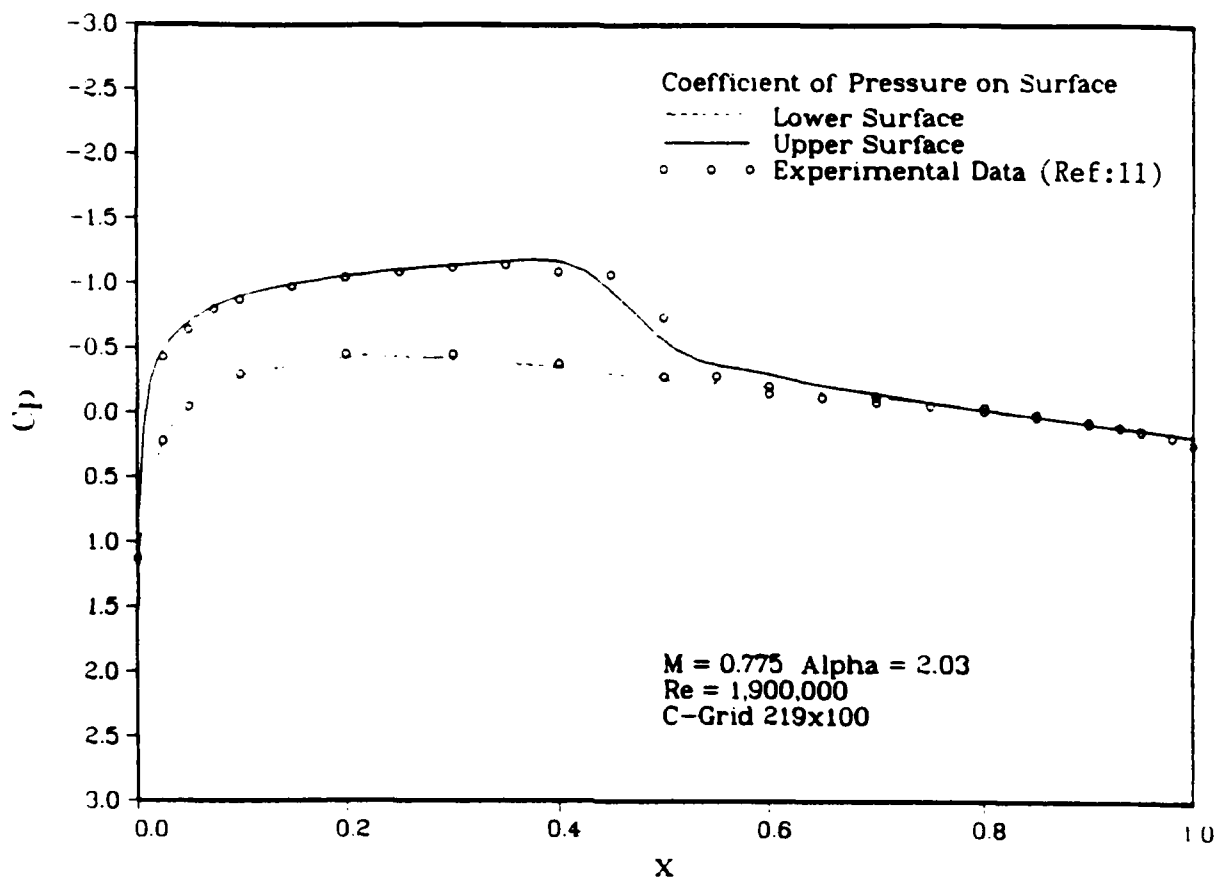
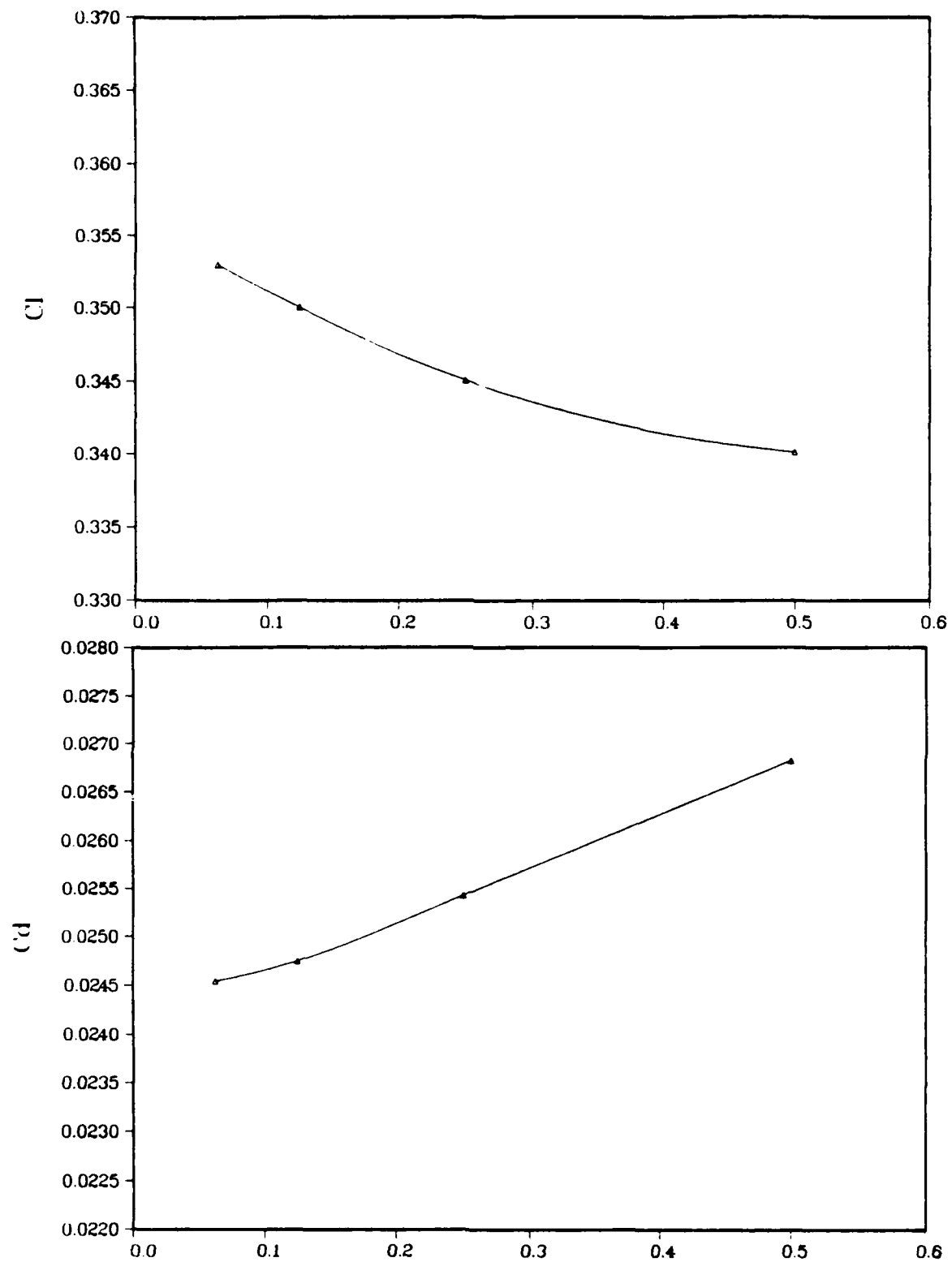


Figure 23. Transonic Pressure Coefficient Profile, Reduced Damping



Second-Order Artificial Viscosity
Figure 24. C_l and C_d vs Artificial Viscosity

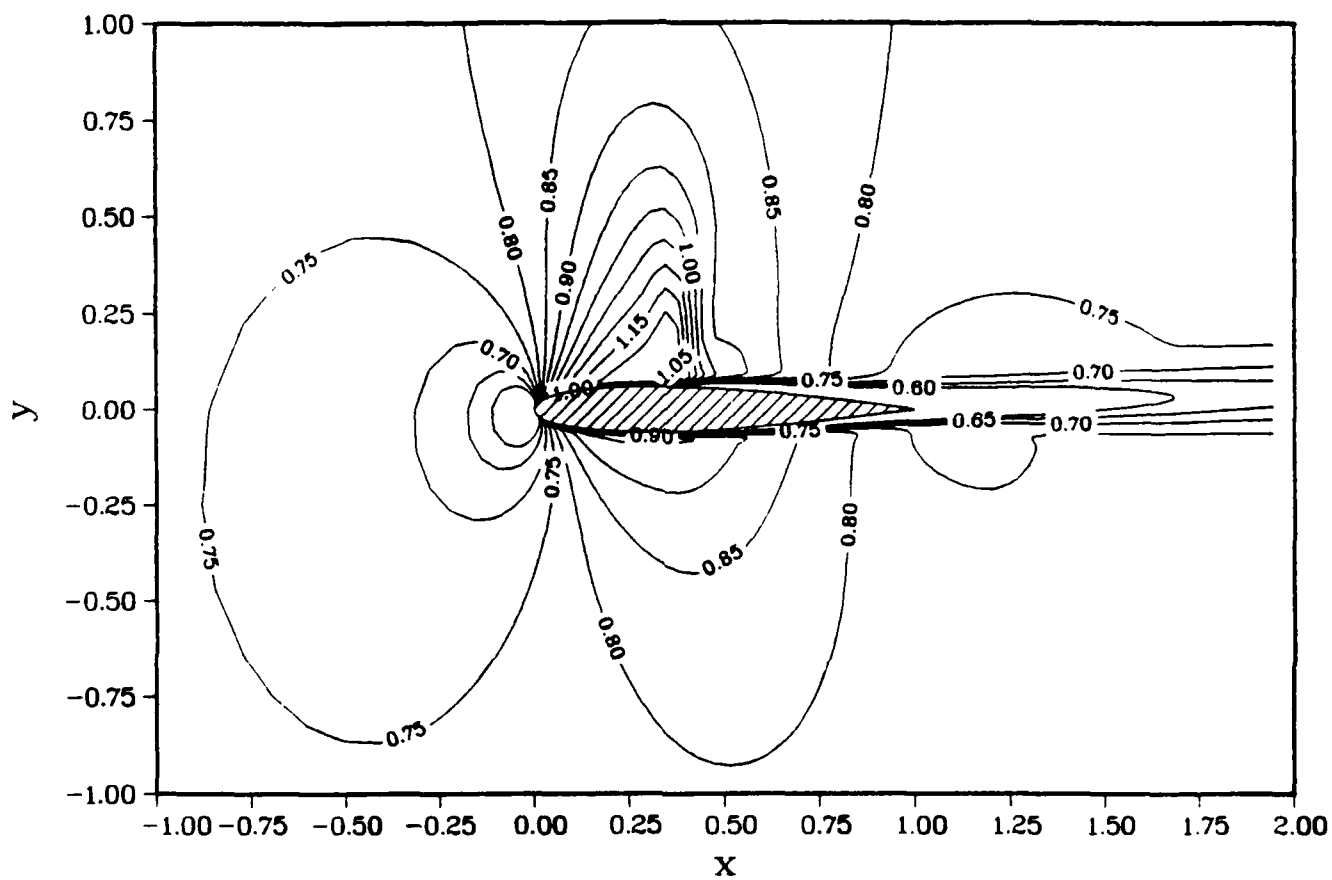


Figure 25. C-grid 1: Mach Contours $M = 0.775, \alpha = 2.03$

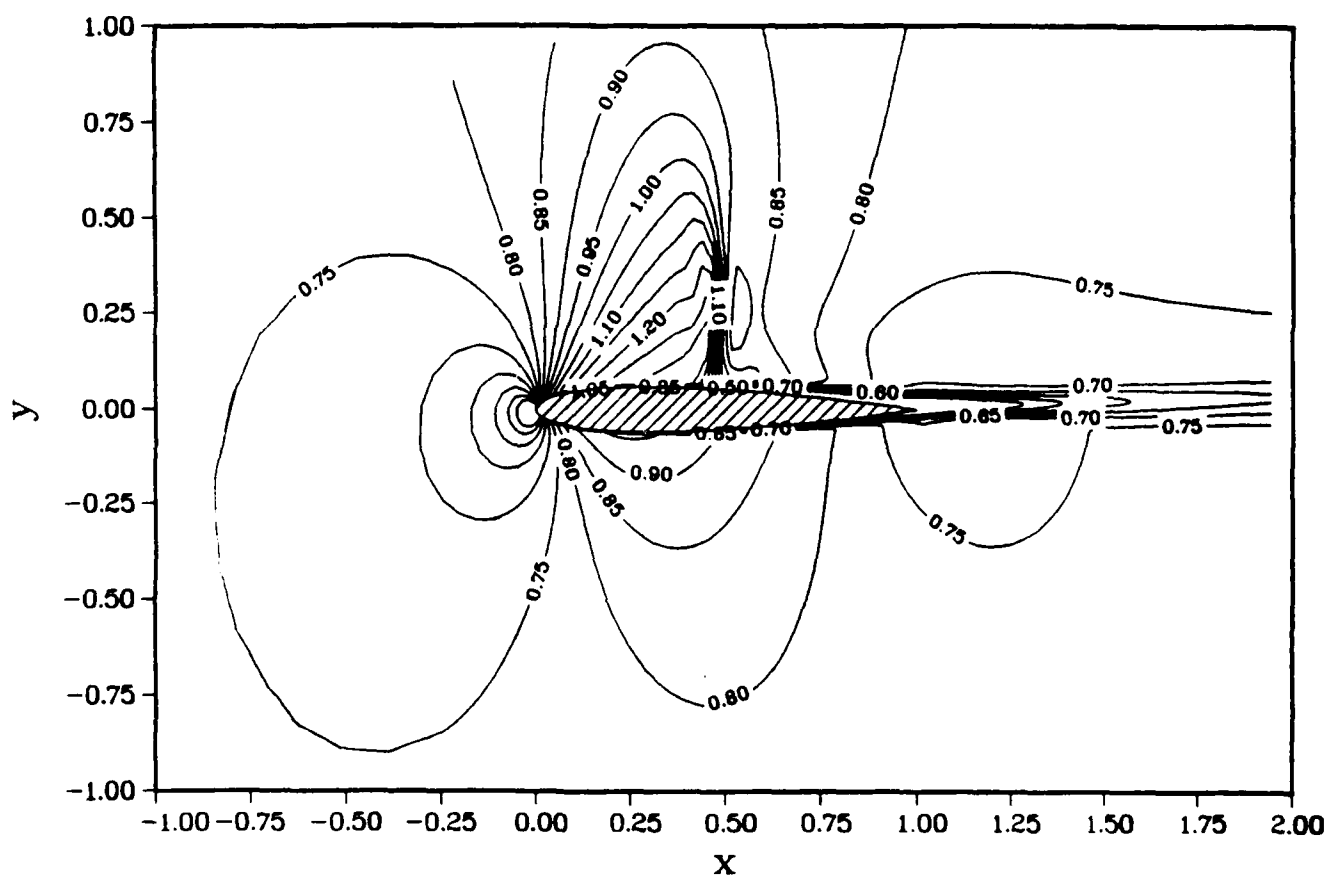


Figure 26. C-grid 4: Mach Contours $M = 0.775, \alpha = 2.03$

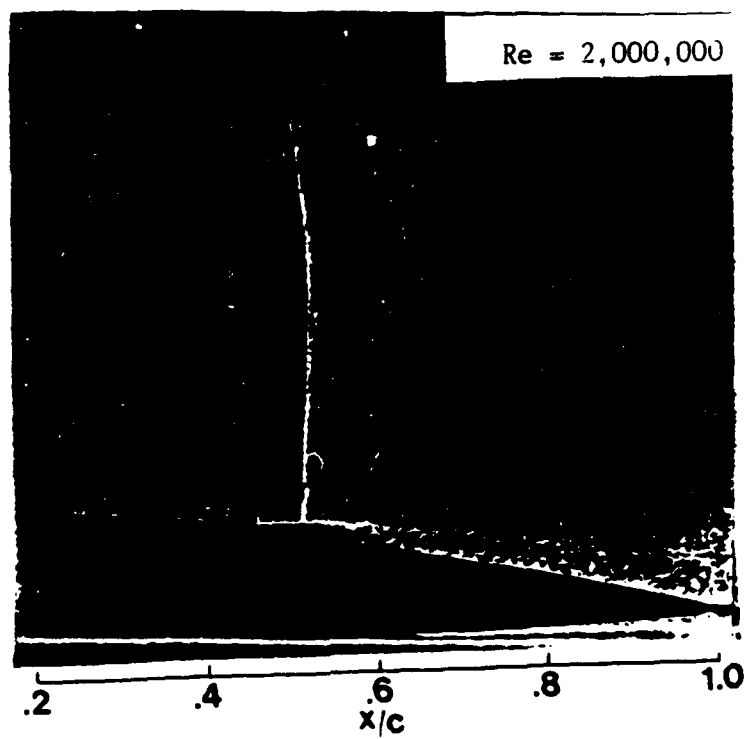


Figure 27. Experimental Location of Shock Wave, $M = 0.775$, $\alpha = 2.03$
(Ref:11)

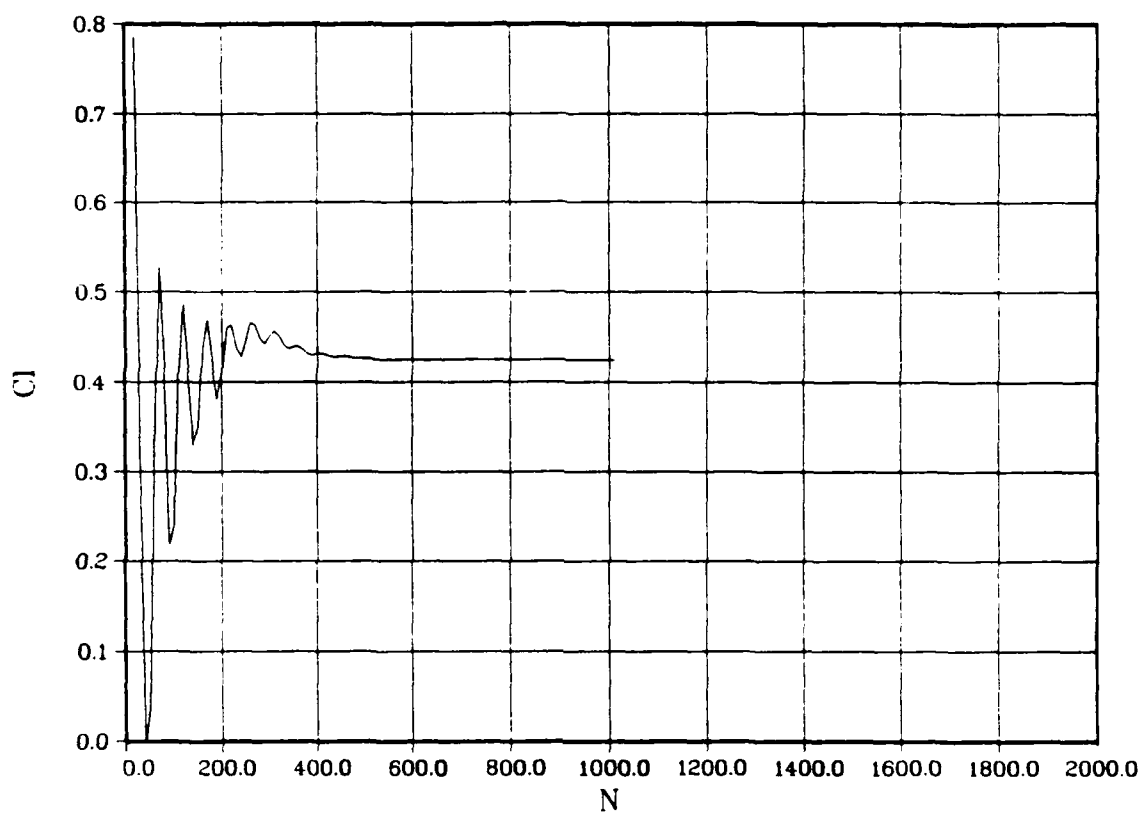


Figure 28. C-grid 2: Lift Coefficient vs Iterations, $M = 0.3, \alpha = 4.04$

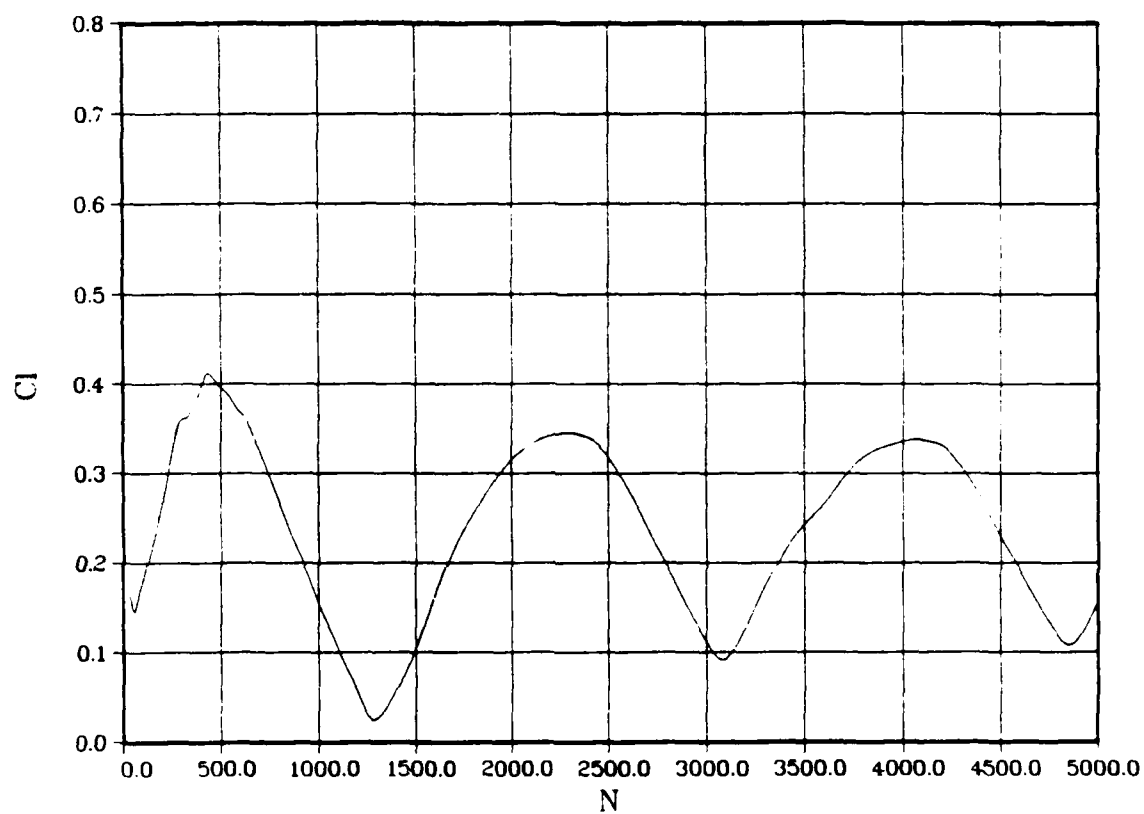


Figure 29. C-grid 2: Lift Coefficient vs Iterations, $M = 0.775$, $\alpha = 2.03$

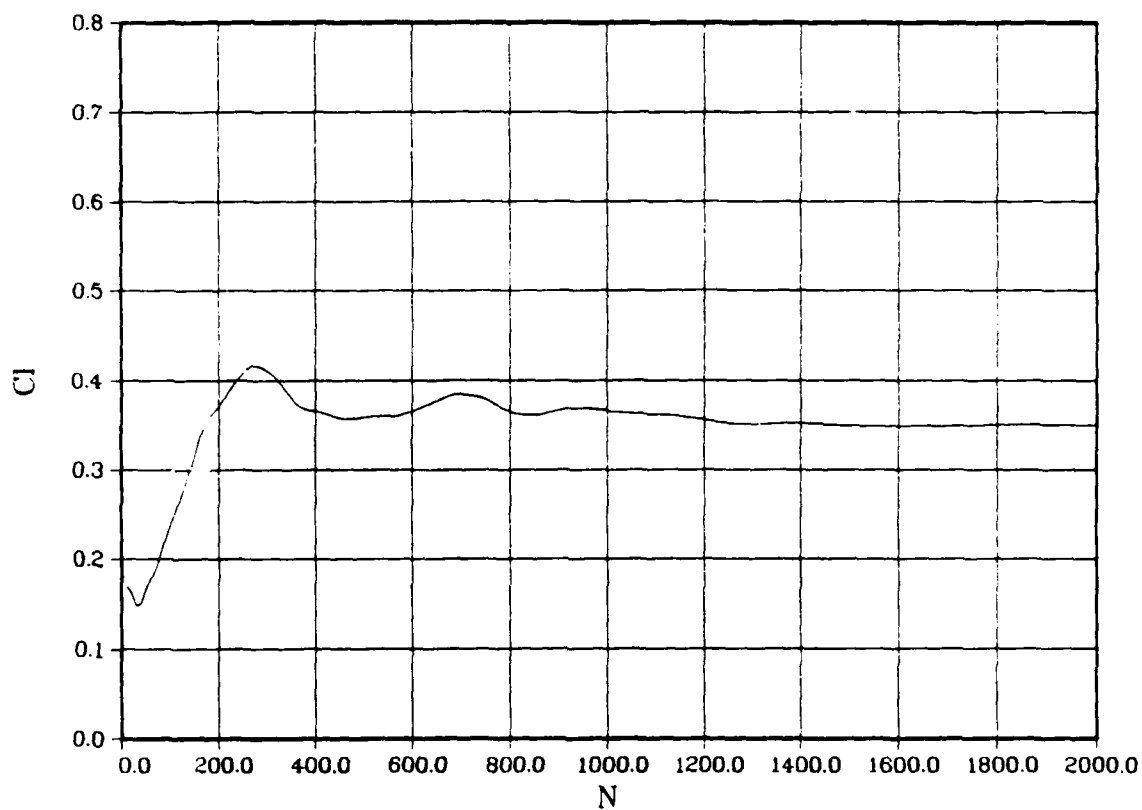


Figure 30. C-grid 4: Lift Coefficient vs Iterations, $M = 0.775$, $\alpha = 2.03$

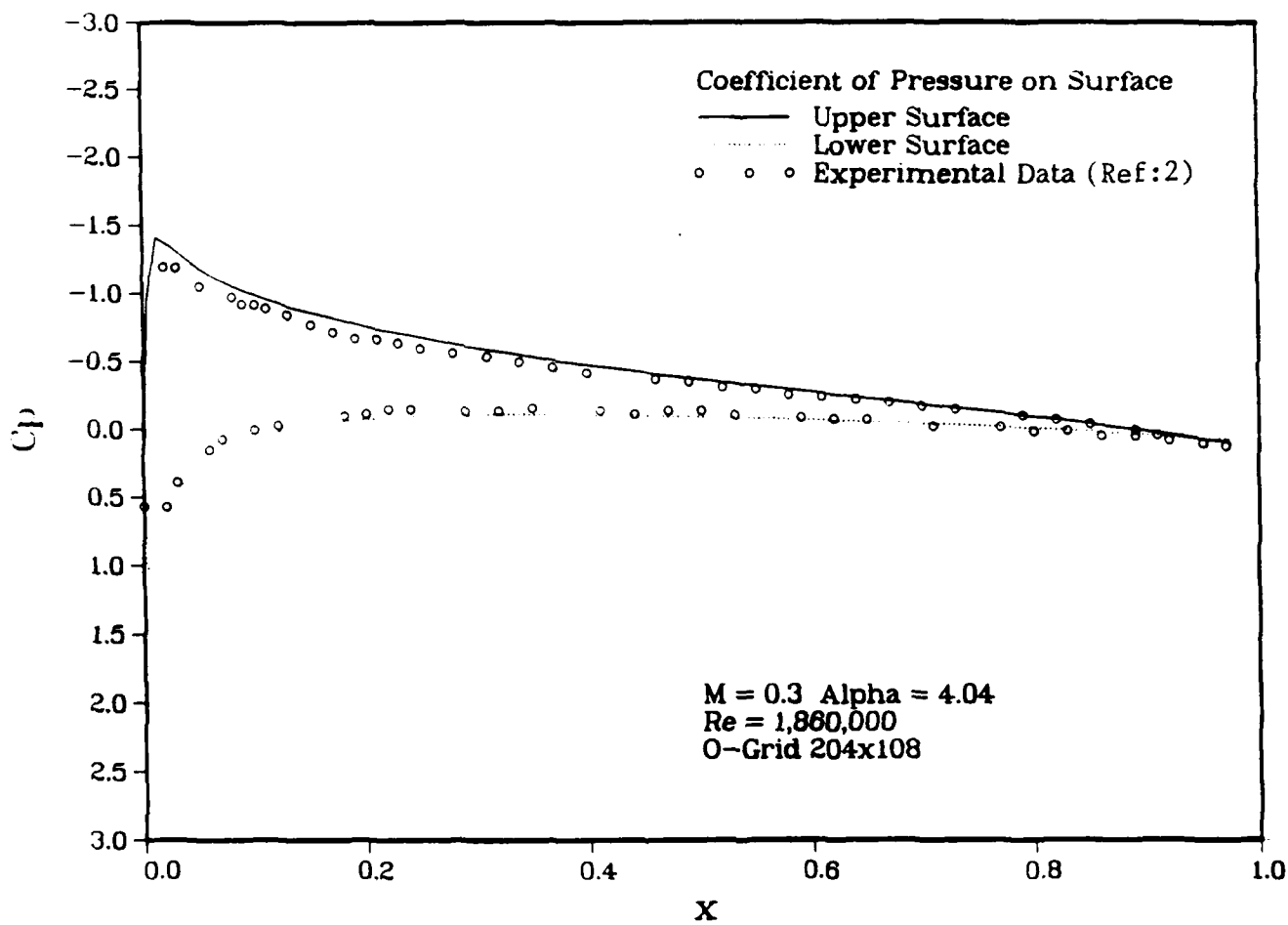


Figure 31. O-grid 1: Subsonic Pressure Coefficient Profile

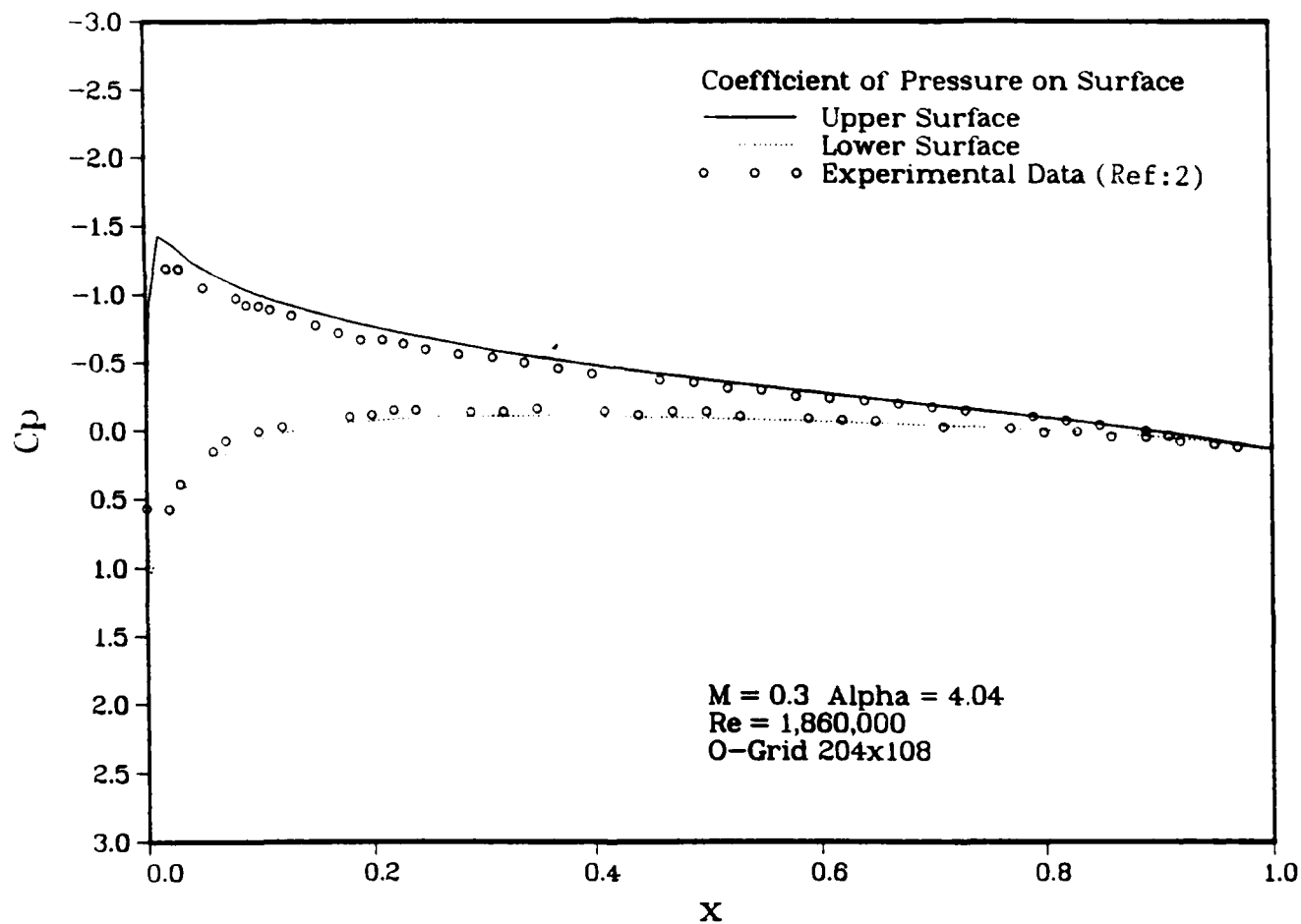


Figure 32. O-grid 3: Subsonic Pressure Coefficient Profile

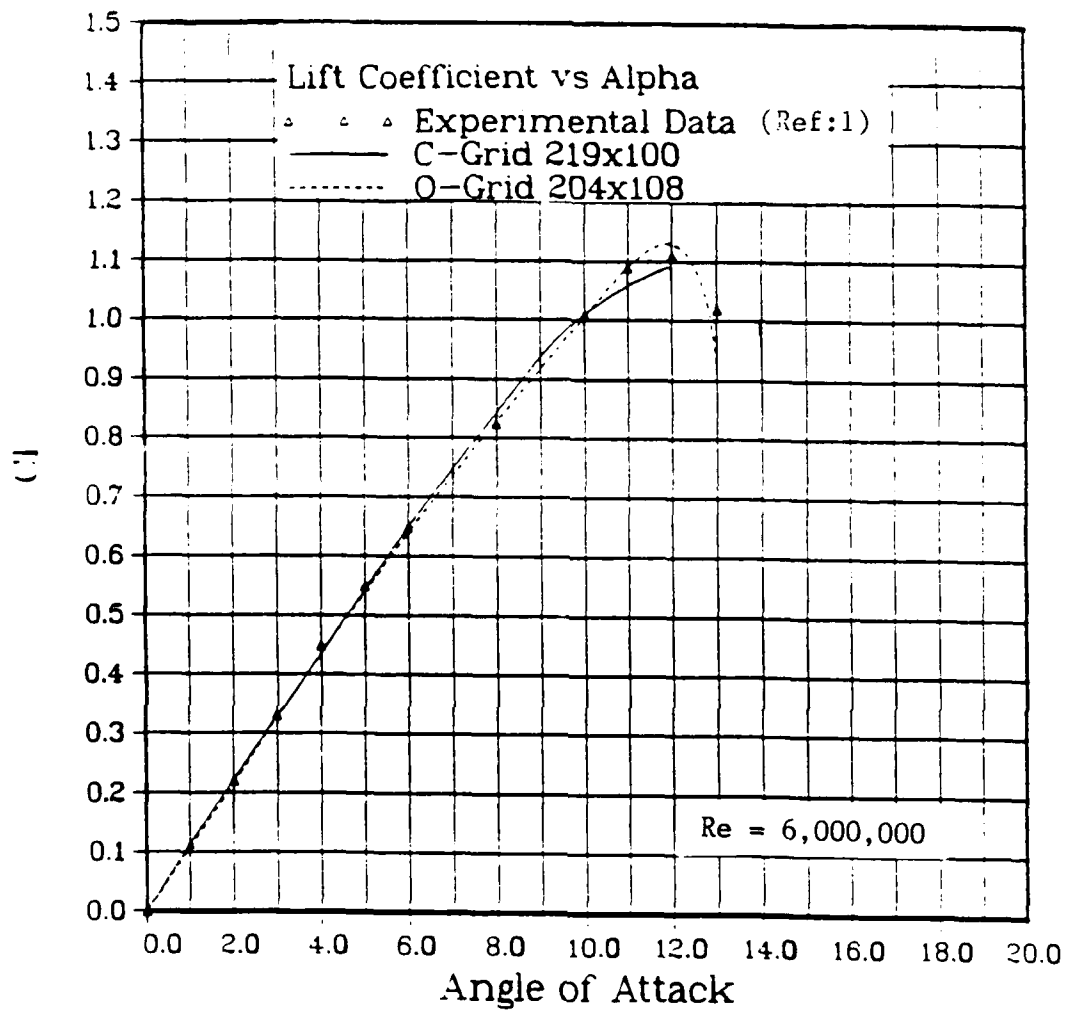


Figure 33. C-grid 4, O-grid 3: Lift Coefficient vs Angle of Attack

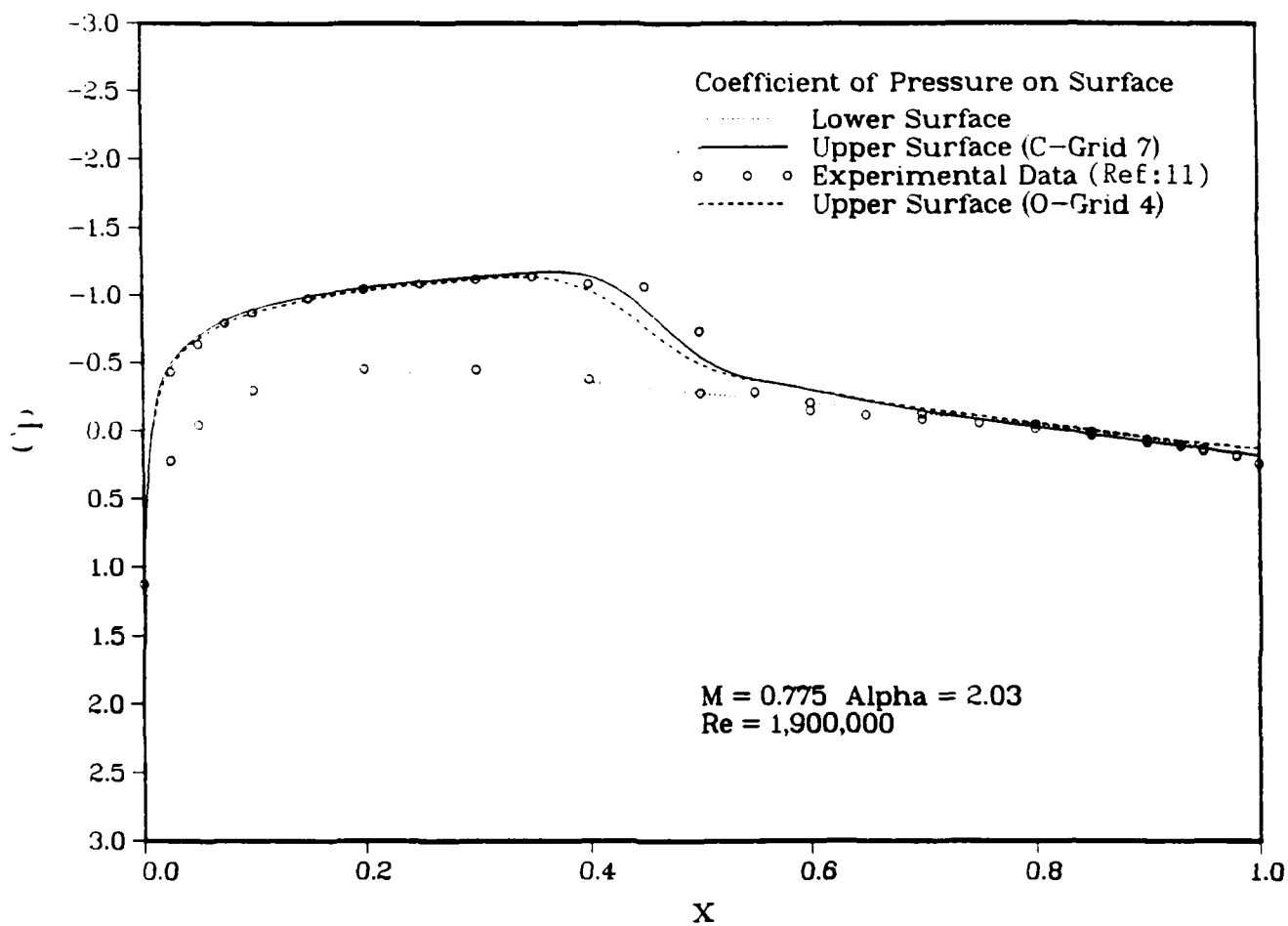


Figure 34. C-grid 4, O-grid 3: Transonic Pressure Coefficient Profiles

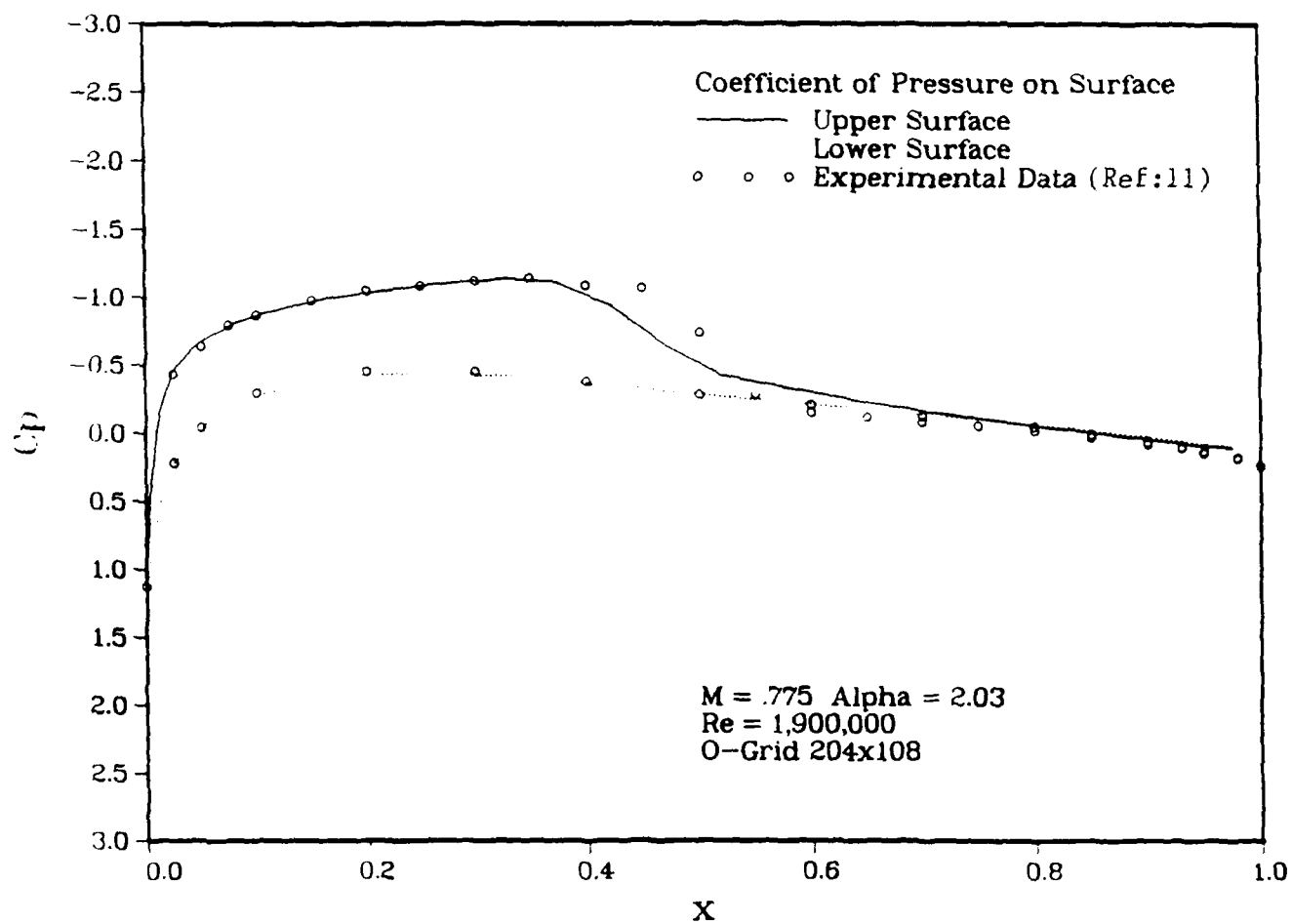


Figure 35. O-grid 2: Transonic Pressure Coefficient Profile

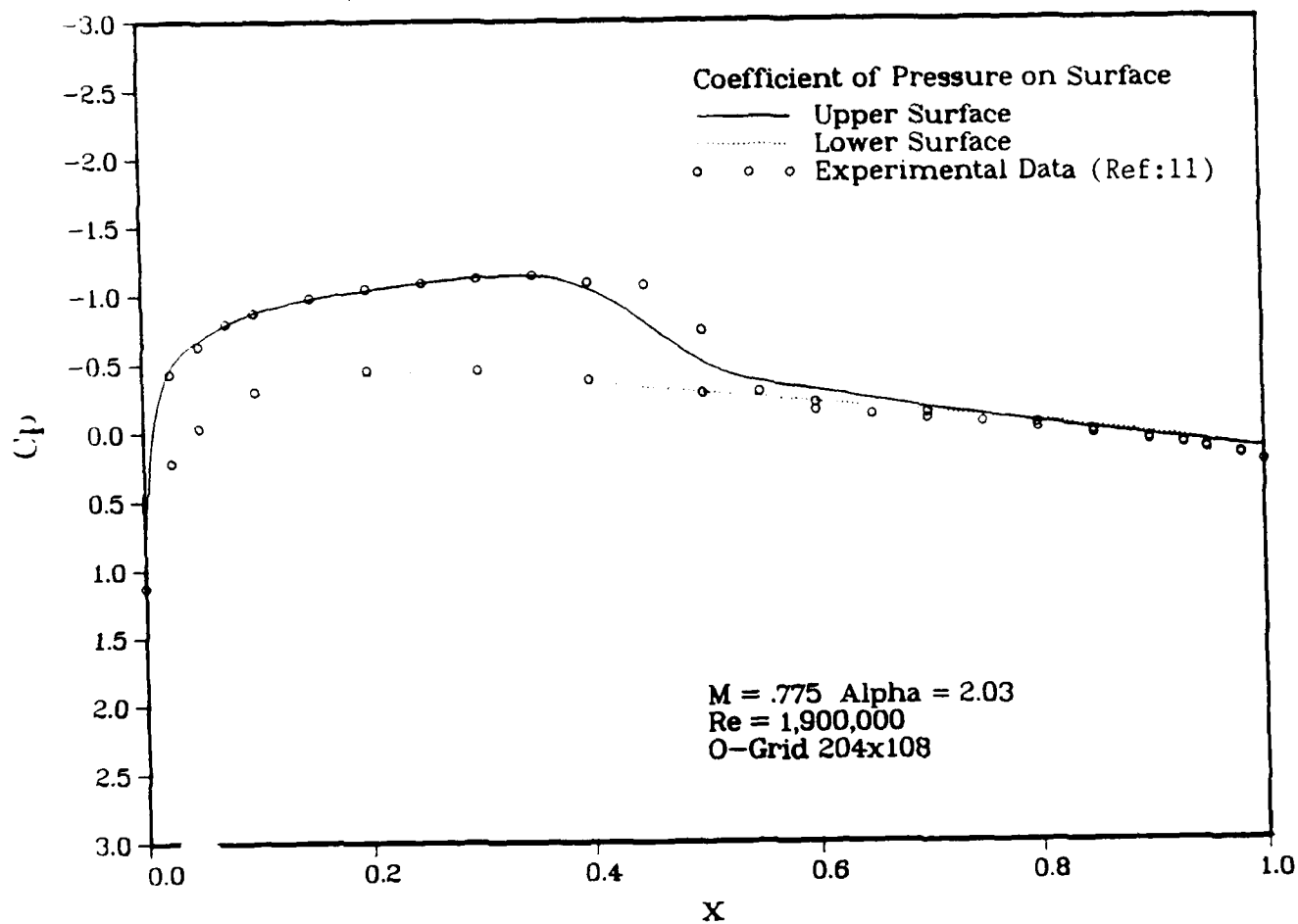


Figure 36. O-grid 4: Transonic Pressure Coefficient Profile

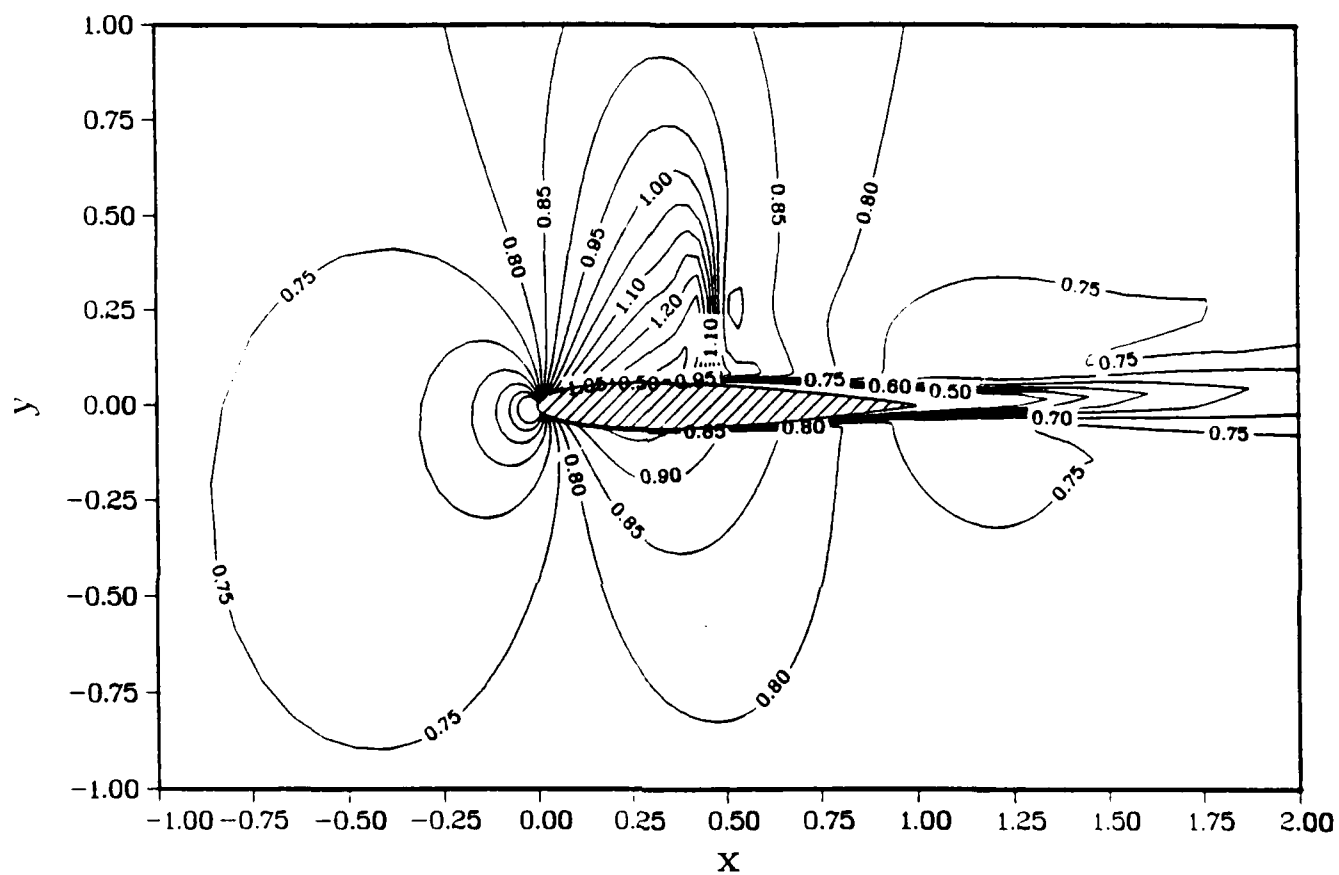


Figure 37. O-grid 3: Mach Contours, $M = 0.775$, $\alpha = 2.03$

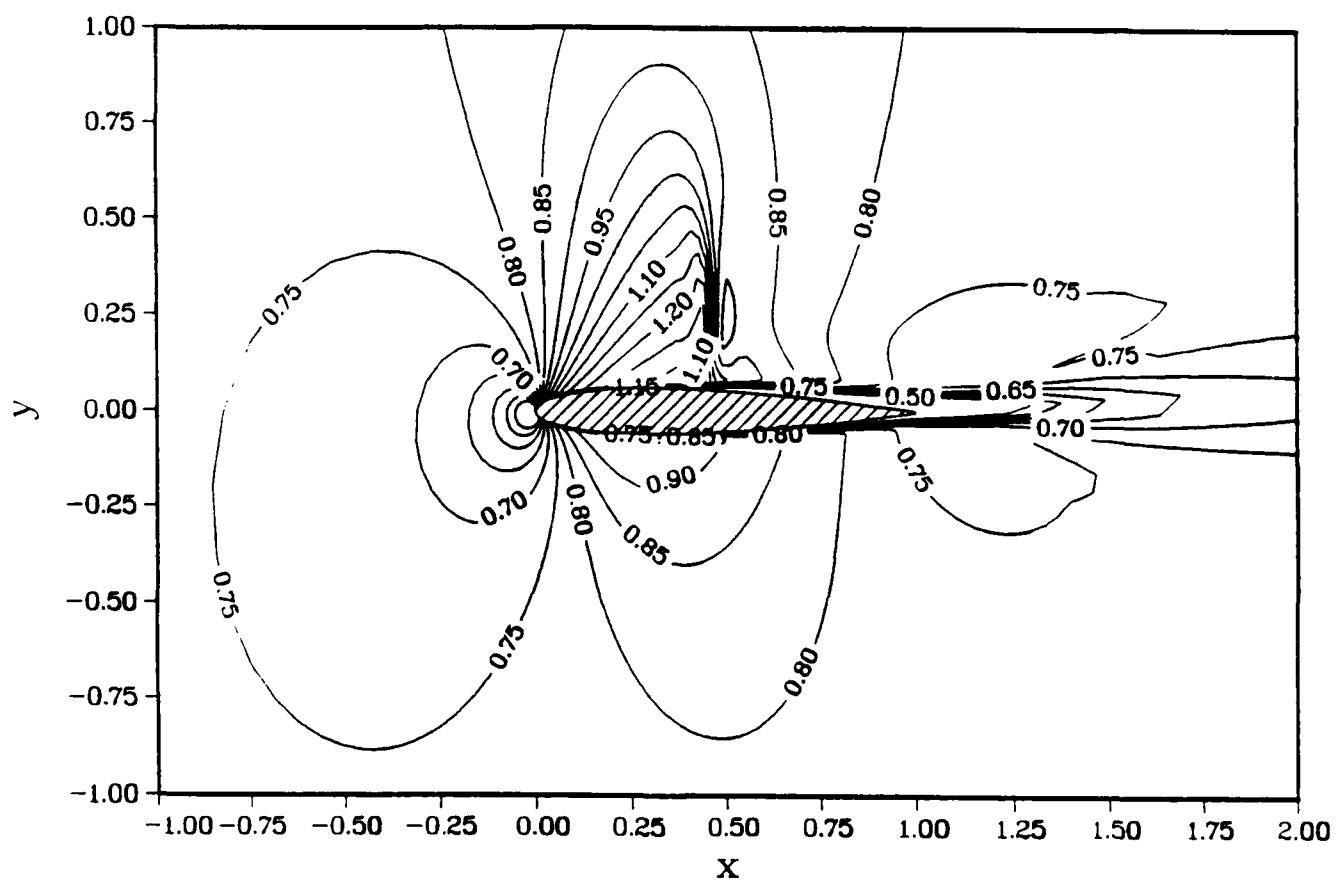


Figure 38. O-grid 4: Mach Contours, $M = 0.775$, $\alpha = 2.03$

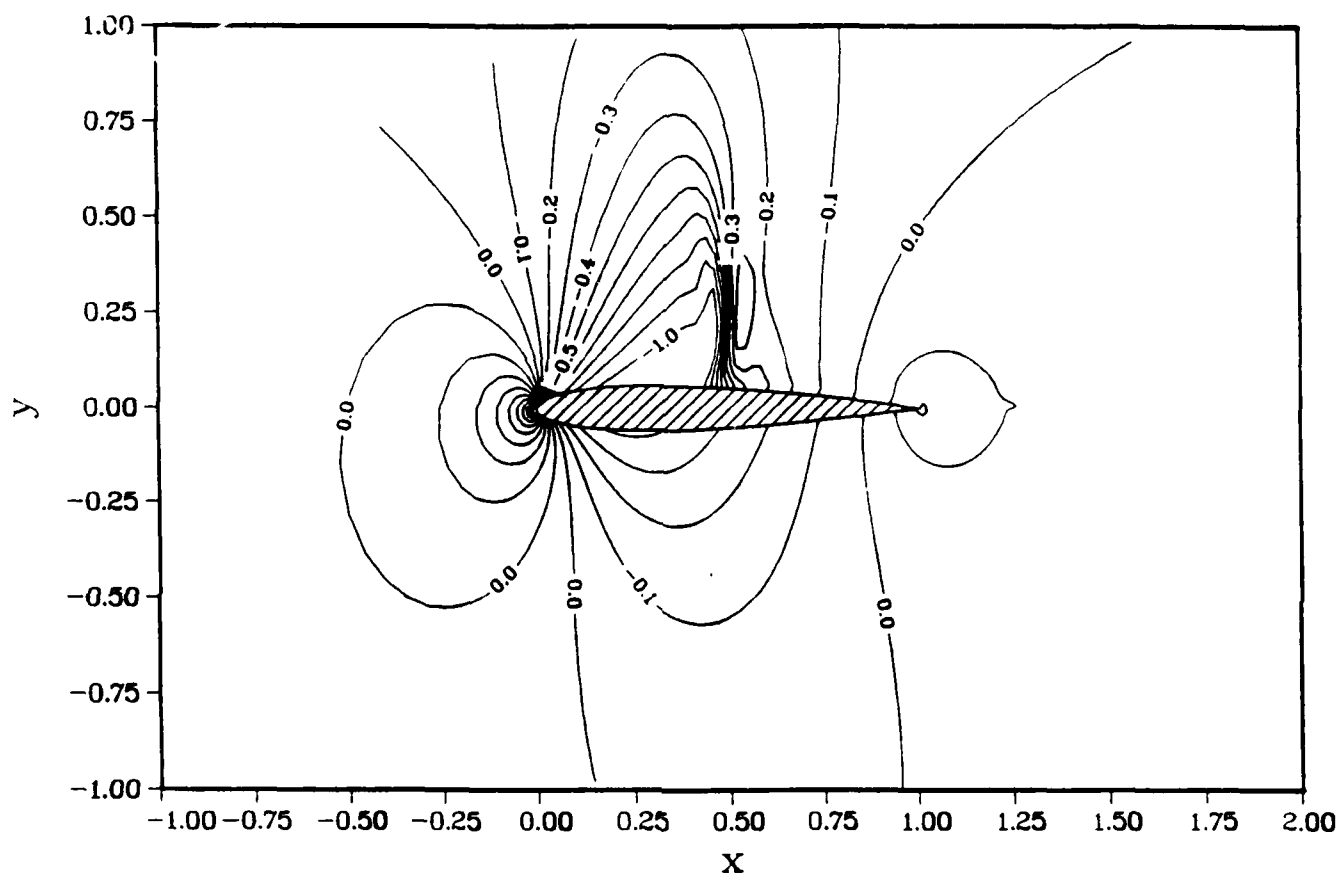


Figure 39. C-grid 4: Pressure Coefficient Contours, $M = 0.775$, $\alpha = 2.03$

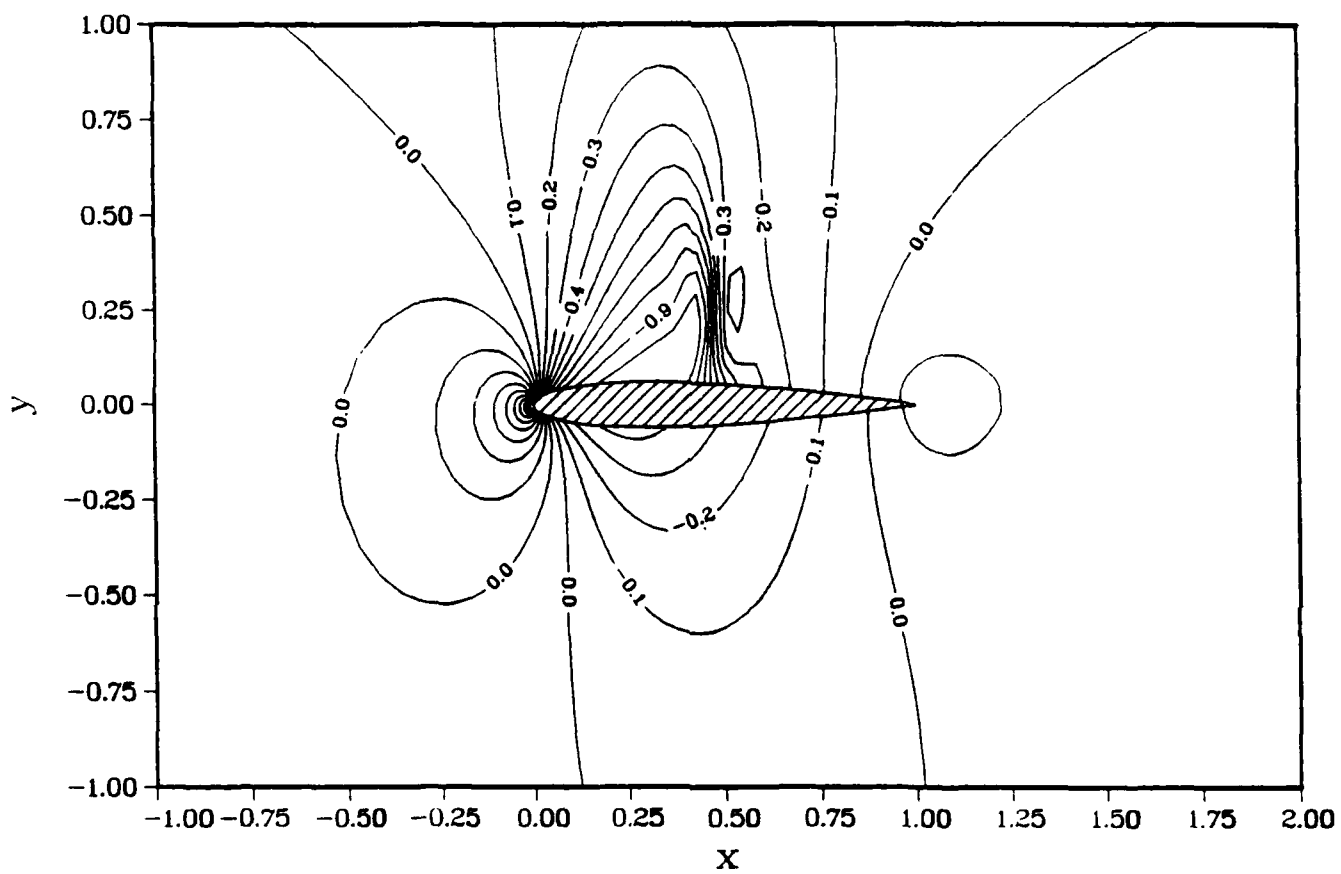


Figure 40. O-grid 3: Pressure Coefficient Contours, $M = 0.775$, $\alpha = 2.03$

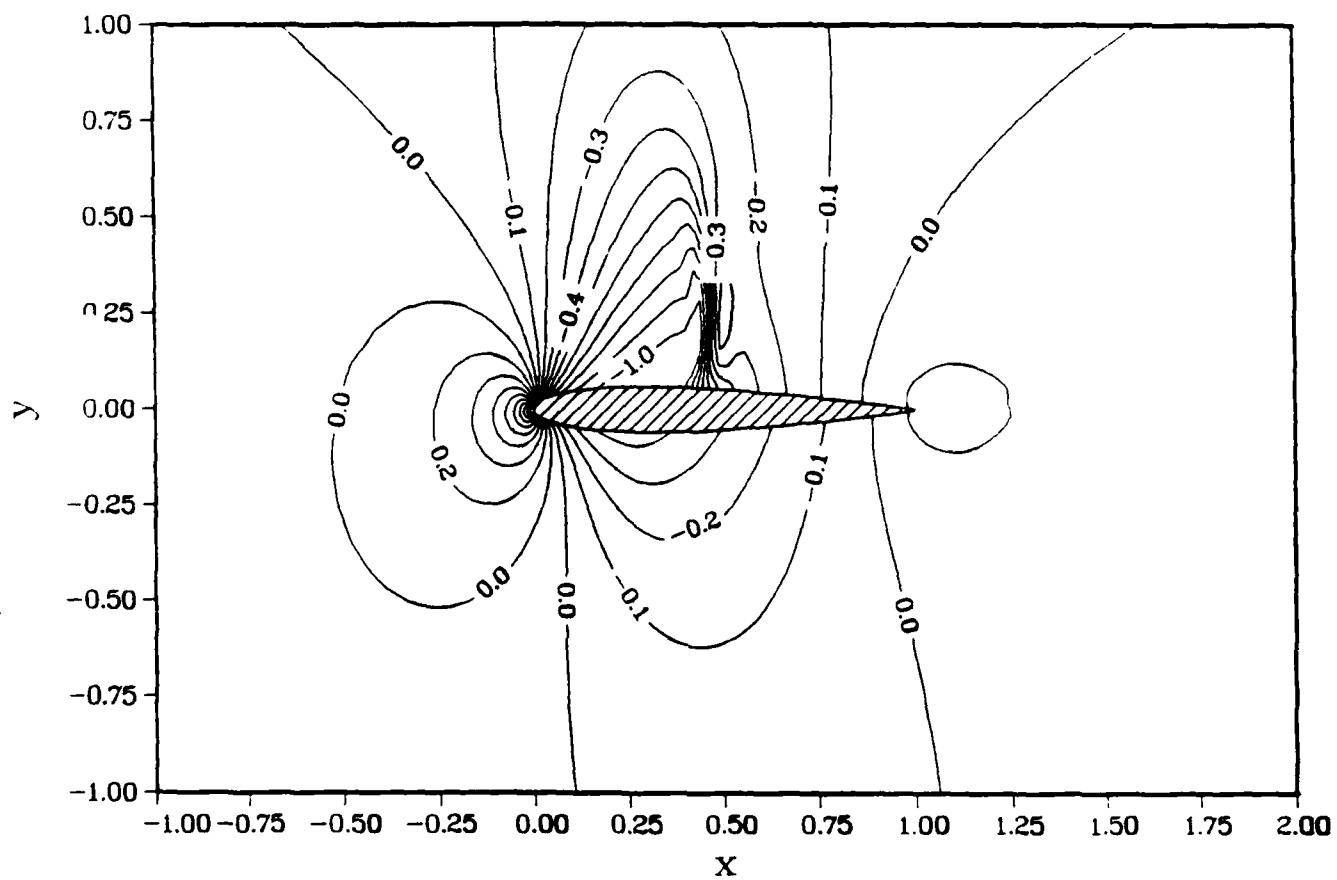


Figure 41. O-grid 4: Pressure Coefficient Contours, $M = 0.775, \alpha = 2.03$

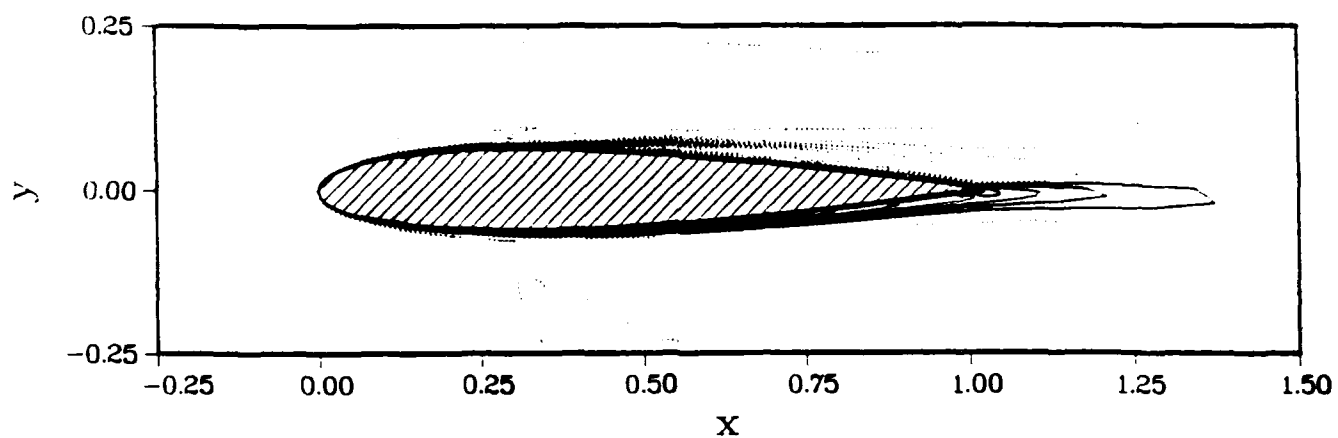


Figure 42. O-grid 3: Vorticity Contours $M = 0.775, \alpha = 2.03$

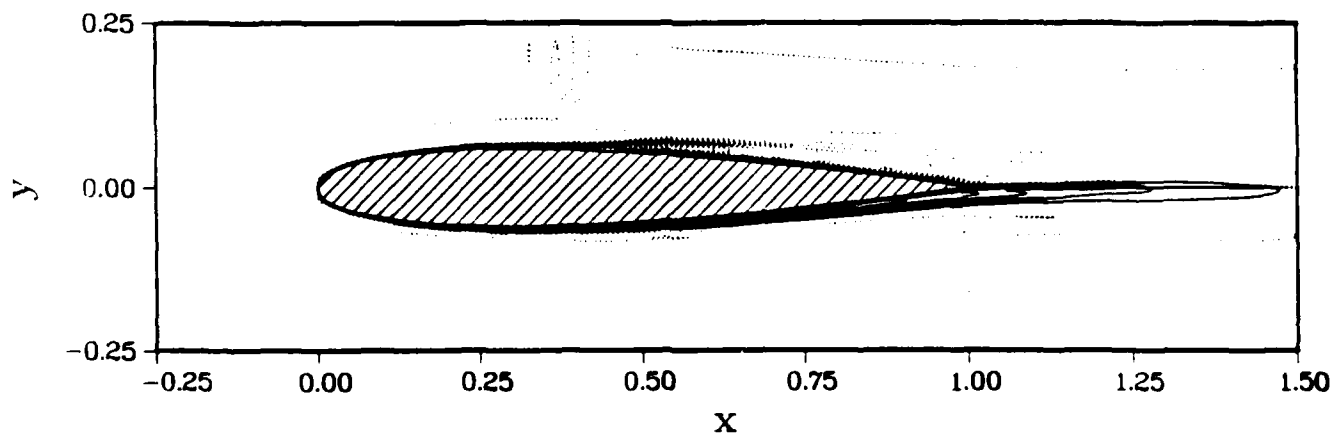


Figure 43. C-grid 4: Vorticity Contours, $M = 0.775, \alpha = 2.03$

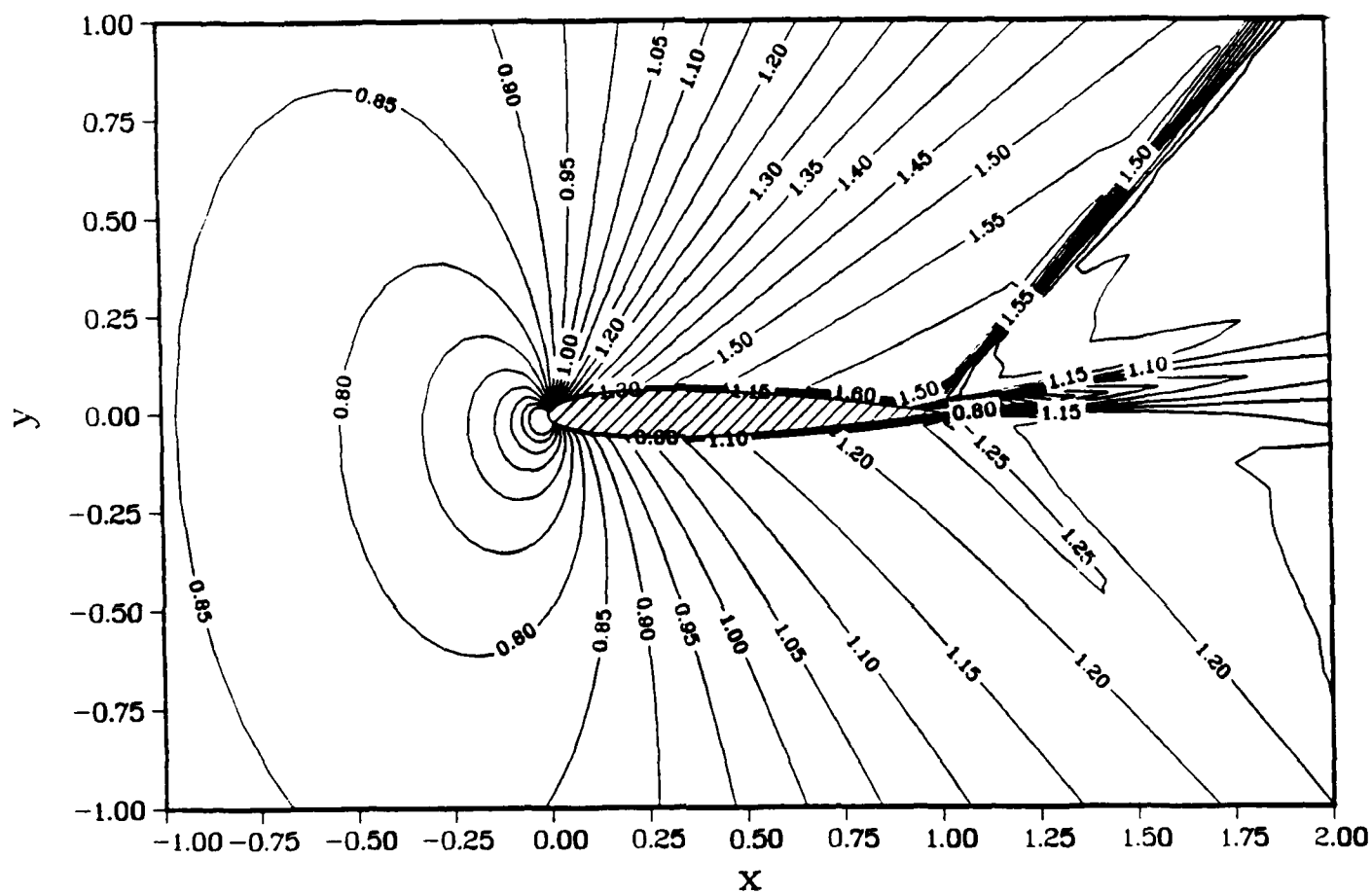


Figure 44. O-grid 3: Mach Contours, $M = 1.1$, $\alpha = 6.00$

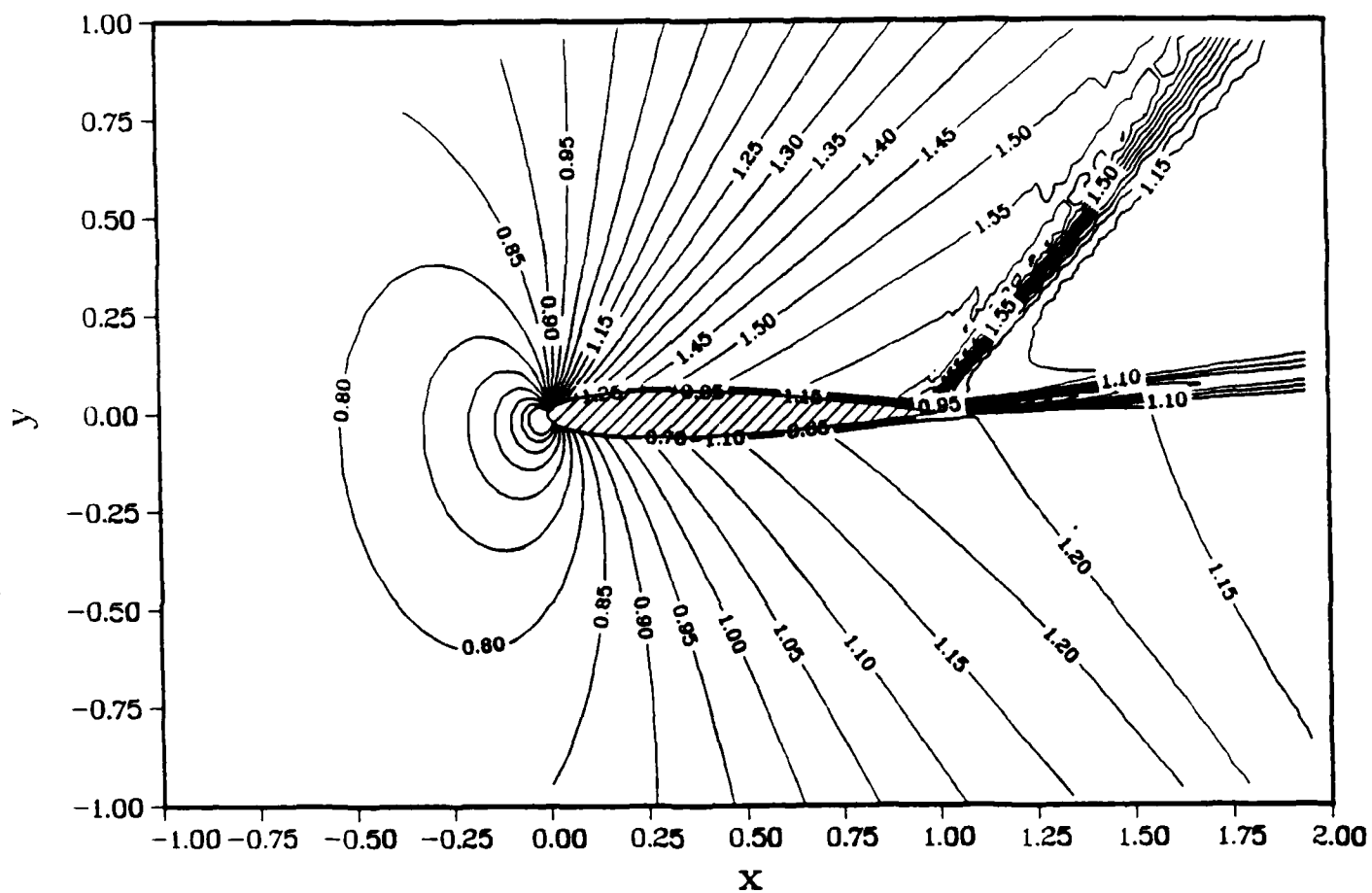


Figure 45. C-grid 4: Mach Contours, $M = 1.1$, $\alpha = 6.00$

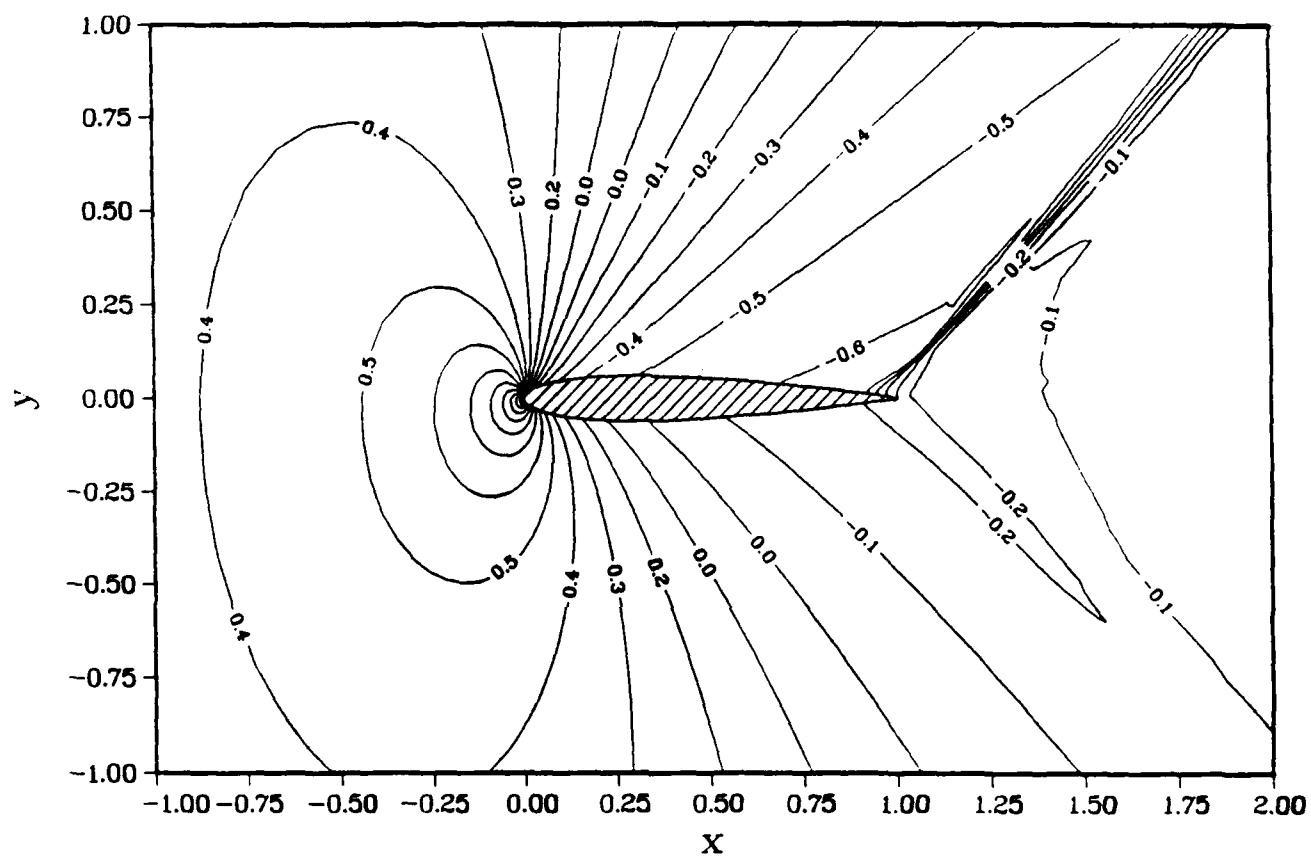


Figure 46. O-grid 3: Pressure Coefficient Contours, $M = 1.1$, $\alpha = 6.00$

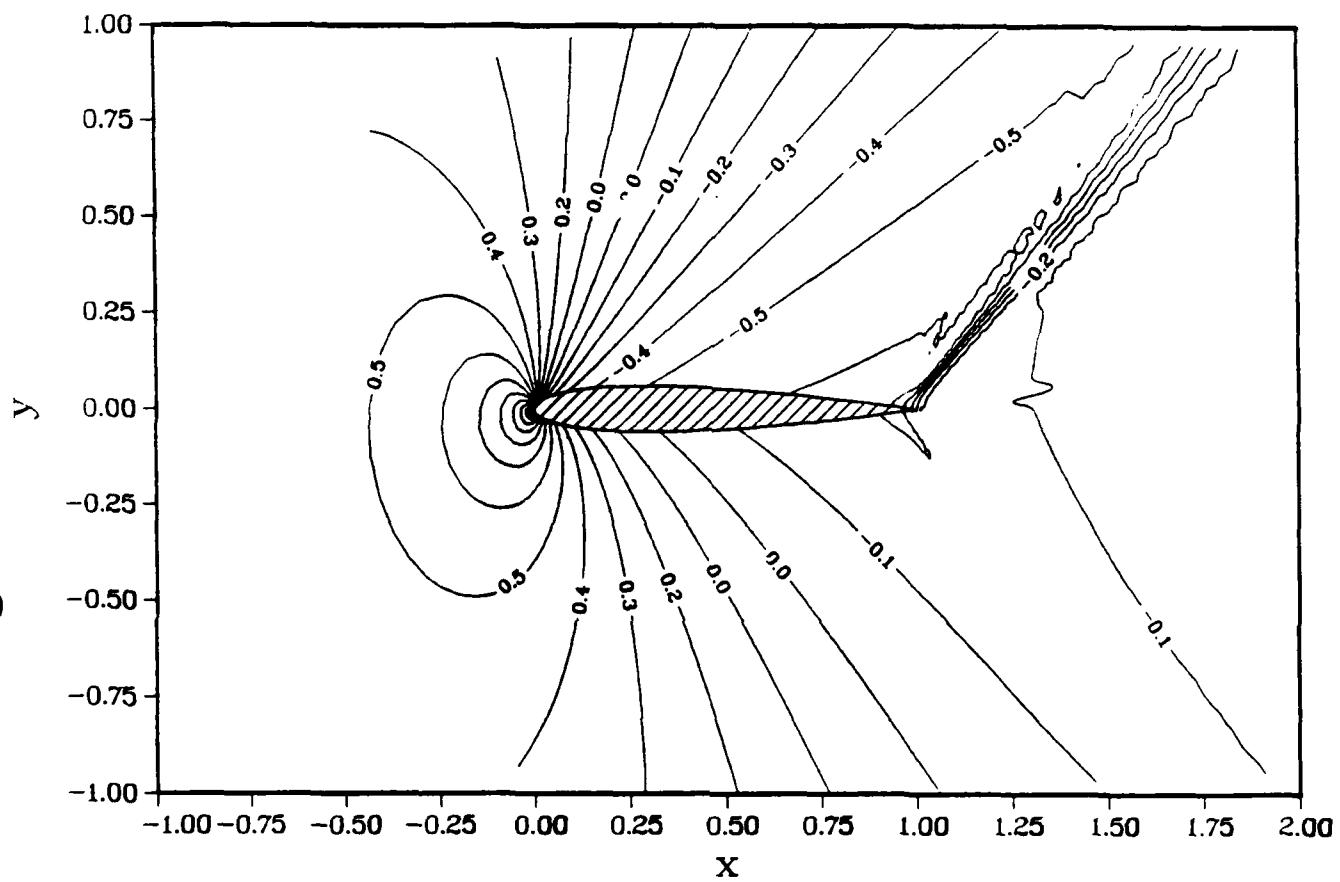


Figure 47. C-grid 4: Pressure Coefficient Contours, $M = 1.1$, $\alpha = 6.00$

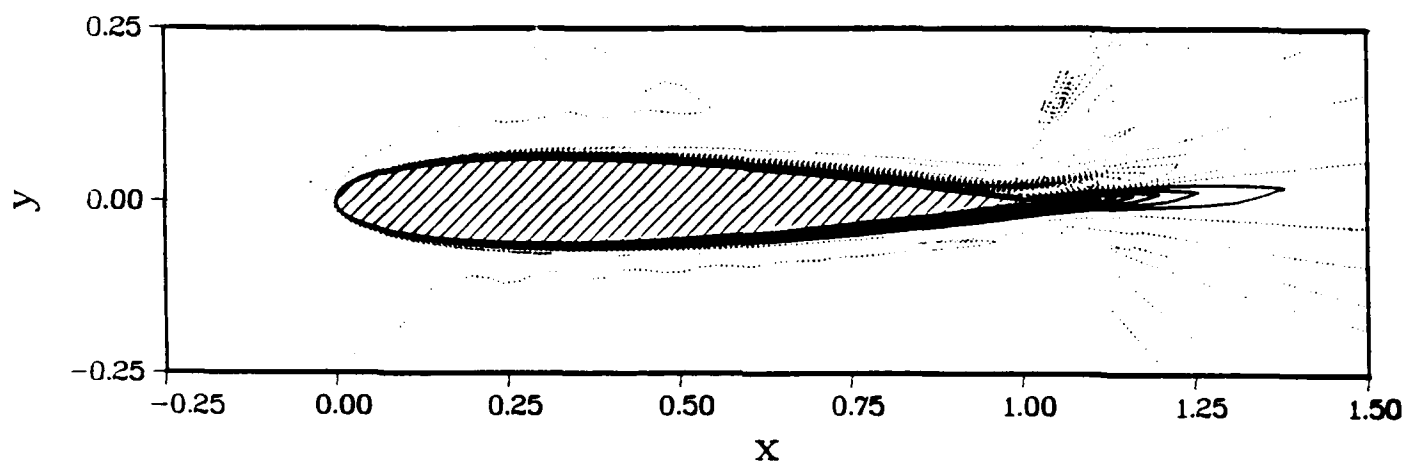


Figure 48. O-grid 3: Vorticity Contours, $M = 1.1$, $\alpha = 6.00$

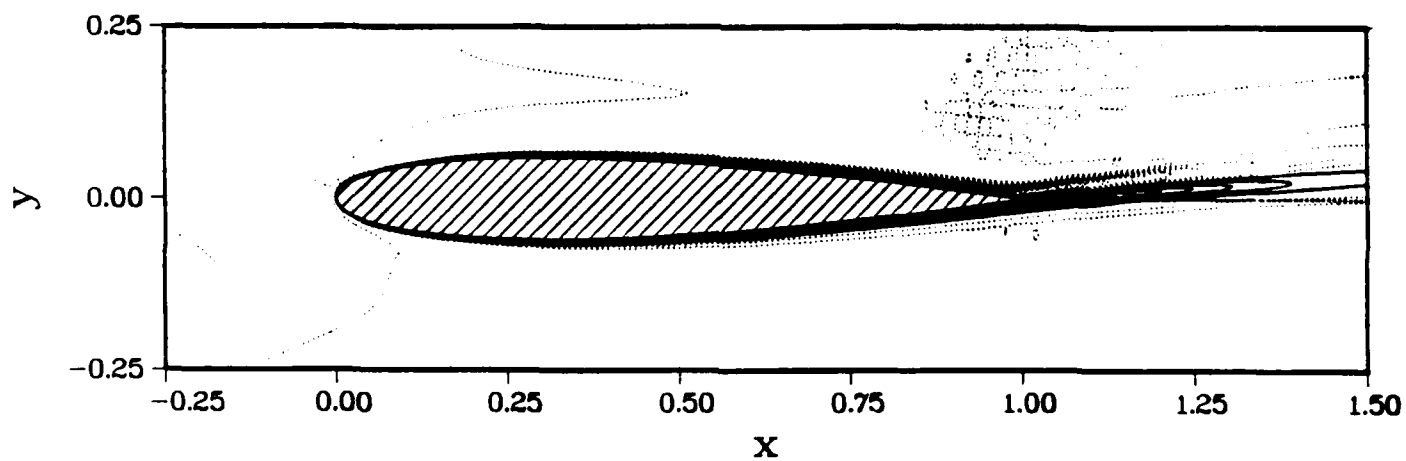


Figure 49. C-grid 4: Vorticity Contours $M = 1.1$, $\alpha = 6.00$

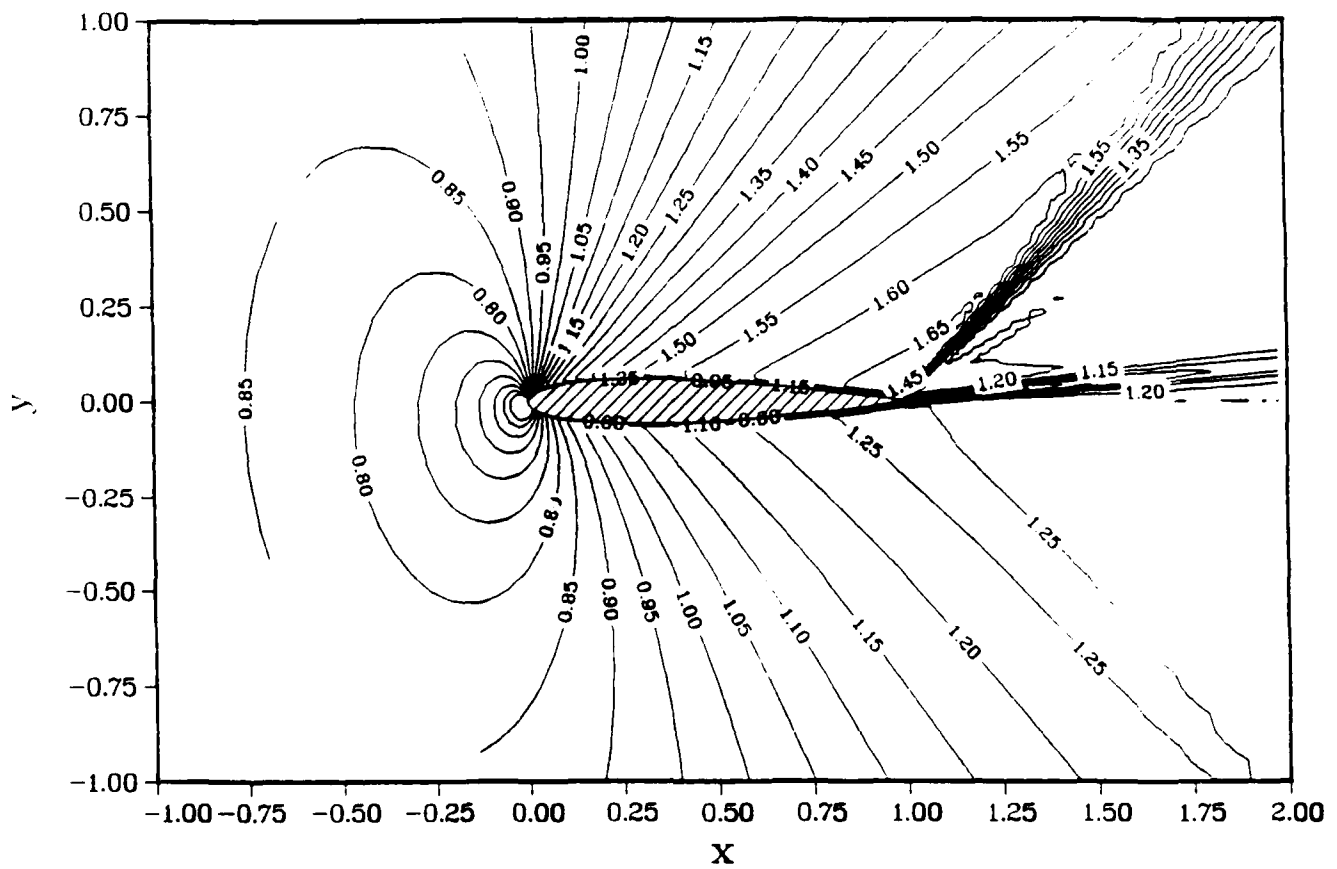


Figure 50. C-grid 8: Mach Contours, $M = 1.1$, $\alpha = 6.00$

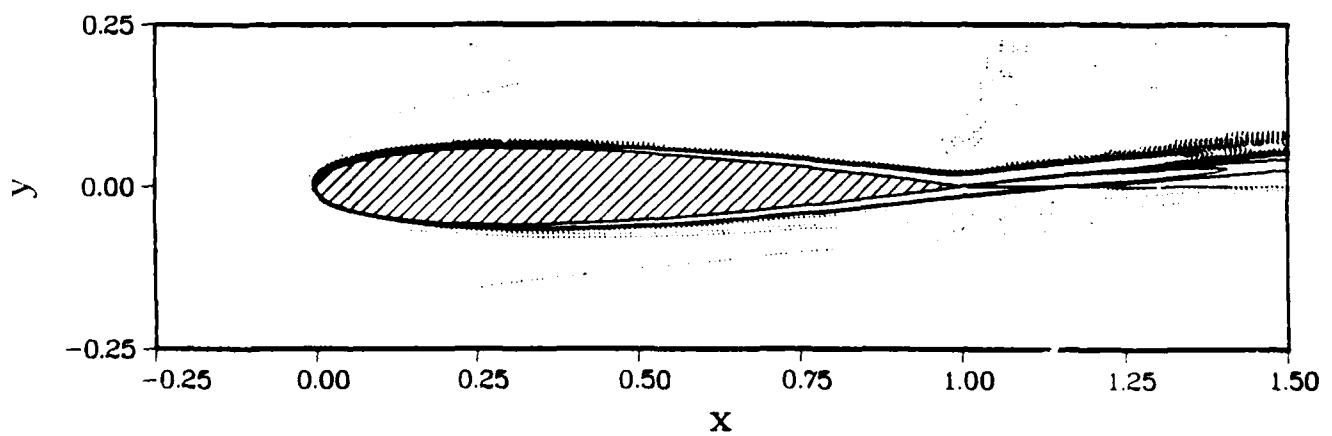


Figure 51. C-grid 8: Vorticity Contours, $M = 1.1$, $\alpha = 6.00$

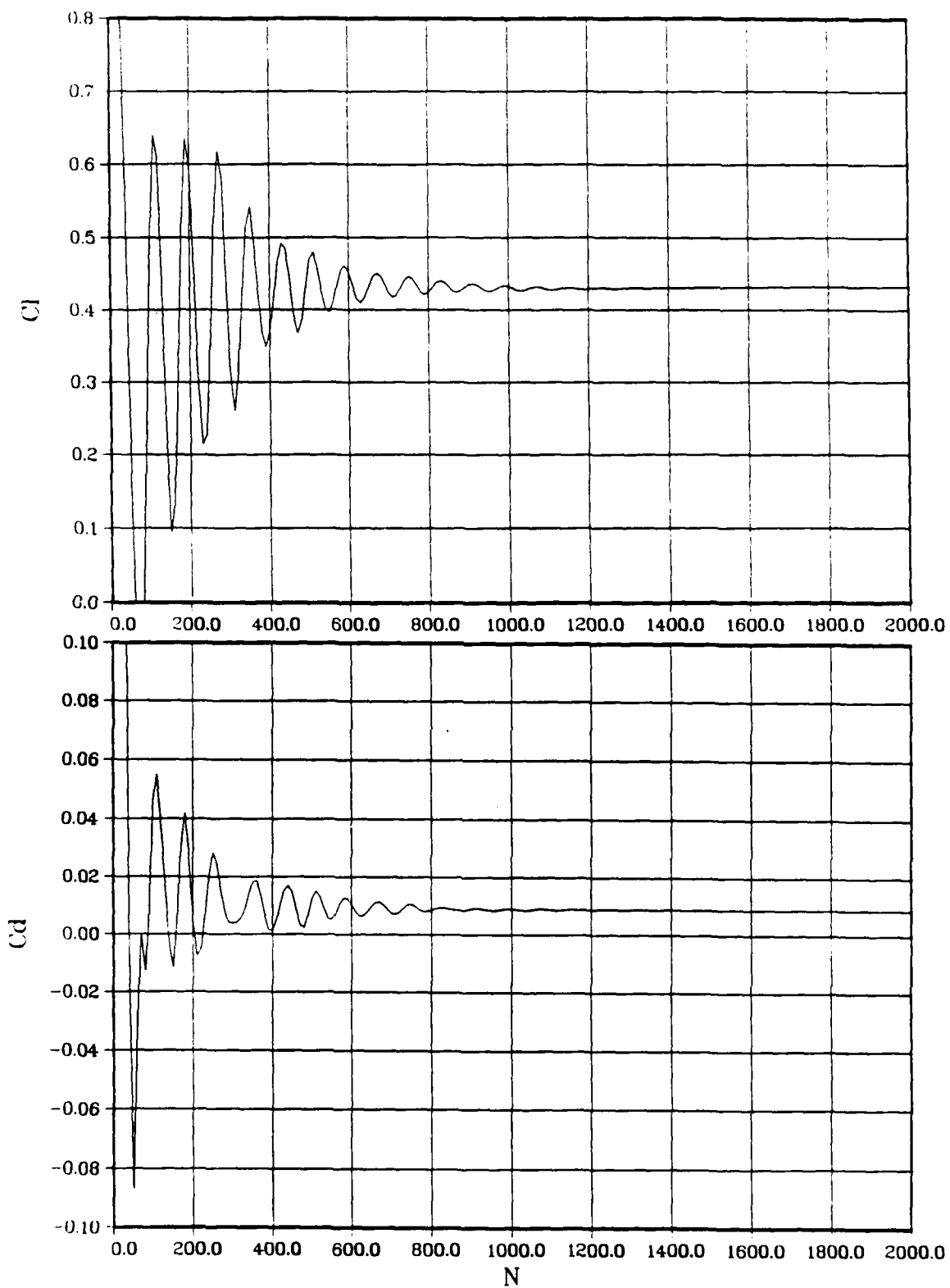


Figure 52. O-grid 3: Force Coefficients vs Iterations, $M = 0.3$, $\alpha = 4.04$

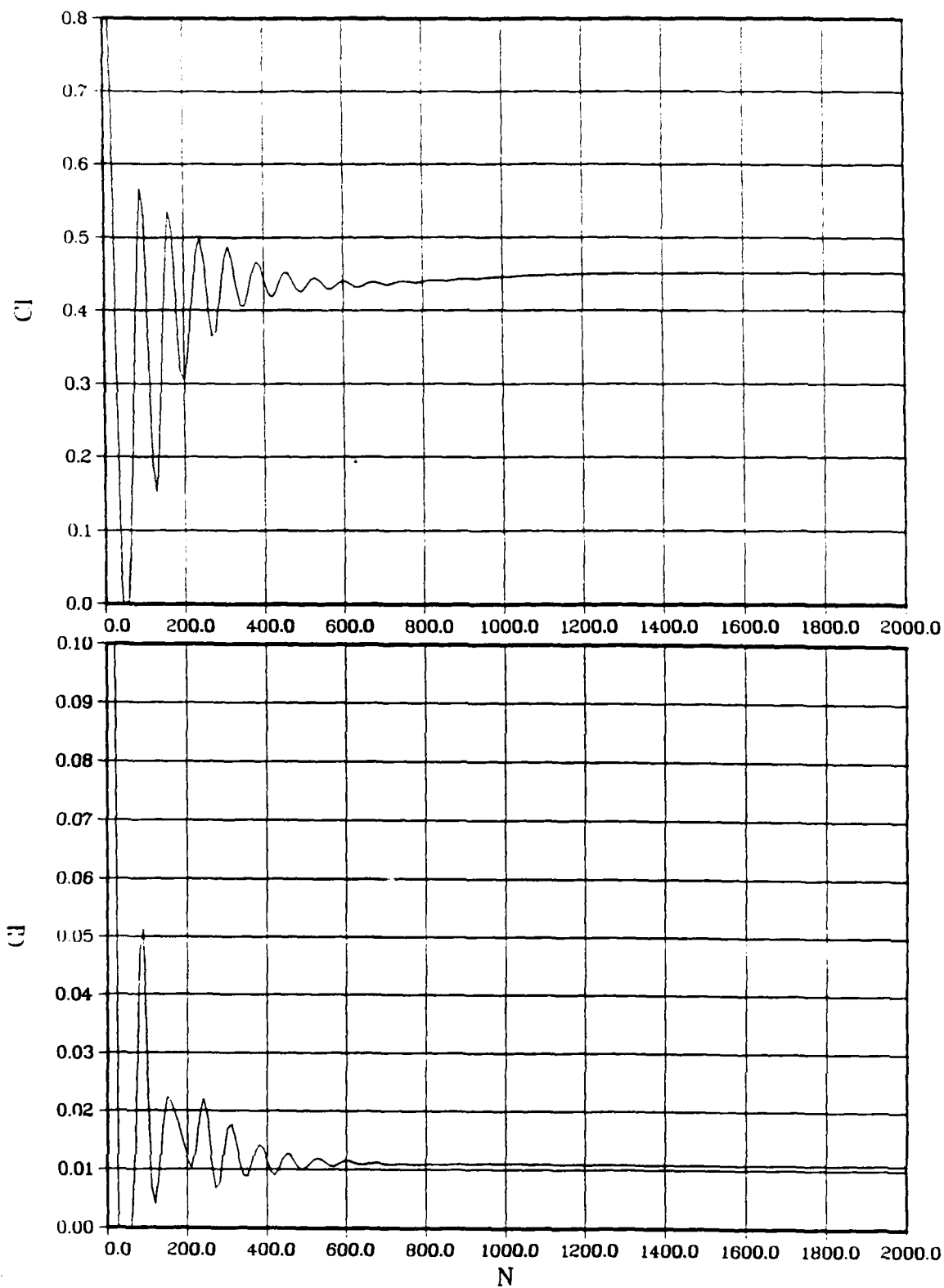


Figure 53. C-grid 4: Force Coefficients vs Iterations, $M = 0.3, \alpha = 4.04$

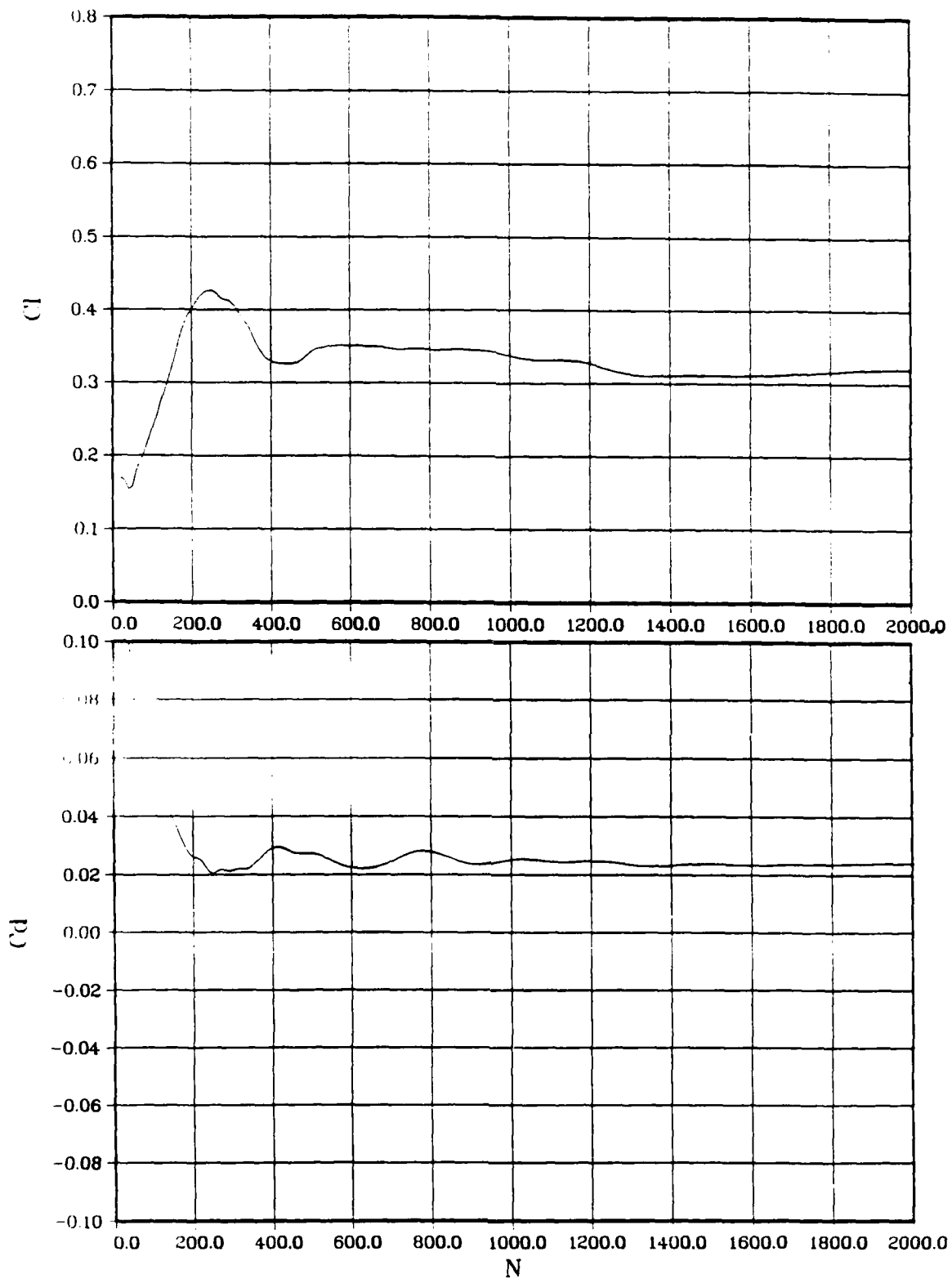


Figure 54. O-grid 3: Force Coefficients vs Iterations, $M = 0.775, \alpha = 2.03$

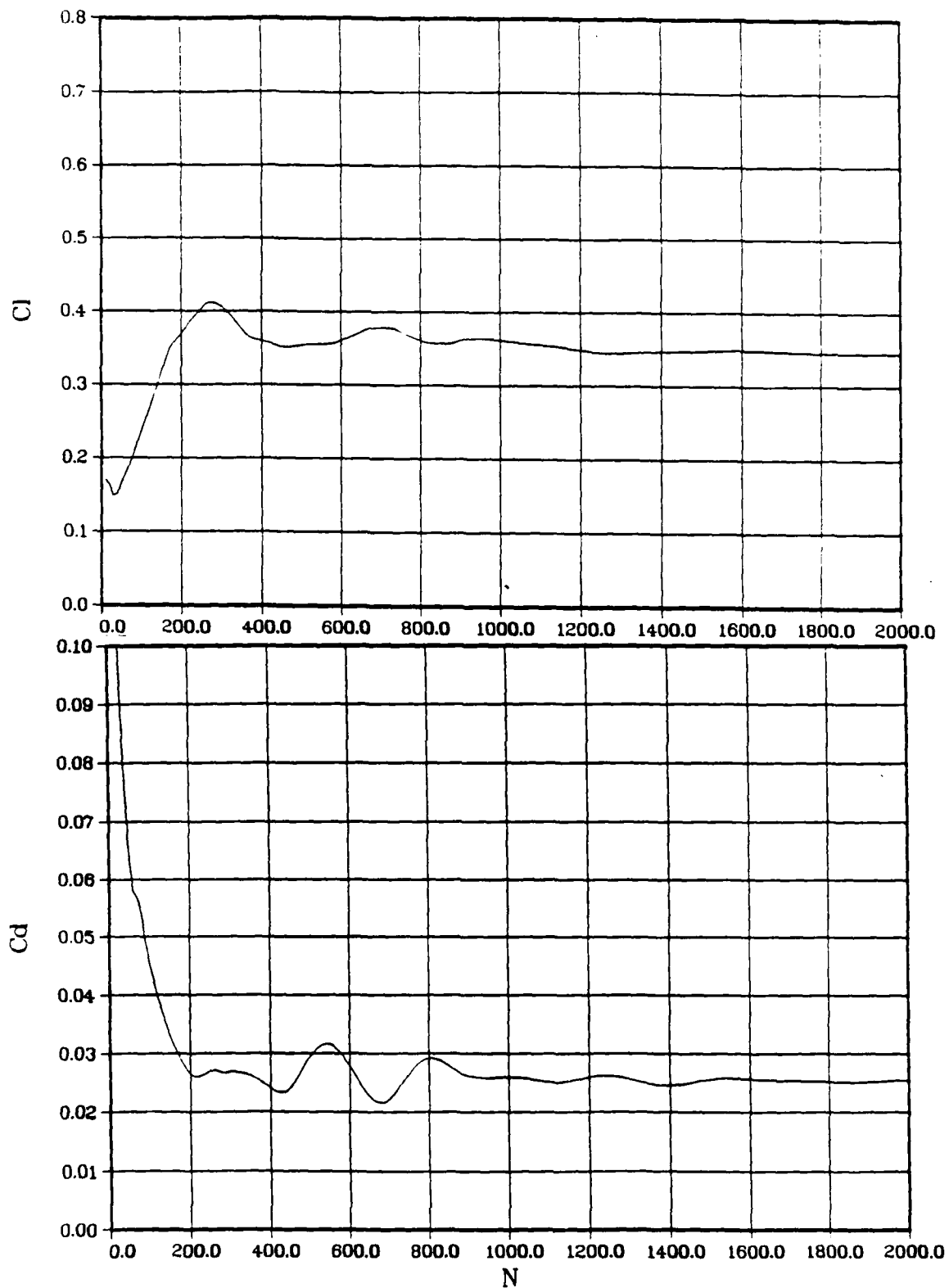


Figure 55. C-grid 4: Force Coefficients vs Iterations, $M = 0.775, \alpha = 2.03$

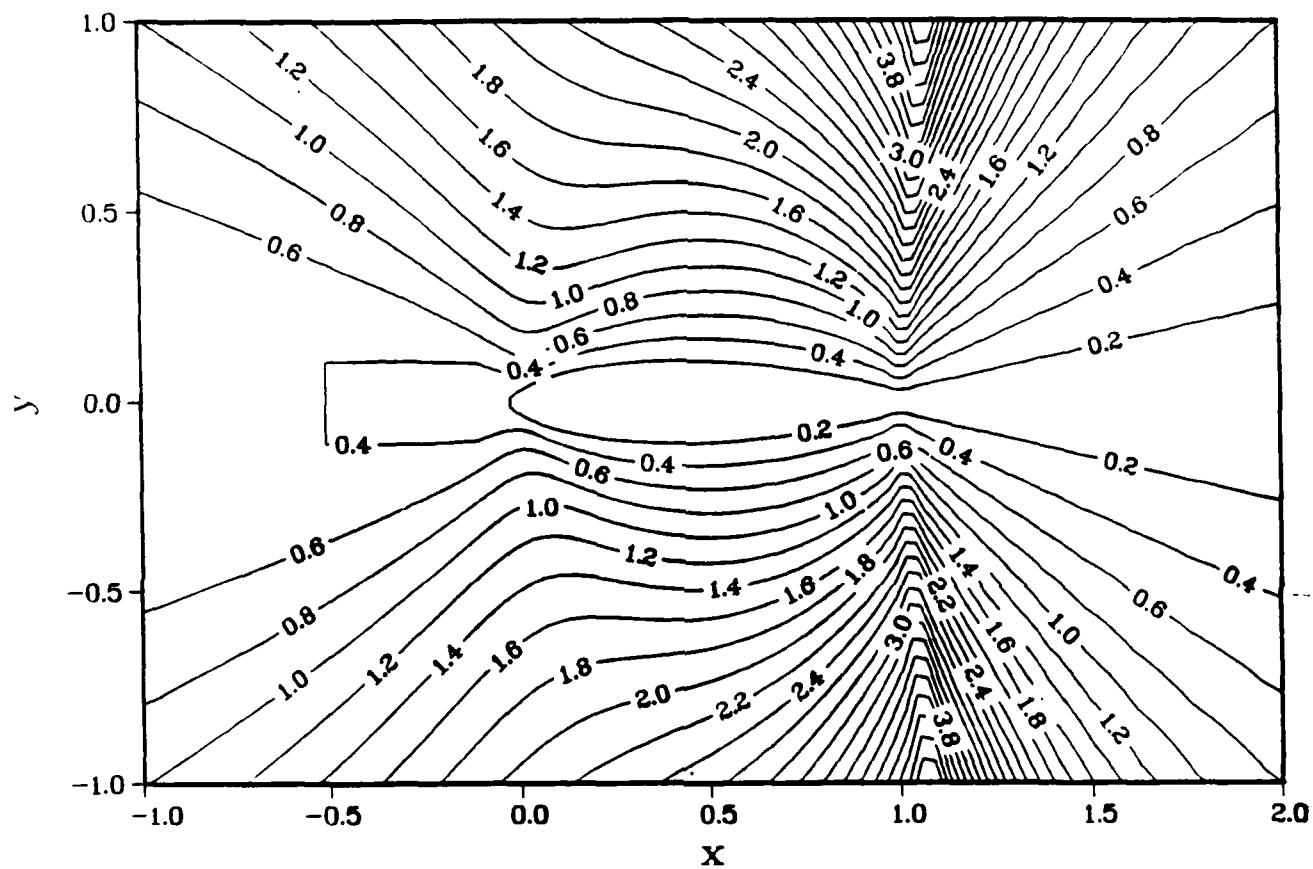


Figure 56. C-grid 4: Aspect Ratio Contours

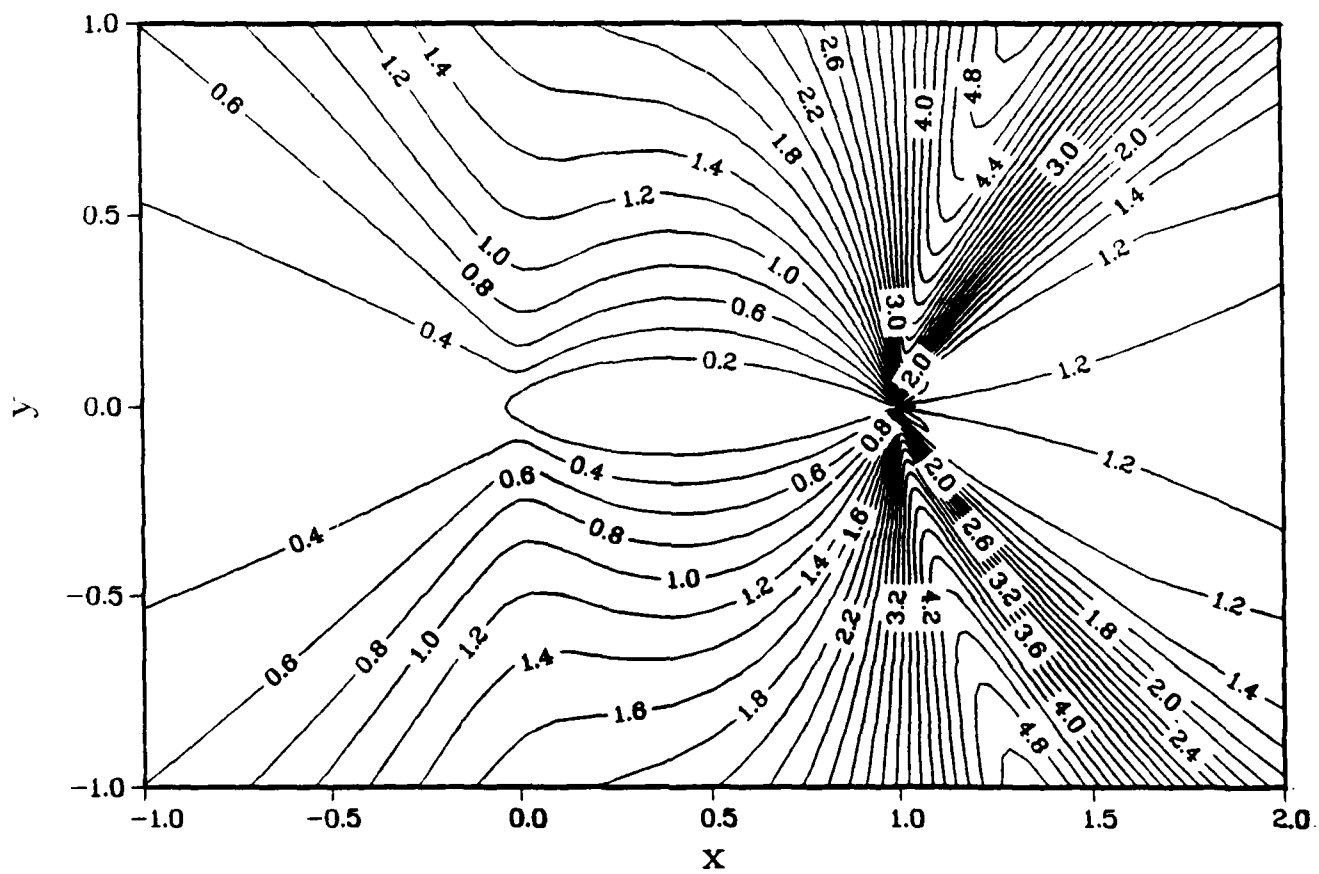


Figure 57. O-grid 3: Aspect Ratio Contours

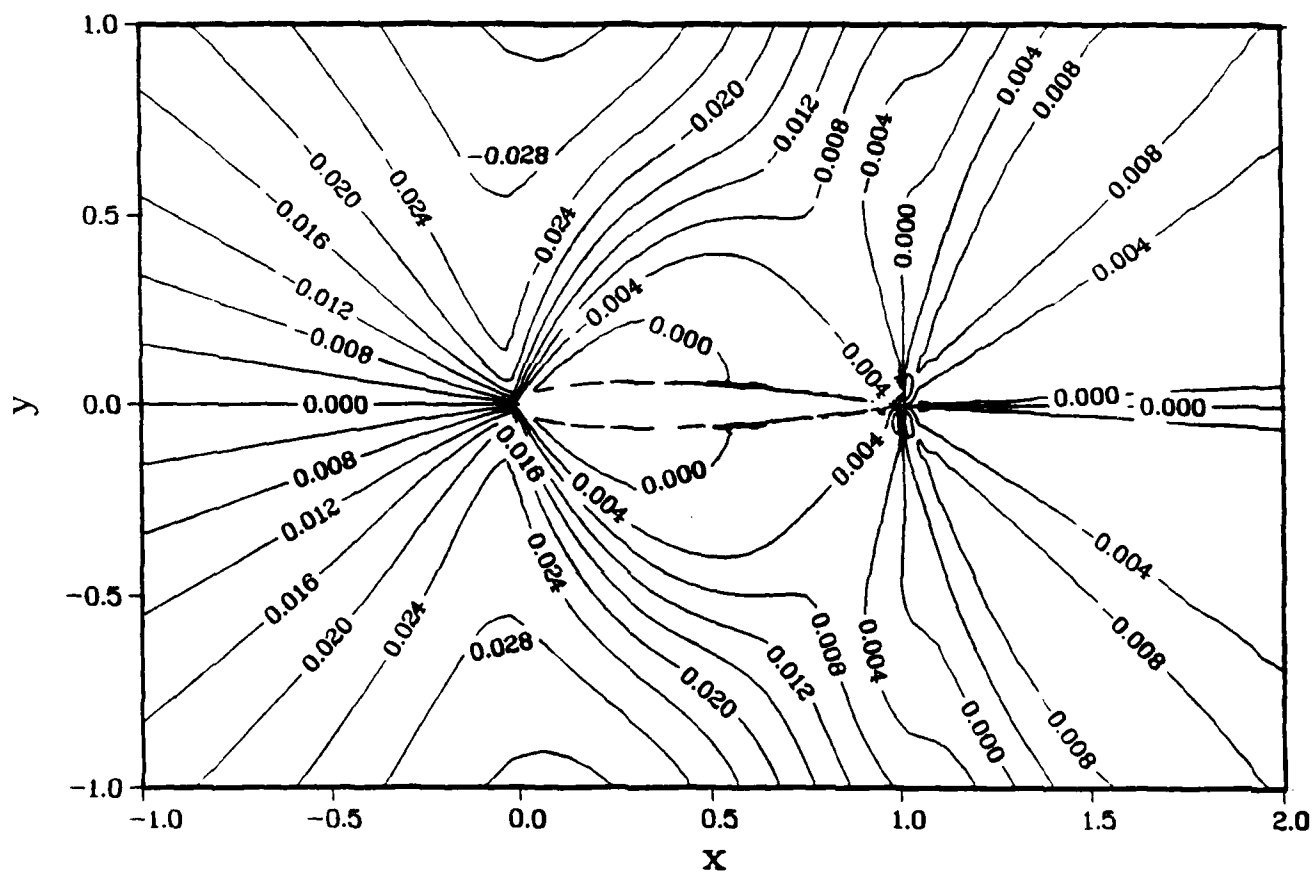


Figure 58. C-grid 4: Non-orthogonality Contours

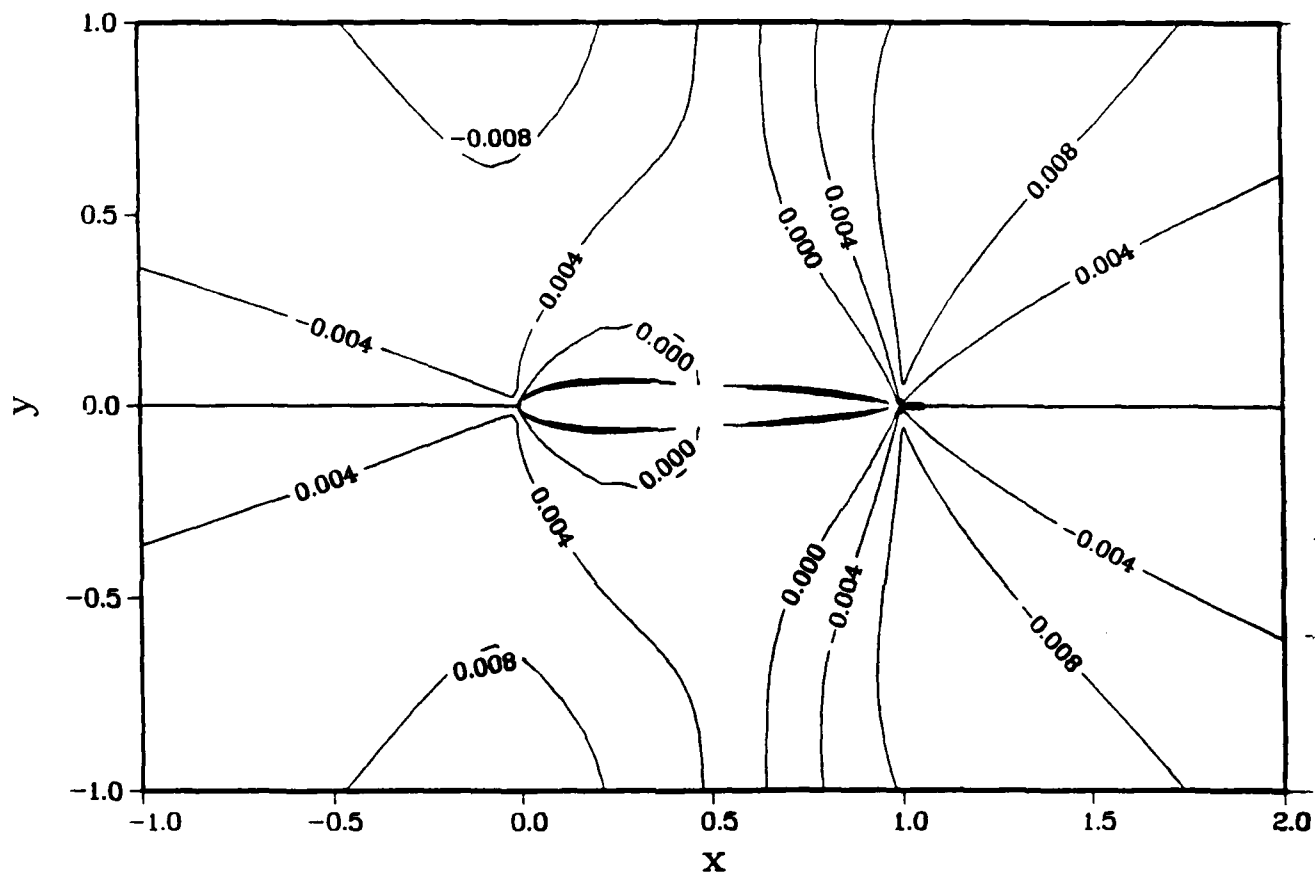


Figure 59. O-grid 3: Non-orthogonality Contours

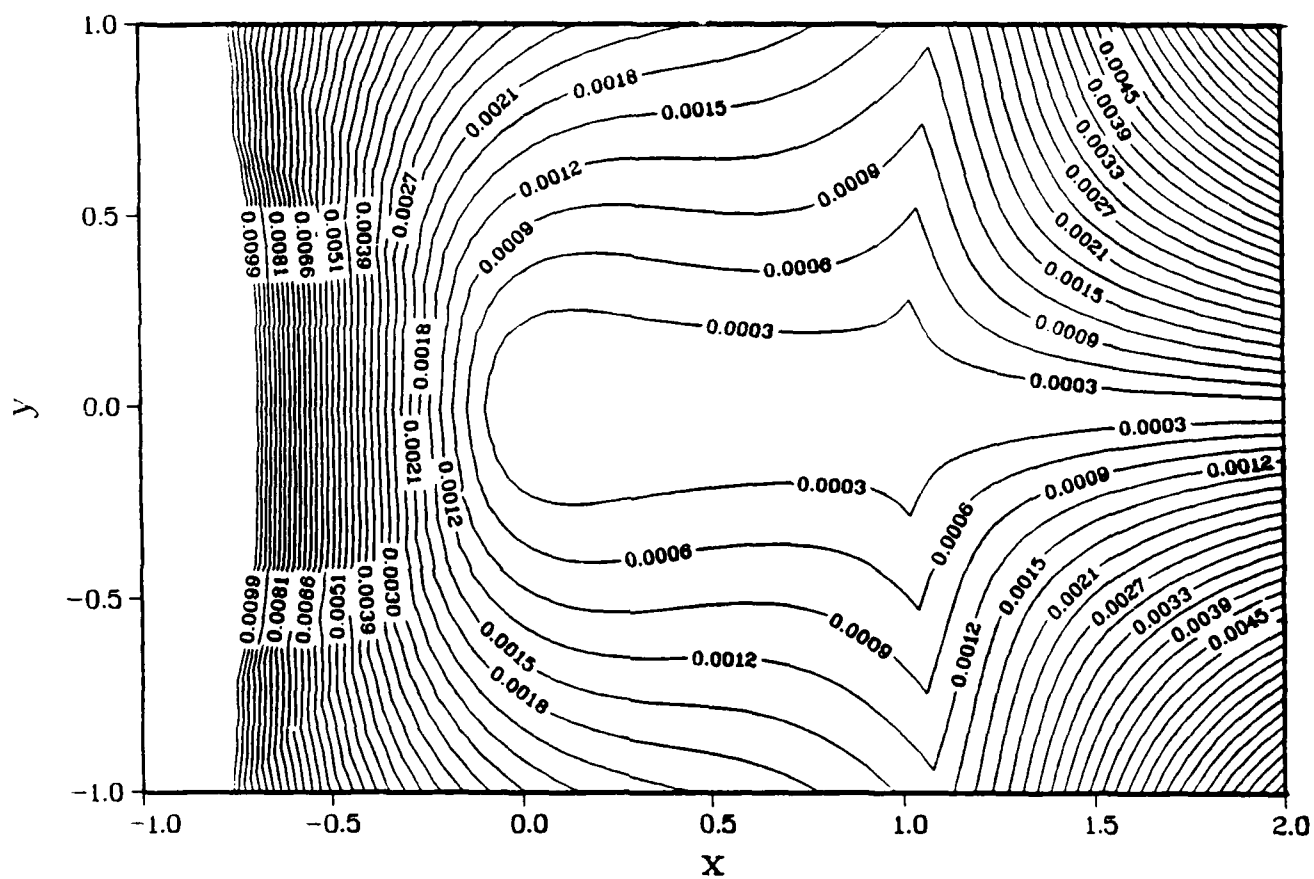


Figure 60. C-grid 4: Jacobian Contours

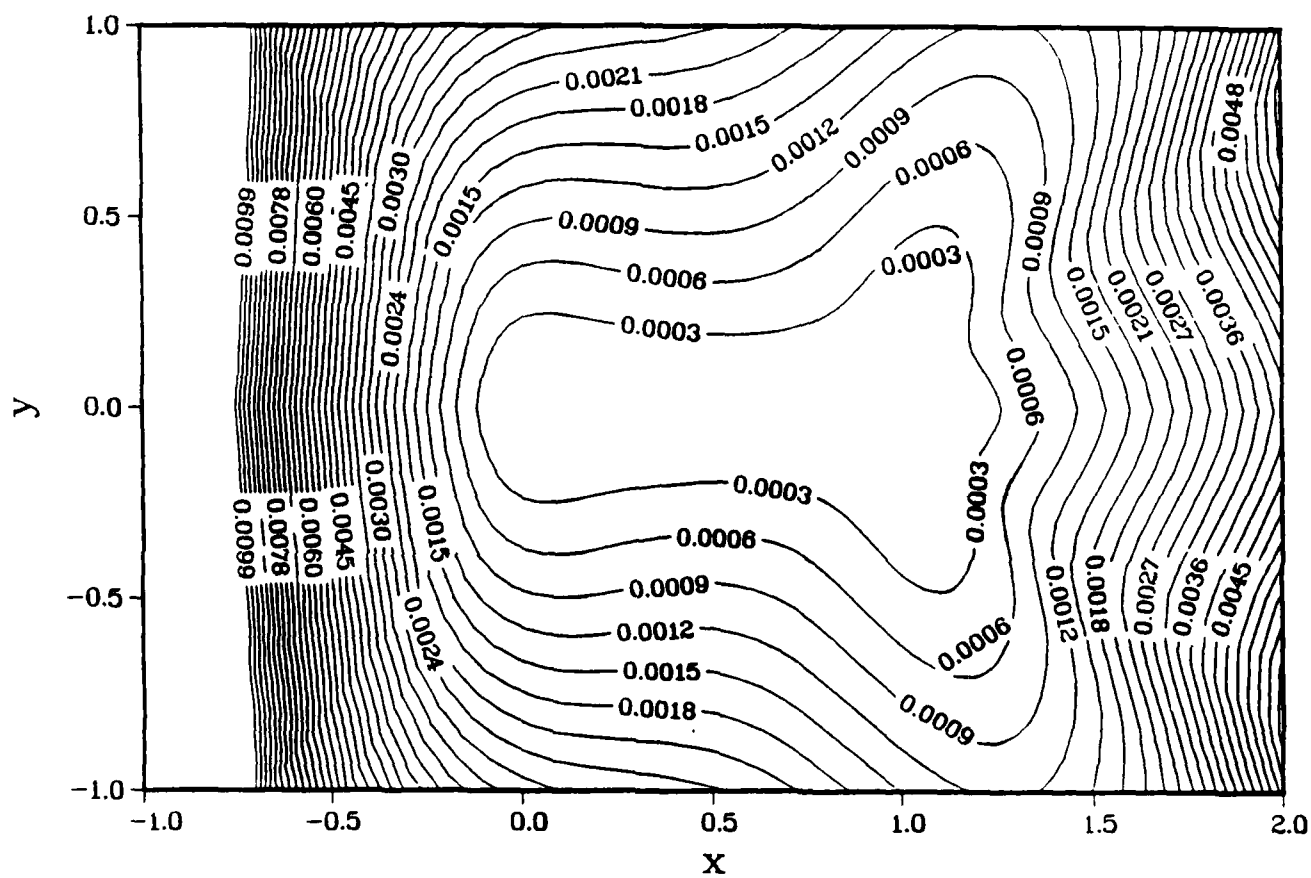


Figure 61. O-grid 3: Jacobian Contours

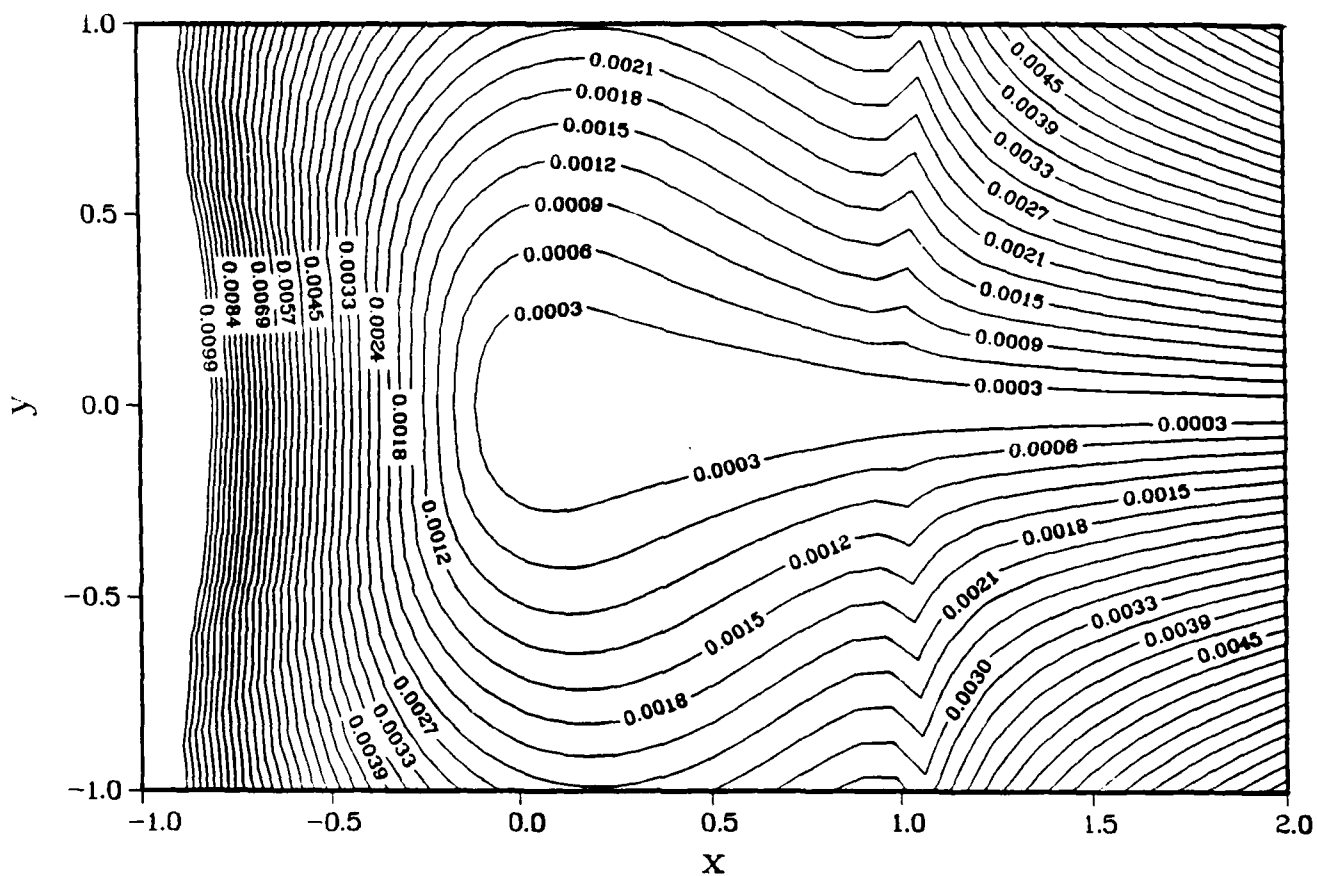


Figure 62. C-grid 4: Jacobian Contours - Smoothed Metrics

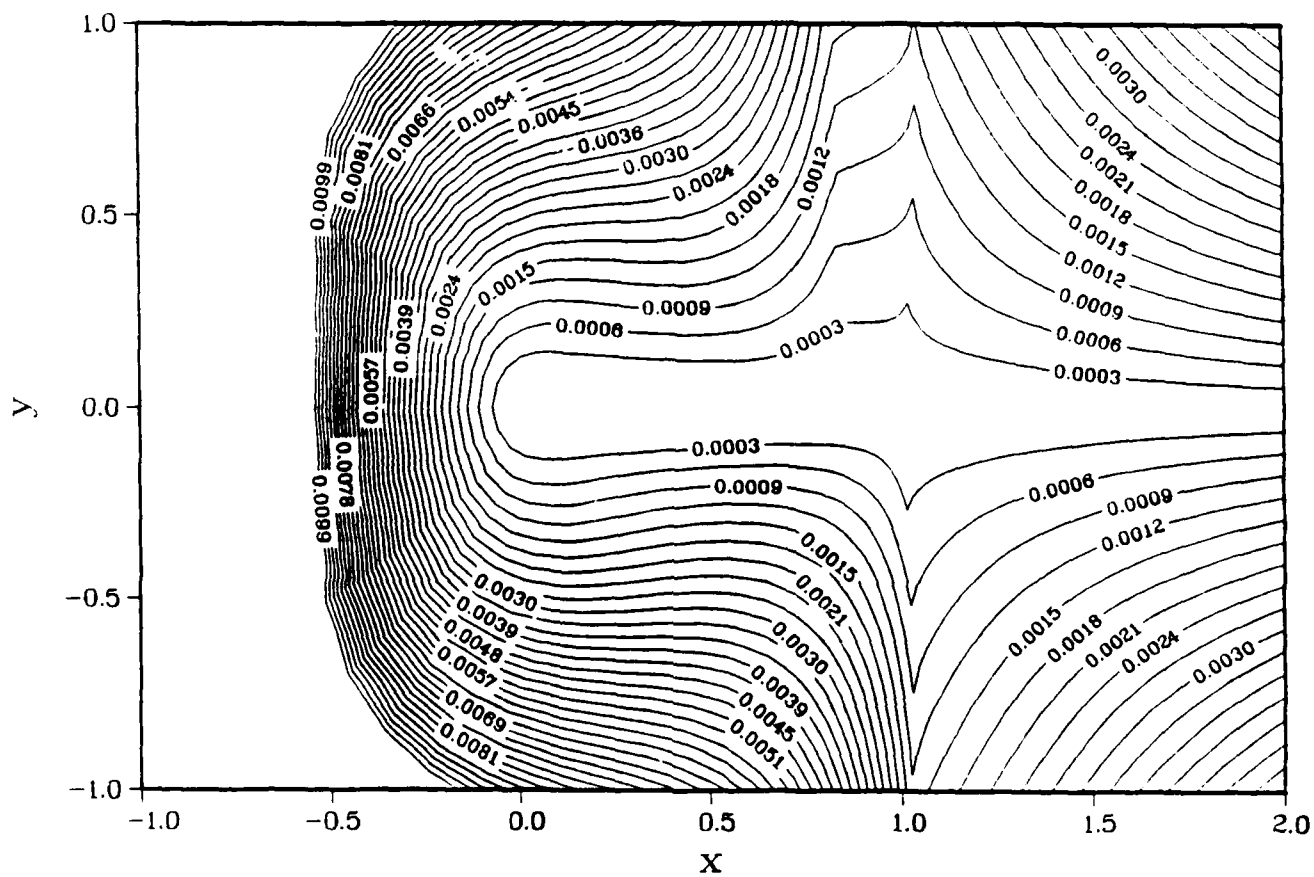


Figure 63. C-grid 8: Jacobian Contours - Smoothed Metrics

V. Conclusions and Recommendations

The numerical solutions obtained with both the C- and O-grid configurations using the Beam and Warming approximate factorization algorithm compare favorably to both experiment and previous numerical results. The numerical results produced indicate that both grids are satisfactory in a general application. However, specific weaknesses arise for each type of grid in certain situations. In these instances there may be an advantage in selecting a particular type of grid.

Studies in the subsonic range indicate that when equal spacing of grid points is specified at the leading edge, the O-grid is superior to the C-grid in determining the pressure coefficient in the vicinity of the leading edge. The O-grid also displays a pronounced advantage when large flow gradients appear in the vicinity of the trailing edge, such as the formation of a lambda shock. The O-grid typically exhibits a clustering of grid points around the trailing edge, and the gradient of the transformation metrics is considerably smoother. For certain critical flow conditions, e.g., a combination of high Reynolds number, high Mach number or angle of attack, the O-grid displays superior numerical stability when compared with the C-grid. This result is a likely result of two effects: the global smoothness of the transformation metrics compared to those of the C-grid, and the errors induced by the boundary conditions across the C-grid branch cut. The increased numerical stability, demonstrated by the O-grid, allows a better estimation of α at $C_{l_{max}}$.

The C-grid displayed several advantages over the O-grid as well. One advantage is ease of application. It is generally easier to construct a C-grid to a given set of specifications than an O-grid. The C-grid can be constructed in a single step with minimal effort, while the O-grid requires multiple steps. It is also difficult in the case of the O-grid to concentrate grid points in the wake while maintaining a reasonable spacing at the trailing edge. The O-grid generator tends to coalesce points in a fan-like shape directly above and below the trailing edge. Too fine a spacing

at the trailing edge can produce numerical instabilities when using a hyperbolic grid generator. Therefore, it becomes difficult to maintain adequate grid spacing in the wake. In the wake region, both grids display problems. The O-grid has difficulty resolving flow structures because of the large grid spacing there. The C-grid develops small oscillations along the branch cut where the boundary conditions are applied. However, the C-grid handles the flow resolution better in the wake when the flow gradients are concentrated directly behind the airfoil. In this region the C-grid displays a considerably higher concentration of grid points. The C-grid also predicts the pressure distribution and shock location more accurately than the O-grid in the transonic case. The O-grid can approach the C-grid performance in this regard only if a deliberate attempt is made to match the point distribution occurring in the C-grid case, at the cost of a further deterioration of the solution in the wake.

The selection of a specific grid type should be geared to the application considered, as indicated by the conclusions enumerated above. However, there are several recommendations that could increase the utility of both types of grids. In the case of the C-grid, central differencing across the branch cut could reduce or eliminate some of the spurious results demonstrated in the wake. However, this would create additional computational and memory requirements. In the case of the O-grid, the lack of an ability to control grid spacing in the wake, when applying a hyperbolic grid generator, presents a significant problem. Therefore, an elliptic grid generation scheme should be considered. This represents an added degree of difficulty due to the iterative numerical process required and the constraint of the outer computational domain. However, the constraint of the outer domain offers a means to control the grid spacing in the wake.

An important consideration, which applies to both C- and O-grids, is the minimization of artificial viscosity. In particular, second-order artificial viscosity has a considerable effect upon the pressure distribution on the surface and the integrated variables C_l and C_d . The minimization of artificial viscosity should be considered a

prerequisite to obtaining an accurate solution.

Another approach worth consideration is an attempt to reduce the overall truncation error by smoothing the transformation metrics. This involves a trade off between the need to concentrate grid points in an area of interest and not allowing a steep gradient in the transformation metrics to result. The most likely area of application would be in the region above and below the trailing edge in the case of the C-grid. A method of smoothing the metrics in this region, without unduly compromising the grid spacing, may provide a means of reducing the overall truncation error.

Appendix A. *Non-dimensional Variables*

The Navier-Stokes equations are generally nondimensionalized to allow for ease of application. This is accomplished by selecting reference length, velocity, and mass scales, L^* , U_∞^* , and ρ_∞^* respectively. The advantage of this approach is the appearance of non-dimensional parameters such as Mach number, Reynolds number, and Prandtl number, which can then be varied independently. Denoting dimensional variables with a *, the nondimensionalization appears as follows (6:191) (5:16)

$$\begin{array}{llll}
 x = \frac{x^*}{L^*} & y = \frac{y^*}{L^*} & u = \frac{u^*}{U_\infty^*} & v = \frac{v^*}{U_\infty^*} \\
 p = \frac{p^*}{\gamma M_\infty^2 \rho_\infty^*} & \rho = \frac{\rho^*}{\rho_\infty^*} & T = \frac{\gamma M_\infty^2}{\rho} & \mu = \frac{\mu^*}{\mu_\infty^*} \\
 \epsilon = \frac{\epsilon^*}{\mu_\infty^*} & q = \frac{q^*}{\rho_\infty^*} & E_1 = \frac{E_1^*}{\gamma M_\infty^2 \rho_\infty^*} & c = \frac{c^*}{\rho} \\
 M_\infty = \frac{U_\infty^*}{\sqrt{\gamma R T_\infty^*}} & Re = \frac{\rho_\infty^* U_\infty^* L^*}{\mu_\infty^*} & t = \frac{U_\infty^* t^*}{L^*} & L^* = c
 \end{array}$$

Appendix B. *Jacobian Matrices*

The Jacobian matrices employed in equations (98-99) are presented below. They are obtained by rewriting the vectors E_1 , E_2 , V_1 , and W_2 appearing in equations (51-56) in terms of the conserved variables $(\rho/J, \rho u/J, \rho v/J, \rho e/J)$ and differentiating with respect to \hat{U} , \hat{U}_ξ , or \hat{U}_η as indicated in equations (98-99). The resulting matrices are then (18:45)

$$A = \begin{pmatrix} 0 & \xi_x & \xi_y & 0 \\ \xi_x \phi - u\mathcal{U} & \mathcal{U} - (\gamma - 2)\xi_x u & \xi_y u - (\gamma - 1)\xi_x v & (\gamma - 1)\xi_x \\ \xi_y \phi - v\mathcal{U} & \xi_x u - (\gamma - 1)\xi_y u & \mathcal{U} - (\gamma - 2)\xi_y v & (\gamma - 1)\xi_y \\ (2\phi - \gamma e)\mathcal{U} & (\gamma e - \phi)\xi_x - (\gamma - 1)u\mathcal{U} & (\gamma e - \phi)\xi_y - (\gamma - 1)v\mathcal{U} & \gamma\mathcal{U} \end{pmatrix}, \quad (115)$$

$$B = \begin{pmatrix} 0 & \eta_x & \eta_y & 0 \\ \eta_x \phi - u\mathcal{V} & \mathcal{V} - (\gamma - 2)\eta_x u & \eta_y u - (\gamma - 1)\eta_x v & (\gamma - 1)\eta_x \\ \eta_y \phi - v\mathcal{V} & \eta_x u - (\gamma - 1)\eta_y u & \mathcal{V} - (\gamma - 2)\eta_y v & (\gamma - 1)\eta_y \\ (2\phi - \gamma e)\mathcal{V} & (\gamma e - \phi)\eta_x - (\gamma - 1)u\mathcal{V} & (\gamma e - \phi)\eta_y - (\gamma - 1)v\mathcal{V} & \gamma\mathcal{V} \end{pmatrix}, \quad (116)$$

where $\phi = 1/2(\gamma - 1)(u^2 + v^2)$.

The Jacobian matrices M and N are defined by

$$M = \frac{1}{\rho} \begin{pmatrix} 0 & 0 & 0 & 0 \\ -(b_1 u + b_2 v) & b_1 & b_2 & 0 \\ -(b_2 u + b_3 v) & b_2 & b_3 & 0 \\ b_{41} & b_{42} & b_{43} & b_{44} \end{pmatrix}, \quad (117)$$

where

$$\begin{aligned} b_{41} &= -(b_1^2 + 2b_2 uv + b_3 v^2 + b_4 \gamma (\gamma - 1)(u^2 + v^2 - e)) \\ b_{42} &= b_1 - b_4 \gamma (\gamma - 1)u + b_2 v \\ b_{43} &= b_2 u + b_3 - b_4 \gamma (\gamma - 1) \\ b_{44} &= b_4 \gamma (\gamma - 1), \end{aligned}$$

and

$$N = \frac{1}{\rho} \begin{pmatrix} 0 & 0 & 0 & 0 \\ -(d_1 u + d_2 v) & d_1 & d_2 & 0 \\ -(d_2 u + d_3 v) & d_2 & d_3 & 0 \\ d_{41} & d_{42} & d_{43} & d_{44} \end{pmatrix}, \quad (118)$$

where

$$\begin{aligned} d_{41} &= -(d_1^2 + 2d_2 uv + d_3 v^2 + d_4 \gamma (\gamma - 1)(u^2 + v^2 - e)) \\ d_{42} &= d_1 - d_4 \gamma (\gamma - 1)u + d_2 v \\ d_{43} &= d_2 u + d_3 - d_4 \gamma (\gamma - 1) \\ d_{44} &= d_4 \gamma (\gamma - 1). \end{aligned}$$

The coefficients b_i and d_i appearing in M and N respectively are defined in equations (59) through (71).

Appendix C. *Boundary and Initial Conditions*

The particular solution of all differential equations requires the specification of boundary and/or initial conditions. In this case, the boundary conditions take the form of specifying flow variables on the airfoil surface and along the grid boundaries. Initial conditions are specified by assigning flow variables throughout the field upon code initiation.

Referring to Figure 1, freestream values in non-dimensional form are assigned throughout the flow field and along the boundary ABC.

$$\begin{aligned}\rho &= \rho_{\infty} = 1 & \epsilon &= \epsilon_{\infty} = 0 \\ p &= p_{\infty} = \frac{1}{\gamma M_{\infty}^2} & U_{\infty} &= 1 \\ u &= U_{\infty} \cos(\alpha) & v &= U_{\infty} \sin(\alpha).\end{aligned}\tag{119}$$

The initial eddy viscosity is generally set equal to a constant in the boundary along the airfoil. Since the initial conditions are a function of Mach number and angle of attack, it is required that restart solutions maintain the same Mach number and angle of attack.

At the airfoil surface, EFG, an adiabatic condition is imposed. The velocities are determined there by no-slip condition.

$$u_w = v_w = 0.\tag{120}$$

The boundary-layer assumption is employed, as the gradient of pressure normal to the surface is assumed zero. The adiabatic assumption implies that the temperature gradient normal to the surface is zero. The surface density is permitted to vary as a function of surface pressure and temperature via the perfect gas law.

$$\frac{\partial}{\partial \eta} \begin{pmatrix} p \\ T \end{pmatrix}_w = 0 \quad (121)$$

$$\rho_w = \rho_w(p, T). \quad (122)$$

The downstream outflow conditions along boundaries AD and HC are computed by the following means

$$p = p_\infty \quad (123)$$

$$\frac{\partial}{\partial \xi} \begin{pmatrix} \rho \\ \epsilon \\ u \\ v \end{pmatrix} = 0. \quad (124)$$

In general, the derivative conditions here allow for large scale flow fluctuations due to the forces applied on the body.

In the case of the C-grid, the boundary conditions along the branch cut must be specified to assure continuity is satisfied. Thus along cut ED and EH, the following is applied

$$\frac{\partial}{\partial \eta} \begin{pmatrix} p \\ \rho \\ \epsilon \\ u \\ v \end{pmatrix}_{\text{lower}} = \frac{\partial}{\partial \eta} \begin{pmatrix} p \\ \rho \\ \epsilon \\ u \\ v \end{pmatrix}_{\text{upper}} \quad (125)$$

which reduces to averaging across the wake

$$\begin{pmatrix} p \\ \rho \\ \epsilon \\ u \\ v \end{pmatrix}_{wake} = \frac{1}{2} \begin{pmatrix} p \\ \rho \\ \epsilon \\ u \\ v \end{pmatrix}_{lower} + \frac{1}{2} \begin{pmatrix} p \\ \rho \\ \epsilon \\ u \\ v \end{pmatrix}_{lower} \quad (126)$$

In the case of the O-grid, the placement of the wake cut is arbitrary and in this case is chosen to extend from the leading edge to the forward boundary. Coincident grid lines are superimposed over those lines bordering the O-grid wake cut to allow for central differencing to be applied across the wake rather than the somewhat artificial boundary condition imposed in the C-grid wake. This represents a difference in the manner in which the boundary conditions are applied in the two cases.

Appendix D. *Turbulence Model*

One of the most difficult problems in modern computational fluid dynamics is the correct modeling of the turbulence. The turbulence model employed here is a modified version of the algebraic eddy-viscosity model of Baldwin and Lomax (3). The application of the turbulence model is applied in three separate regions: the boundary layer on the airfoil, the wake proximal to the airfoil trailing edge, and the far-field wake (see Figure 59).

The boundary layer of the airfoil is divided into an inner and outer region. In the inner region, the eddy viscosity, ϵ_i , is given by the Prandtl-Van Driest formula (18:12)

$$\epsilon = \rho(KD)^2 |\omega| \quad (127)$$

with

$$D = 1 - \exp \left[-\frac{Y}{26} \left(\frac{\rho_w |\omega_w|}{\mu_w} \right)^{.5} \right] \quad (128)$$

and

$$\omega = \frac{\partial u}{\partial y} - \frac{\partial v}{\partial x} \quad (129)$$

where ω is the vorticity, Y represents the normal distance to the airfoil surface, $K = 0.40$ is the von Karman constant, and the subscript w denotes conditions located at the surface (wall).

In the outer region of the boundary layer, the eddy viscosity is defined by (18:12)

$$\epsilon_o = \rho K C_{cp} Y_{max} F_{max} F_k \quad (130)$$

$$F_k = \left[1 + 5.5(C_k Y / Y_{max})^6 \right]^{-1} \quad (131)$$

where $F_{mas} = \max(Y|\omega|D)$, Y_{mas} is the value of Y corresponding to F_{mas} and $k = 0.0168$, $C_{cp} = 1.6$, $C_k = 0.3$.

The turbulence model switches from the inner to outer formulation at the first value of Y for which $\epsilon_i \geq \epsilon_o$. Transition from laminar to turbulent flow is specified by user input and is chosen to match boundary-layer trip locations when comparing to experimental data.

The turbulence model in the far-wake is modeled by defining the turbulent eddy viscosity there as (18:13)

$$\epsilon_{wk} = \rho C_{wk} \frac{Y_{mas} \Delta U^2}{F_{mas}} F_k \quad (132)$$

where

$$C_{wk} = 0.058$$

$$F_{mas} = \max(Y|\omega|)$$

$$\Delta U = (u^2 + v^2)_{mas}^{1/2} - (u^2 + v^2)_{min}^{1/2}$$

In the wake, Y_{mas} is measured from the wake centerline as determined by the location of minimum velocity. The intermittency factor F_k is obtained from equation (131). The constants C_{wk} and C_k are chosen to match theoretical values for an incompressible turbulent wake (14).

In the near-wake the turbulent eddy viscosity is determined by exponentially smoothing the eddy viscosity profile at the trailing edge to the far-wake profile. The following functional form is employed (18:14):

$$\begin{aligned} \epsilon_{nw} = & \frac{1}{2} \{ [\epsilon(x_{te}, Y) + \epsilon_{wk}(x_o, Y)] \\ & + A [\epsilon(x_o, Y) - \epsilon(x_{te}, Y)] \} \end{aligned} \quad (133)$$

$$A = \tanh \left[8 \frac{x - x_{te}}{x_o - x_{te}} - 4 \right]$$

The distance $x_o - x_{te}$ is chosen to be of order 10δ , where δ is the average boundary layer thickness at the trailing edge. It should be noted that Visbal considers the near-wake formulation a preliminary approach within the context of the algebraic eddy viscosity model.

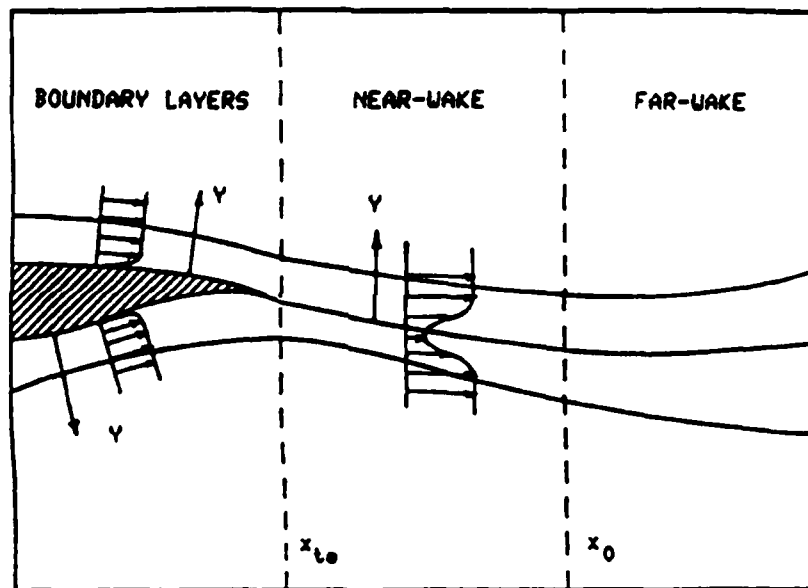


Figure 64. Regions of Application for Turbulence Model

(Ref:18)

Appendix E. *Computer Resources and Codes*

The Navier-Stokes code was executed on two computer systems. The primary computer utilized was the Aeronautical Systems Division Cray XMP, located at Wright-Patterson Air Force Base, Ohio. Selected data runs were accomplished on the Air Force Institute of Technology Stellar computer, also located at Wright-Patterson Air Force Base. Table 3 compares execution times of the two computers (CPU time). The times quoted are for 500 iterations using a 119x40 C-Grid. The computations on the Stellar were performed using single-precision (32 bit) accuracy, while the runs performed on the Cray XMP were performed using double-precision (64 bit) accuracy. The front-end machine used to interface with the Cray XMP was the Aeronautical Systems Division Cray-Vax.

Additional computer resources employed included the FDL Iris and Prime computers. The Iris workstation was utilized for grid generation and data reduction. Data plotting was accomplished using the Prime computer, in conjunction with the Talaris laser printer.

A computer listing is provided for the metric analysis program used to calculate the Jacobian, aspect ratio, orthogonality, and skewness parameters for a given grid. The transformation metrics are extracted directly from the Navier-Stokes code, the above parameters are then calculated from the metrics. Listings of the Navier-Stokes

computer	CPU time (sec)	C-Grid	Iterations	C_l	C_d
Stellar	60.1	119x40	500	0.35398	0.029575
Cray XMP	64.4	119x40	500	0.35416	0.029480

Table 3. Comparison of CPU times: Cray vs Stellar

code for the C-grid and the associated data reduction codes may be found by referring to Boyles (5). Both the C- and O-grid Navier-Stokes codes, and the grid generation codes, are archived on the Stellar computer.

PROGRAM METRIC CALCULATES THE TRANSFORMATION METRICS AND USES
HOW TO CALCULATE THE GEOMETRIC QUANTITIES:
JACOBIAN, ASPECT RATIO, ORTHOGONALITY, AND DETERMINANT.
NOTE: SUBROUTINE.

```

PROGRAM SETVEC
      DIMENSION I(20),Y(10),X(10),YI(10),XI(10),YII(10),XII(10),
      & VETA(20),HJAC(10),COCAL(10),COSTH(10),AR(10),AO

```

WATER INTO FUEL

FROM (LAST) Vol. FILE No. 4-14, STATUS: OLD.)

```

SPRAMEQST12, PLEN = 2, STATUS = 'UNOPEN'
SPRAMEQST13, PLEN = 0, STATUS = 'UNOPEN'
SPRAMEQST14, PLEN = 0, STATUS = 'UNOPEN'
SPRAMEQST15, PLEN = 0, STATUS = 'UNOPEN'
SPRAMEQST16, PLEN = 0, STATUS = 'UNOPEN'

```

2021-2022 1st 6/18

UNITED STATES DEPARTMENT OF AGRICULTURE
BUREAU OF PLANT INDUSTRY

NEW IN Q12

$$\begin{aligned} & \text{DO } 100 \text{ J}=1, \text{J} \\ & \text{DO } 100 \text{ I}=1, \text{IL} \\ & \text{SUM}=(1.000) \times (\text{I}, \text{J}) \times (\text{I}, \text{J}) \times (\text{I}, \text{J}) \end{aligned}$$

01 CONT PAGE

Form 47 (2018-9)

EVALUATE TRANSFORMATION METRICS

EXERCISING YOUR RIGHTS

$$\begin{aligned} \text{06 } 7 \quad J=2, A_1 \\ \text{06 } 7 \quad I=2, U_1 \\ X(1, J) = .6 * (X(I+1, J) - X(I-1, J)) \\ V(1, J) = .6 * (V(I+1, J) - V(I-1, J)) \\ W(1, J) = .6 * (W(I+1, J) - W(I-1, J)) \\ Y(1, J) = .6 * (Y(I+1, J) - Y(I-1, J)) \end{aligned}$$

Time 0

$$x(1-j) = 5 - (-x(2-j) + 4 \cdot x(2-j) - 3 \cdot x(1-j))$$
[illegible]

```

100 GO3 J=1, X
101 KJMAX = AMAX1 (KJCMAX, KJAC(I, J))
102 KJMIN = AMIN1 (KJCMIN, KJAC(I, J))
103 KJMAXX = AMAX1 (KJMAXX, AB(I, J))
104 KJMINX = AMIN1 (KJMINX, AB(I, J))
105 KJTHAX = AMAX1 (KJTHAX, COSTH(I, J))
106 KJTHMIN = AMIN1 (KJTHMIN, COSTH(I, J))
107 KJCMAX = AMAX1 (KJCMAX, COSAL(I, J))
108 KJCMIN = AMIN1 (KJCMIN, COSAL(I, J))
109 WRITE (18, 604) X(I, J), Y(I, J), KJAC(I, J)
110 WRITE (18, 604) X(I, J), Y(I, J), AB(I, J)
111 WRITE (14, 604) X(I, J), Y(I, J), COSTH(I, J)
112 WRITE (18, 604) X(I, J), Y(I, J), COSAL(I, J)
113 CONTINUE
114 WRITE (16, 606) KJCMIN, KJCMAX
115 WRITE (16, 606) KJMINX, KJMAXX
116 WRITE (16, 607) KJTHMIN, KJTHAX
117 WRITE (16, 608) KJCMIN, KJCMAX
118 WRITE (16, 609) (X(I, J)) / 2, X
119 FORMAT (2E12, 4)
120 FORMAT (1X, ' JACOBIAN MAX AND MIN = ', 2E12, 4)
121 FORMAT (1X, ' ASPECT RATIO MAX AND MIN = ', 2E12, 4)
122 FORMAT (1X, ' COS(THETA) MAX AND MIN = ', 2E12, 4)
123 FORMAT (1X, ' COS(ALPHA) MAX AND MIN = ', 2E12, 4)
124 FORMAT (1X, ' OUTPUT DATA DIMENSIONS = ', I4, ' X ', I4)
125 FORMAT (3X, ' COLUMN', I3)
126 FORMAT (4X, 'J', 5X, 'K', 5X, 'Y', 5X, 'KJAC(I, J)', 5X, 'KJXI(I, J)',
127 1 5X, 'KJETA(I, J)', 5X, 'KJY(I, J)', 5X, 'KJETA(I, J)')
128 FORMAT (2X, I3, 7 (3X, I10, 3))
129 FORMAT (10X, '... WARNING : JACOBIAN LESS OR EQUAL TO ZERO',
130 1 3X, 'MIN(COLUMN) = ', I16, 7, /)
131 FORMAT (3X, 'LOCATION IS AT I, J = ', I10, 2X, ' AND X, Y = ', 2E7, 3, /)
132 FORMAT (10I1, 10X, 'TRANSFORMATION DERIVATIVES' //)
133 CONTINUE
134
135
136
137
138
139
140
141
142
143
144
145
146
147
148
149
150
151
152
153
154
155
156
157
158
159
160
161
162
163
164
165
166
167
168
169
170
171
172
173
174
175
176
177
178
179
180
181
182
183
184
185
186
187
188
189
190
191
192
193
194
195
196
197
198
199
200
201
202
203
204
205
206
207
208
209
210
211
212
213
214
215
216
217
218
219
220
221
222
223
224
225
226
227
228
229
230
231
232
233
234
235
236
237
238
239
240
241
242
243
244
245
246
247
248
249
250
251
252
253
254
255
256
257
258
259
260
261
262
263
264
265
266
267
268
269
270
271
272
273
274
275
276
277
278
279
280
281
282
283
284
285
286
287
288
289
290
291
292
293
294
295
296
297
298
299
300
301
302
303
304
305
306
307
308
309
310
311
312
313
314
315
316
317
318
319
320
321
322
323
324
325
326
327
328
329
330
331
332
333
334
335
336
337
338
339
340
341
342
343
344
345
346
347
348
349
350
351
352
353
354
355
356
357
358
359
360
361
362
363
364
365
366
367
368
369
370
371
372
373
374
375
376
377
378
379
380
381
382
383
384
385
386
387
388
389
390
391
392
393
394
395
396
397
398
399
400
401
402
403
404
405
406
407
408
409
410
411
412
413
414
415
416
417
418
419
420
421
422
423
424
425
426
427
428
429
430
431
432
433
434
435
436
437
438
439
440
441
442
443
444
445
446
447
448
449
450
451
452
453
454
455
456
457
458
459
460
461
462
463
464
465
466
467
468
469
470
471
472
473
474
475
476
477
478
479
480
481
482
483
484
485
486
487
488
489
490
491
492
493
494
495
496
497
498
499
500

```

Bibliography

1. Abbott, Ira H. and Albert E. von Doenhoff. *Theory of Wing Sections*. New York: McGraw-Hill Book Co., 1949.
2. Advisory Group for Aerospace Research and Development. *Experimental Data Base for Computer Program Assessment*, London Technical Editing and Reproductions Ltd. NATO sponsored document: AGARD-AR-138.
3. Baldwin, B. and H.Lomax. "Thin Layer Approximation and Algebraic Model for Separated Turbulent Flows," *AIAA 16th Aerospace Sciences Meeting* (1988).
4. Beam, Richard M. and R. F. Warming. "An Implicit Factored Scheme for the Compressible Navier- Stokes Equations," *AIAA 3rd Computational Fluid Dynamics Conference* (1987).
5. Boyles, Paul D. *Navier-Stokes Solution for a NACA 0012 Airfoil With Mass Flux*. Technical Report, Air Force Institute of Technology, WPAFB OH, December 1988. AFIT/GAE/AA/88D-02.
6. Dale A. Anderson, John C. Tannehill, Richard H. Pletcher. *Computational Fluid Mechanics and Heat Transfer*. New York: Hemisphere Publishing Corp., 1984.
7. Harris, Charles D. *Two-dimensional Aerodynamic Characteristics of the NACA 0012 Airfoil in the Langley 8-Foot Transonic Pressure Tunnel*. Technical Report, National Aeronautics and Space Administration, 1981. Technical Memorandum 81927.
8. Kerlick, G. David and Goetz H. Klopfer. "Assessing the Quality of Curvilinear Coordinate Meshes by Decomposing the Jacobian Matrix." In *Numerical Grid Generation*, Elsevier Science Publishing Co, 1982.
9. Kinsey, Don W. and Timothy J. Barth. *Description of a Hyperbolic Grid Generating Procedure for Arbitrary Two-Dimensional Bodies*. AFWAL-TM-84-FIMM. WPAFB OH, July 1984.
10. McCroskey, W. J. *A Critical Assessment of Wind Tunnel Results for the NACA 0012 Airfoil*. Technical Report, National Aeronautics and Space Administration, 1987. Technical Memorandum 100019.
11. McDevitt, John B. and Arthur F. Okuno. *Static and Dynamic Pressure Measurements on a NACA 0012 Airfoil in the Ames High Reynolds Number Facility*. Technical Report, National Aeronautics and Space Administration, 1985. Technical Paper 2485.
12. McRae, D. Scott and Goetz H. Klopfer. *Nonlinear Error Analysis of Finite Difference Solutions*. Technical Report, AFWAL, Flight Dynamics Laboratory, WPAFB OH, 1988. AFWAL-TR-88-3012.

13. Peyret, Roger and Thomas D. Taylor. *Computational Methods for Fluid Flow*. New York: Springer-Verlag, 1984.
14. Schlichting, Hermann. *Boundary-Layer Theory (Seventh Edition)*. New York: McGraw-Hill Book Co., 1979.
15. Steger, Joseph L. and Denny S. Chaussee. "Generation of Body-Fitted Coordinates Using Hyperbolic Partial Differential Equations." In *SIAM J. Sci. Stat. Comp. Vol.1 No.4*, Society for Industrial and Applied Mathematics, 1980.
16. Visbal, Miguel R., "Vectorized Navier-Stokes Code, Beam and Warming Algorithm: C- Grid Configuration." August, 1985.
17. Visbal, Miguel R., "Vectorized Navier-Stokes Code, Beam and Warming Algorithm: O- Grid Configuration." July, 1986.
18. Visbal, Miguel R. *Calculation of Viscous Transonic Flows About a Supercritical Airfoil*. Technical Report, AFWAL, Flight Dynamics Laboratory, WPAFB OH, 1986. AFWAL-TR-86-3013.
19. Wang, Yi-Yun and Toshi Fujiwara. "Numerical Analysis of Transonic Flow Around a Two-Dimensional Airfoil by Solving Full Navier-Stokes Equations." In *Memoirs of The Faculty of Engineering*, Nagoya University, Japan, 1984.
20. White, Frank M. *Viscous Fluid Flow*. New York: McGraw Hill Book Co., 1974.

Vita

Captain Mark J. Lutton [REDACTED]

[REDACTED] entered the Air Force in 1977. After serving as a Medical Laboratory Specialist stationed at Eglin Air Force Base in Florida, he was selected for the Airman's Education and Commissioning Program. He attended The Pennsylvania State University and graduated with high distinction, earning a Bachelor of Science in Aerospace Engineering. After completing Officer Training School in 1984, he served as a flight test engineer at the Air Force Flight Test Center, Edwards Air Force Base, California, until entering the School of Engineering, Air Force Institute of Technology in 1988.

[REDACTED]

REPORT DOCUMENTATION PAGE

Form Approved
OMB No. 0704-0188

1. REPORT SECURITY CLASSIFICATION UNCLASSIFIED			1b. RESTRICTIVE MARKINGS		
2a. SECURITY CLASSIFICATION AUTHORITY			3. DISTRIBUTION/AVAILABILITY OF REPORT Approved for public release; distribution unlimited.		
2b. DECLASSIFICATION/DOWNGRADING SCHEDULE					
4. PERFORMING ORGANIZATION REPORT NUMBER(S) AFIT/GAE/AA/89D-21			5. MONITORING ORGANIZATION REPORT NUMBER(S)		
6a. NAME OF PERFORMING ORGANIZATION School of Engineering		6b. OFFICE SYMBOL (if applicable) AFIT/ENY		7a. NAME OF MONITORING ORGANIZATION	
6c. ADDRESS (City, State, and ZIP Code) Air Force Institute of Technology Wright-Patterson AFB, Ohio 45433			7b. ADDRESS (City, State, and ZIP Code)		
8a. NAME OF FUNDING/SPONSORING ORGANIZATION		8b. OFFICE SYMBOL (if applicable)		9. PROCUREMENT INSTRUMENT IDENTIFICATION NUMBER	
8c. ADDRESS (City, State, and ZIP Code)			10. SOURCE OF FUNDING NUMBERS		
			PROGRAM ELEMENT NO.	PROJECT NO.	TASK NO.
11. TITLE (Include Security Classification) COMPARISON OF C- AND O-GRID GENERATION METHODS USING A NACA 0012 AIRFOIL (UNCLASSIFIED)					
12. PERSONAL AUTHOR(S) Mark J. Lutton, B.S., Capt, USAF					
13a. TYPE OF REPORT Thesis		13b. TIME COVERED FROM _____ TO _____		14. DATE OF REPORT (Year, Month, Day) 1989 December	
15. PAGE COUNT					
16. SUPPLEMENTARY NOTATION Thesis Committee Chairman: Capt Philip S. Beran, Associate Professor of Aerospace Engineering					
17. COSATI CODES			18. SUBJECT TERMS (Continue on reverse if necessary and identify by block number)		
FIELD	GROUP	SUB-GROUP			
	04		Computational Fluid Dynamics; Fluid Dynamics; Beam and Warming algorithm; Navier-Stokes equations; Grid Generation		
19. ABSTRACT (Continue on reverse if necessary and identify by block number)					
<p>An investigation is undertaken to compare the performance of C- and O-grid generation methods as applied to numerically predicting the flow about a NACA 0012 airfoil. Both types of grid were generated using a hyperbolic grid generation code. The solution of the flow field was numerically calculated using the Beam and Warming algorithm to solve the two-dimensional Navier-Stokes equations for viscous, compressible flow.</p> <p>Numerical solutions are obtained for Mach number ranging from 0.3 to 1.1, angle of attack ranging from 0 to 13 degrees, and Reynolds numbers between 2 and 6 million. The numerical results obtained from both C- and O-grids are compared to experimental data.</p> <p>Results indicate a weakness is the method of applying the boundary conditions in the wake for the C-grid, while the overall resolution in the wake is poor for the O-grid due to inadequate control of grid spacing in that region.</p> <p>The transformation metrics are examined to explain differences observed in grid performance. <i>See notes</i></p>					
20. DISTRIBUTION/AVAILABILITY OF ABSTRACT <input checked="" type="checkbox"/> UNCLASSIFIED/UNLIMITED <input type="checkbox"/> SAME AS RPT. <input type="checkbox"/> DTIC USERS			21. ABSTRACT SECURITY CLASSIFICATION		
22a. NAME OF RESPONSIBLE INDIVIDUAL Capt Philip S. Beran			22b. TELEPHONE (Include Area Code) (513) 255-3517		22c. OFFICE SYMBOL AFIT/ENY

Theses. (jlt) 10